

3-17-93
E-11433-1

NASA Technical Memorandum 106019

A Full-Scale STOVL Ejector Experiment

Wendy S. Barankiewicz
Lewis Research Center
Cleveland, Ohio

February 1993

The NASA logo, consisting of the word "NASA" in a bold, sans-serif font.

A FULL-SCALE STOVL EJECTOR EXPERIMENT

WENDY S. BARANKIEWICZ

Bachelor of Science in Mechanical Engineering

The University of Illinois at Urbana-Champaign

May, 1989

Submitted in partial fulfillment of the requirements for the degree

Master of Science in MECHANICAL ENGINEERING

at the

Cleveland State University

December, 1992

A FULL-SCALE STOVL EJECTOR EXPERIMENT

WENDY S. BARANKIEWICZ

ABSTRACT

The design and development of thrust augmenting short take-off and vertical landing (STOVL) ejectors has typically been an iterative process. In this investigation, static performance tests of a full-scale vertical lift ejector were performed at primary flow temperatures up to 1560 R (1100°F). Flow visualization (smoke generators, yarn tufts and paint dots) was used to assess inlet flowfield characteristics, especially around the primary nozzle and end plates. Performance calculations are presented for ambient temperatures close to 480 R (20°F) and 535 R (75°F) which simulate "seasonal" aircraft operating conditions. Resulting thrust augmentation ratios are presented as functions of nozzle pressure ratio and temperature.

Full-scale experimental tests such as this are expensive, and difficult to implement at engine exhaust temperatures. For this reason the utility of using similarity principles -- in particular, the Munk and Prim similarity principle for isentropic flow -- was explored. At different primary temperatures, exit pressure contours are compared for similarity. A nondimensional flow parameter is then shown to eliminate primary nozzle temperature dependence and verify similarity between the hot and cold flow experiments. Under the assumption that an

appropriate similarity principle can be established, then properly chosen performance parameters should be similar for both hot flow and cold flow model tests.

TABLE OF CONTENTS

	Page
NOMENCLATURE	vii
LIST OF TABLES	x
LIST OF FIGURES	xi
CHAPTER	
I. INTRODUCTION	1
1.1 STOVL/Powered Lift Background	6
1.2 Literature Review	14
1.3 Scope of Work	19
II. EXPERIMENTAL FACILITY	23
2.1 Facility Description	25
2.1.1 Thrust Balance	25
2.1.2 Air Supply System	27
2.1.3 Instrumentation System	28
2.1.4 Data Acquisition System	30
2.2 Facility Calibrations	32
2.2.1 Static Hydraulic Calibration	32
2.2.2 Pressure Tare Calibration	33
2.2.3 STA Nozzle Calibration	34
III. DESCRIPTION OF EXPERIMENT	37
3.1 Model Specifications	37

3.2	Instrumentation	39
3.3	Testing procedure	44
3.4	Cold Flow Tests	45
3.4.1	Flow Visualization	45
3.4.2	Configuration Changes for Performance Optimization	48
3.5	Hot Flow Tests	52
IV.	RESULTS AND DISCUSSION	53
4.1	Thrust Augmentation Ratio	53
4.1.1	Cold Flow Tests	54
4.1.2	Hot Flow Tests	62
4.2	Surface Static Pressures	65
4.3	Approximate Munk and Prim Similarity Principle	70
V.	CONCLUDING REMARKS	92
	BIBLIOGRAPHY	96
	APPENDICES	99
A.	Ejector Thrust Improvement Over an Isolated Nozzle	100
B.	Ejector Community Noise Problem	102
C.	Calibration and Thrust Calculation Procedures	105
D.	Sample PLF Hydraulic Calibration Plots	108
E.	Development of Governing Equations for the Munk and Prim Principle	115

NOMENCLATURE

English

A	area
a	acceleration
C_{ds}	STA nozzle discharge coefficient
C_p	specific heat at constant pressure
C_t	STA nozzle thrust coefficient
dbA	A-weighted noise reading in decibels
F	force
g	gravitational constant
L_c	chord length
L_t	throat length
LFDH	horizontal diffuser pressure load on the fuselage side
LFDV	vertical diffuser pressure load on the fuselage side
LFIH	horizontal inlet pressure load on the fuselage side
LFIV	vertical inlet pressure load on the fuselage side
LWDH	horizontal diffuser pressure load on the wing side
LWDV	vertical diffuser pressure load on the wing side
LWIH	horizontal inlet pressure load on the wing side
LWIV	vertical inlet pressure load on the wing side
M	Mach number
m	mass

\dot{m}	mass flow
NPR	nozzle pressure ratio
P	static pressure
P_∞	free stream static pressure
R	real gas constant
T	thrust, static temperature
t	time
V	velocity
W	weight flow
W_a	actual mass flow rate measured by the flow measuring nozzle (lbm/s)
W_i	Ideal mass flow rate calculated at the STA nozzle entrance (lbm/s)

Greek

γ	specific heat ratio
ρ	density
ϕ	thrust augmentation ratio
ϕ_R	thrust augmentation ratio at a chordwise rake location

Subscripts

a	ambient conditions
e	nozzle exit
o	total (stagnation) conditions
p	primary flow

- S static conditions
- s secondary flow
- T total (stagnation) conditions
- 2 diffuser entrance location
- 3 diffuser exit location

Superscripts

- * nozzle critical properties (Mach = 1)
- vector

LIST OF TABLES

Table		Page
I	Seasonal variations in temperatures	60
II	Pressure forces ($\text{lb}_f/\text{in.}$ at $\text{NPR} = 2.7$, $T_p = 1560 \text{ R}$)	67

LIST OF FIGURES

Figure		Page
1.1	Simple ejector schematic	2
1.2	Ejector applications	5
1.3	Tactical advantages of STOVL (Air Force)	7
1.4	Tactical advantages of STOVL (Navy)	7
1.5	Artist's conceptions of possible supersonic STOVL aircraft	10
1.6	STOVL propulsion concept options	11
1.7	Tandem fan propulsion concept	12
1.8	Ejector installed on the PLF	20
2.1	Artist's conception of a full-scale aircraft test on the PLF	24
2.2	Powered lift test facility and air supply sub-system	26
2.3	PLF thrust frame and force measuring system	29
2.4	ASME flow nozzle	29
2.5	Data acquisition / retrieval	31
3.1	Original ejector inlet configuration	38
3.2	Primary air supply duct	40
3.3	Heater exit instrumentation ring	40
3.4	Ejector inlet instrumentation ring	40
3.5	Ejector instrumentation	42
3.6	Ejector exit plane	43
3.7	Flow visualization paint dots	47

3.8	Photo of ejector plan view. Inlet door replaced with radius shown.	49
3.9	Cross-sectional view of ejector	50
3.10	Sketch of ejector plan view	50
4.1	Test adjusted ejector performance prediction	55
4.2	Cold flow ejector performance	55
4.3	Cold flow ejector performance at NPR=2.7. Inlet door radius and nozzle root fairings installed.	57
4.4	Cold flow spanwise pressure distribution: NPR=2.7, chord location = 40 in..	57
4.5	Cold flow primary nozzle adjustment: NPR=2.7	58
4.6	Cold flow end plate inlet adjustments: NPR=2.7	61
4.7	Effect of seasonal temperature variation on cold flow performance	61
4.8	Hot flow ejector performance	63
4.9	Ejector performance at NPR = 2.7	63
4.10	Design point ejector performance: NPR=2.7, $T_p=1560$ R	66
4.11	Surface static pressure distributions: NPR=2.7, $T_p=1560$ R	66
4.12	Horizontal pressure loads: $T_p=1560$ R	68
4.13	Vertical pressure loads: $T_p=1560$ R	68
4.14	Effect of nozzle pressure ratio on throat Mach number: $T_p=1560$ R	69
4.15	Chordwise variation of throat Mach number: $T_p=1560$ R	69
4.16	Effect of heat transfer and shear stresses on P_T and M	73

4.17	Effect of temperature on ejector thrust augmentation	73
4.18	Chordwise ejector exit Mach number distributions	75
4.19		
(a)	Ejector exit total pressure distribution. $T_p = 517$ R	76
(b)	Ejector exit total pressure distribution. $T_p = 1560$ R	77
(c)	Ejector exit Mach number distribution. $T_p = 517$ R	78
(d)	Ejector exit Mach number distribution. $T_p = 1560$ R	79
4.20		
(a)	Ejector exit total pressure contours of the center nozzles. $T_p = 517$ R	80
(b)	Ejector exit total pressure contours of the center nozzles. $T_p = 1560$ R	81
(c)	Ejector exit total pressure surface plots of the center nozzles	82
4.21		
(a)	Ejector exit Mach number contours of the center nozzles. $T_p = 517$ R	83
(b)	Ejector exit Mach number contours of the center nozzles. $T_p = 1560$ R	84
(c)	Ejector exit Mach number surface plots of the center nozzles	85
4.22	Normalized pumping parameter at constant ejector area ratio	88

4.23	Performance vs. nondimensional flow	90
A.1	Convergent nozzle pressure distribution	101
B.1	Acoustic geodesic dome	104
D.1	PLF hydraulic calibration runs: R1	109
D.2	PLF hydraulic calibration runs: R2	110
D.3	PLF hydraulic calibration runs: R3	111
D.4	PLF hydraulic calibration runs: R4	112
D.5	PLF hydraulic calibration runs: R5	113
D.6	PLF hydraulic calibration runs: R6	114

CHAPTER I

INTRODUCTION

What is an ejector? Basically, an ejector is a mechanically simple pumping device consisting of a nozzle exhausting into a diffuser or shroud. Figure 1.1 highlights the main components and pertinent terminology of a simple ejector. Ejectors operate by inducing large amounts of air (secondary flow) from the ambient through the entraining action of the primary nozzle jet shear layer. This entrainment is enhanced through the use of a shroud.

As the primary jet expands, the shroud induces a shear layer motion and acceleration of the secondary flow. An increase in the secondary flow velocity results in a local static pressure decrease (according to the Bernoulli equation) in the vicinity of the primary nozzle exit. The lower back pressure in the vicinity of the primary nozzle discharge then allows the primary nozzle exhaust to expand to a pressure lower than ambient, and therefore have a higher velocity and kinetic energy than if there were no shroud. As a result, enclosing the primary nozzle with a shroud provides greater total thrust than the primary nozzle alone, improving the kinetic

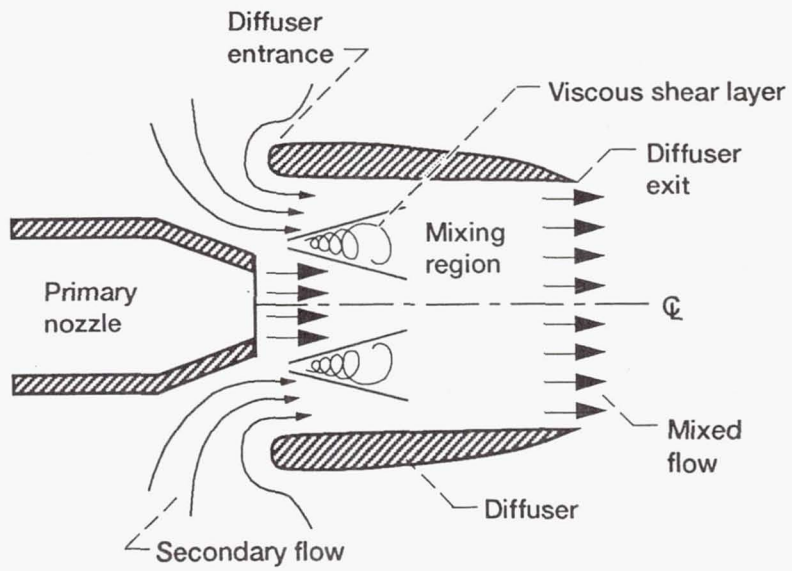


Figure 1.1.—Simple ejector schematic.

energy conversion of the total available energy of the primary nozzle (see Appendix A). Turbulent mixing in the viscous shear layer is responsible for transferring energy between streams, imparting motion to the secondary flow.

The ratio of the total thrust to the ideal thrust of a primary nozzle (exhausting to the same ambient back pressure) is called the thrust augmentation ratio (ϕ), defined here as:

$$\phi = \frac{T_p + T_s}{(T_p)_{\text{isentropic}}} \quad (1)$$

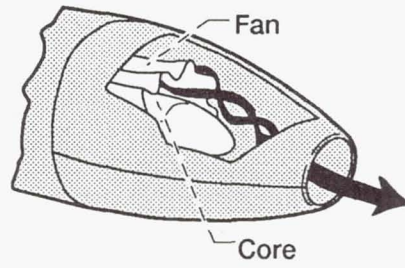
Although the idea of thrust augmentation may lead to the belief that you "get something for nothing", in actuality an ejector simply makes better use of the total internal energy available.

So far, the discussion has been about ejector fluid phenomena. However, the ejector geometry is also important, especially of the inlet and nozzles. Since the inlet directs the incoming secondary flow, separation or stagnation regions that would hinder the mixing process are undesirable. As for the primary nozzles, optimal jet expansion should be obtained without restricting either the amount of secondary flow, or the mixing process.

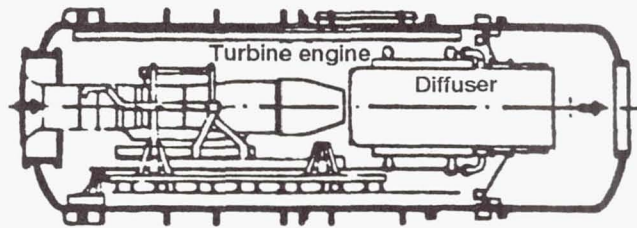
It is clear that in ejector design there are two parts to the "ejector problem". The first is to find the nozzle and inlet geometries that most efficiently enhance mixing between the primary and secondary streams, while the second is to understand the relationship between the shroud geometry and mixing layer characteristics.

Ejectors play a vital role in many applications, from food processing to air conditioning. For example, basic jet/shear layer interactions were employed in the design of the air conditioning system for the Sistine Chapel (Bullock, 1989). Ejector nozzles have also been examined for tailpipe and nozzle cooling in high-speed jet aircraft. These ejectors must be as short as possible to save weight, but only need to pump a small amount of secondary air.

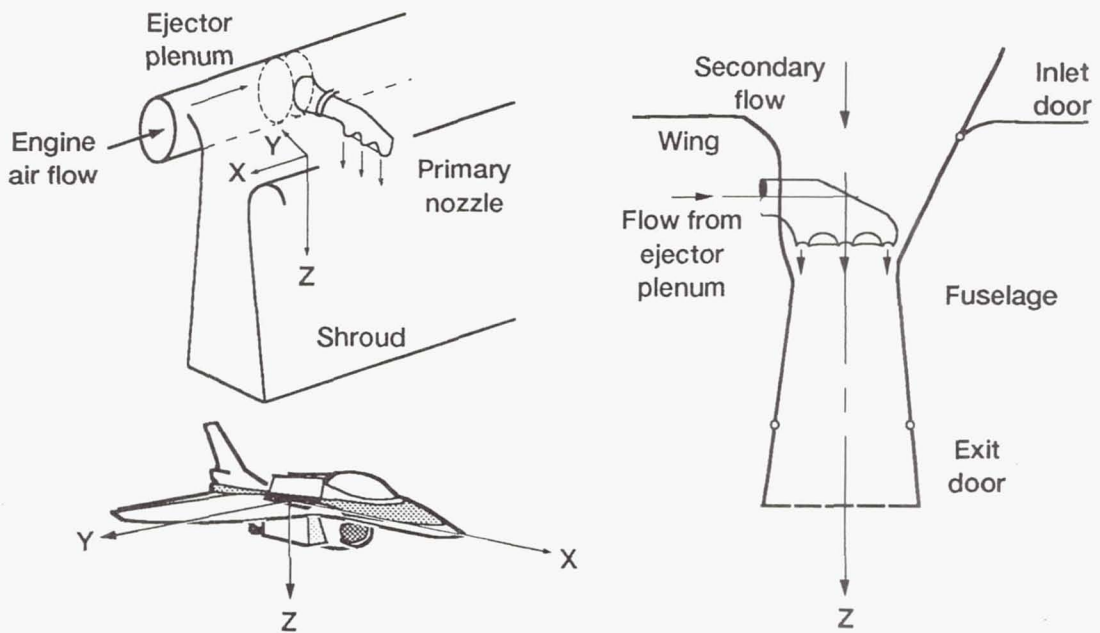
Several aerospace ejector applications are depicted in Figure 1.2. The Turbofan Forced Mixer or mixer ejector (Figure 1.2(a)) is used for noise suppression of a jet engine exit nozzle by mixing the core and fan flow before the nozzle exit (Presz, 1991). This mixing lowers both the velocity and temperature of the exhaust flows. Pumping ejectors such as the turbine engine test installation (Figure 1.2(b)), act as mass flow augmenters to capture and expel free-jet flows (McAmis and Bartlett, 1991). The addition of the diffuser allows the system to act as an ejector; entrainment of the secondary flow allows a more efficient removal of the exhaust gasses. Thrust augmenting ejectors (Figure 1.2(c)) could provide vertical lift for supersonic short take-off and vertical landing (STOVL) aircraft. Here, heated engine air is ducted to a row of nozzles between the wing root and fuselage of the aircraft, exhausting into a rectangular diffuser. It is this last type of ejector application that will be discussed in this thesis.



(a) Turbofan forced mixer.



(b) Typical turbine engine test installation.



(c) Vertical lift aircraft configuration.

Figure 1.2.—Ejector applications.

1.1 STOVL/Powered-Lift Background

Supersonic short take-off and vertical landing (STOVL) aircraft are potential candidates for future high performance fighter aircraft. Successful STOVL designs depend heavily on propulsion system technology development, where both vertical lift and forward thrust must be attained without drastically increasing the aircraft's weight or cross sectional area. Transition between vertical and forward flight is a critical phase of STOVL flight, and in part determines the feasibility of a propulsion concept. The specific technology where a single propulsion system provides power for vertical lift, hover, and forward flight is called powered lift.

The main benefit of powered-lift technology is that it allows aircraft operation from short, or non-existent runways. Two military scenarios of interest include the Air Force operation from short or damaged runways near the battle field (Figure 1.3), and the Navy operation from damaged carrier decks or other smaller aircraft carrying ships (Figure 1.4). Various application scenarios give rise to the many acronyms associated with powered lift: short take-off and landing (STOL), vertical take-off and landing (VTOL), short take-off and vertical landing (STOVL), and combined performance, or V/STOL. In addition, powered-lift technology improves aircraft performance by allowing steep climbs for noise abatement--a current concern for all aircraft--and greatly refining combat maneuverability.

With so many different "performance" options, why choose STOVL? Basically, the STOVL aircraft is the most operationally flexible high performance aircraft

Operation from damaged runways



Operation from small fields near battle area

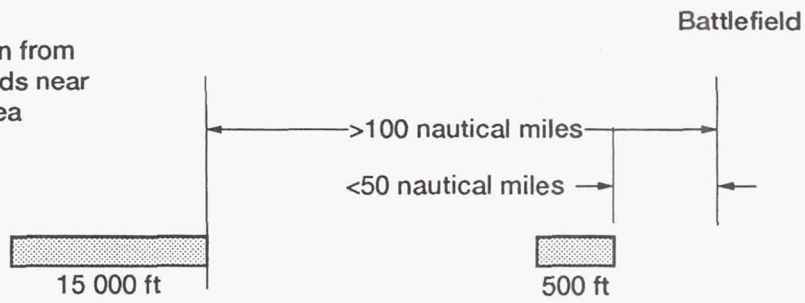
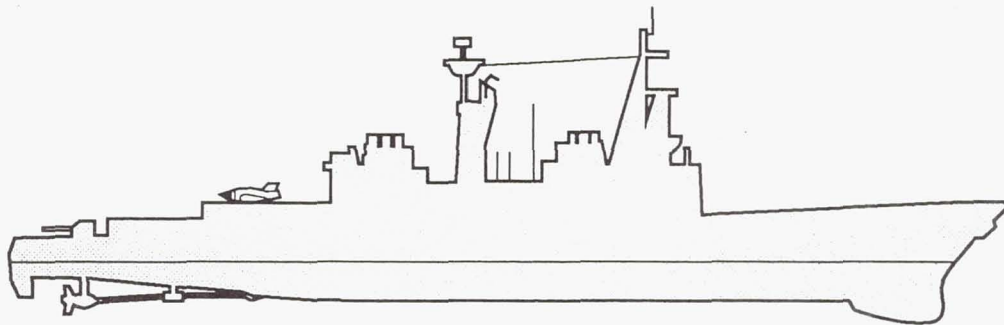
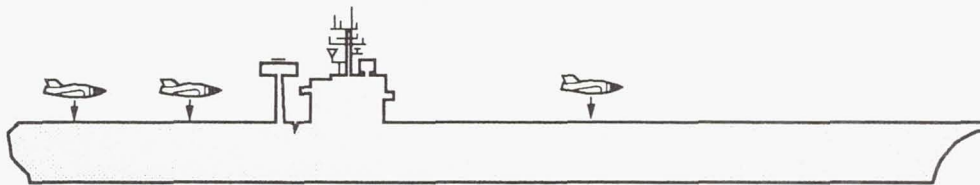


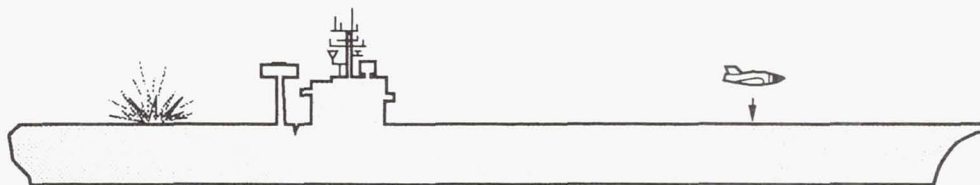
Figure 1.3.—Tactical advantages of STOVL (Air Force).



Smaller aircraft-carrying ships



Shorter carrier-operations cycle times



Operation from a damaged carrier deck

Figure 1.4.—Tactical advantages of STOVL (Navy).

(Kidwell, 1983). Operation in the STOVL mode would take advantage of the large increase in take-off weight capability provided by a short ground run. In this case, the engine would be sized for maximum performance as a STO vehicle at maximum gross weight, using both propulsive and aerodynamic lift. With propulsive lift alone, vertical take-offs and landings could occur at significantly reduced gross weight; the engine would be too small to provide enough vertical lift at the maximum gross weight. For vertical take-offs this reduced gross weight would most likely translate into less fuel, thus decreasing the mission potential of the aircraft. Also, the cost compared to STOL or CTOL (conventional take-off and landing) is going down, while advancing technology continues to increase propulsion system thrust/weight ratio (Deckert, 1985). As explained by Kidwell and Lampkin (1983), "Today, it is no more difficult to build a supersonic STOVL aircraft than it is to build a supersonic CTOL aircraft. A more arduous task is to design this aircraft to have an uncompromised operational capability."

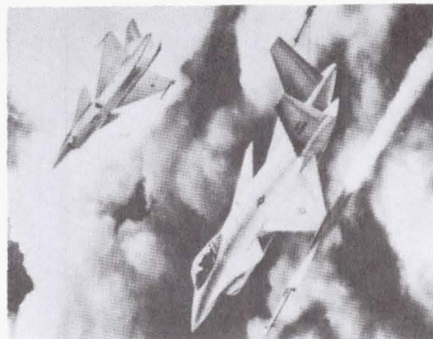
Although there have been many aircraft concepts, the British Aerospace Harrier is the only combat-tested powered-lift aircraft in the world. In this aircraft, a separate flow bypass engine (fan and core flow are separate) provides powered lift by supplying two forward nozzles with fan flow, and two rear nozzles with core flow. Unfortunately, the two rear nozzles create a very hot jet flow which result in severe exhaust temperature ground effects. The Harrier is also a subsonic aircraft nearing the end of its service life. Supersonic STOVL is a logical replacement, but the lack of a detailed customer system specification has led to many propulsion and airframe

configuration variants. A joint US/UK conference held in Farnborough, in June 1983, concluded that an affordable future STOVL fighter would most probably have a single engine, with lift and cruise capabilities combined in the same powerplant system (Levine, 1989). There are currently four different powered lift concepts having the greatest near-term potential (see Figure 1.5). These engine systems are described below and pictured in Figures 1.6 and 1.7.

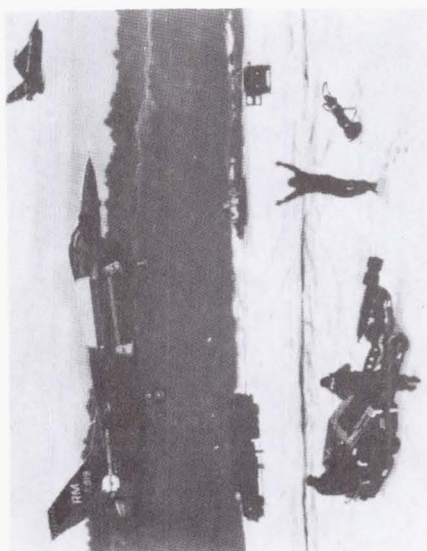
1. **EJECTOR LIFT:** Forward flight employs a single aft nozzle with afterburning capability. For vertical flight, the entire core & fan mixed flow is ducted forward of the aircraft center of gravity to ejectors located in the wings, and to a small ventral nozzle located aft of the center of gravity.
2. **MIXED FLOW VECTORED THRUST:** The core and fan flows are mixed before exiting the engine. This mixing of the cooler fan flow with the hot core flow thus lowers the engine exit temperature. For cruise and maneuver flight, the entire mixed engine flow exhausts through an aft nozzle which has pitch and yaw vectoring capability. For vertical flight, the entire mixed engine flow exits through two vectorable nozzles located just forward of the aircraft center of gravity. A small trimmer nozzle (downstream of the center of gravity) provides balance.
3. **REMOTE AUGMENTER LIFT SYSTEM (RALS):** A vectorable 2-D nozzle directs all engine flow for forward flight. For vertical flight, the core



Remote augmented lift system



Hybrid tandem fan
C-89-02675

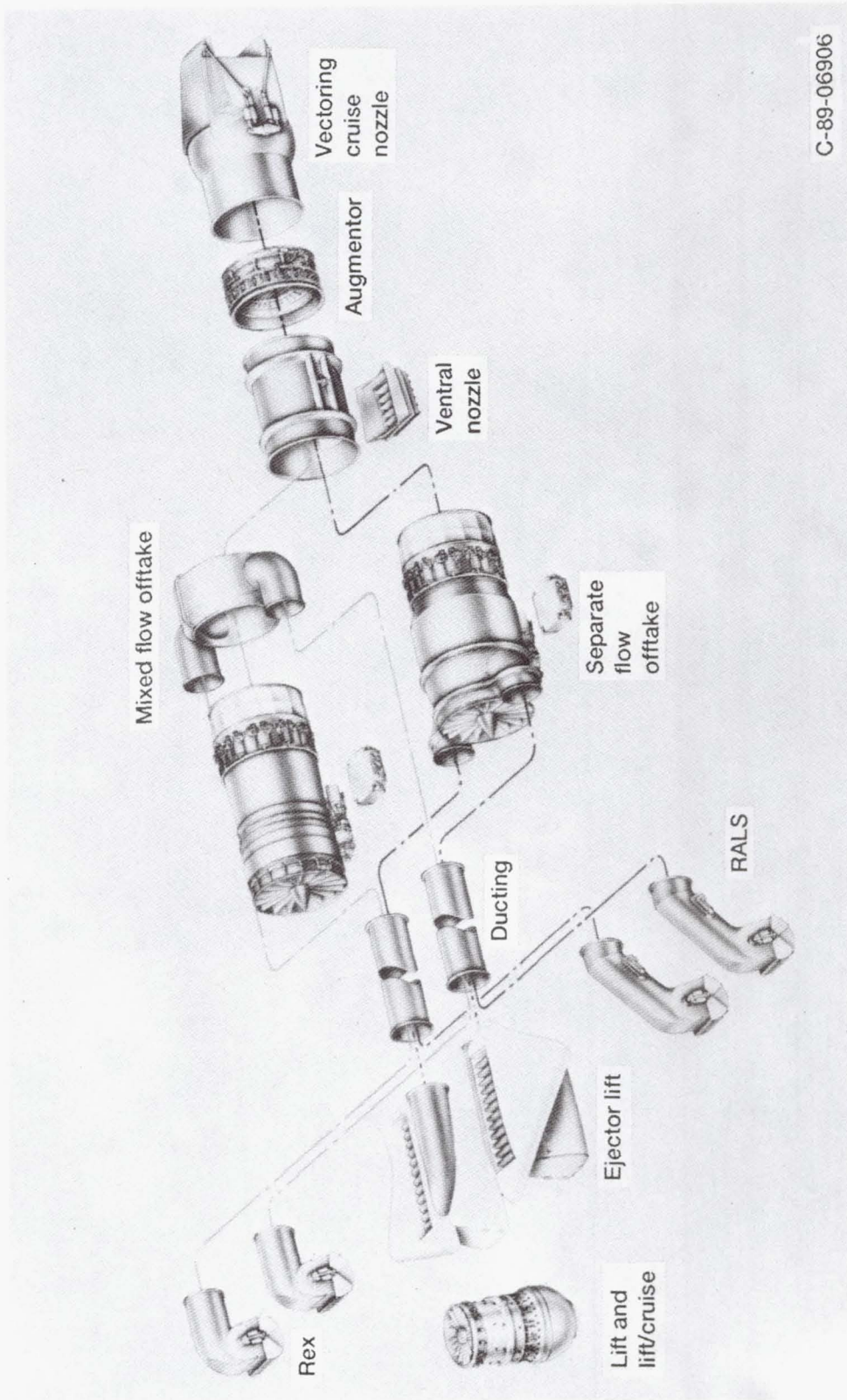


Ejector augmentor



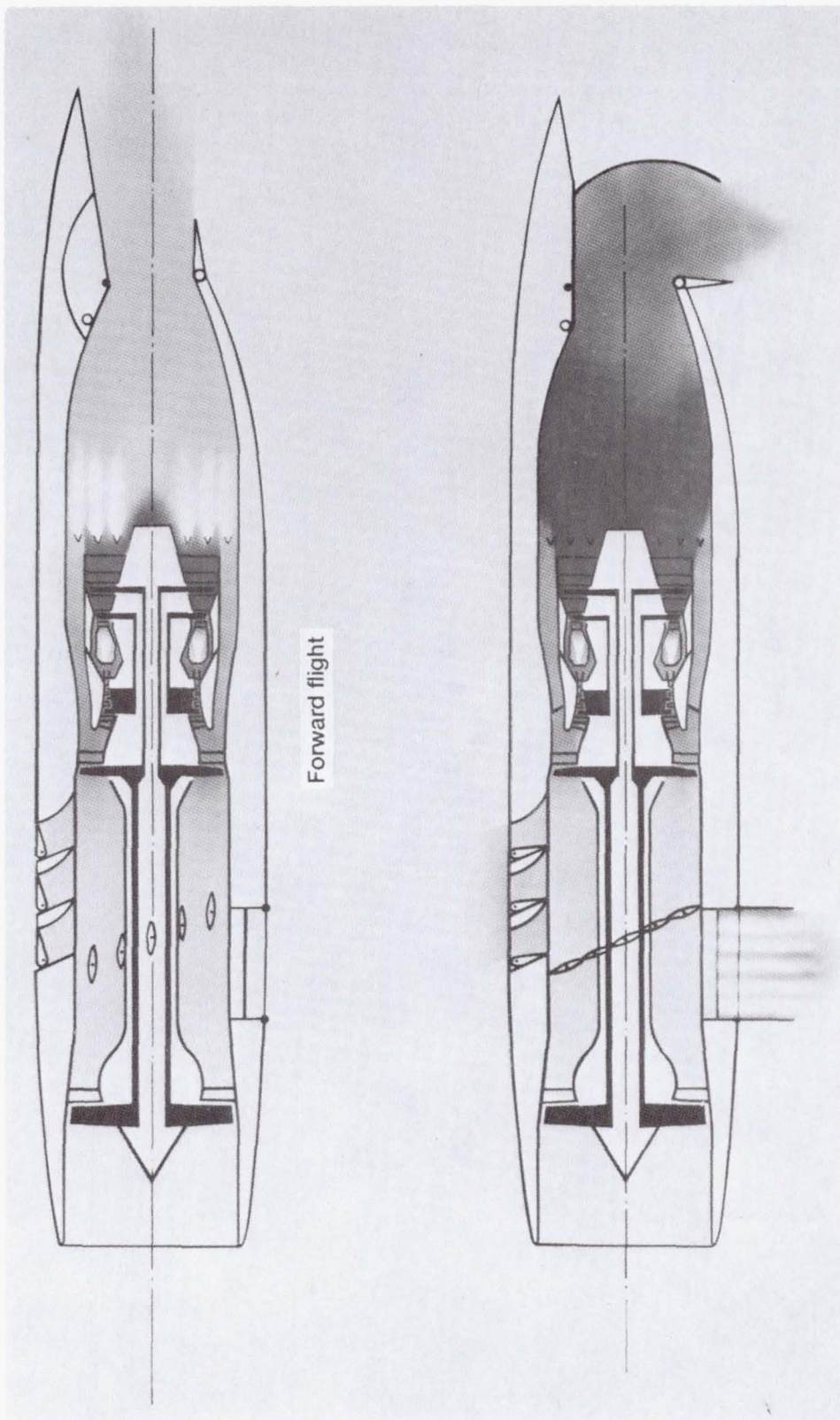
Mixed flow vectored thrust

Figure 1.5.—Artist's conceptions of possible supersonic STOVL aircraft.



C-89-06906

Figure 1.6.—STOVL propulsion concept options.



C-84-4292

Vertical lift

Figure 1.7.—Tandem fan propulsion concept.

flow exits through the 2-D nozzle while the fan flow is burned at remote nozzles forward of the aircraft center of gravity.

4. **TANDEM FAN:** The tandem fan is a variable cycle engine concept with fan stages that can be separated. In forward flight the mixed engine flow exhausts through a 2-D aft vectoring nozzle with afterburning capability. For vertical lift, the fan flow is exhausted through two vectoring nozzles while the core flow passes through the vectoring 2-D nozzle.

Figure 1.6 illustrates that each concept (mentioned above) relies on the reconfiguration of a basic set of components. Since little is known about the individual component flow behavior in these applications, there is a need for experimental testing.

As stated above, one method of achieving STOVL capability in an aircraft is through the use of thrust augmenting ejectors. As shown in Figure 1.2(c), engine air is ducted through a row of nozzles between the wing and fuselage of the aircraft. Thrust augmentation results when the entrained secondary air mixes with the primary flow, increasing total mass flow and thus the vertical thrust.

The original STOVL ejector concept supplied only fan flow (760 R) to the ejector primary nozzles using a separate flow engine (Corsiglia, et.al., 1989), but current proposals would use a mixed flow engine which would provide nozzle air at significantly higher temperatures (1560 R). In this application the ejector functions

like the fan on a high bypass engine: thrust is increased by accelerating a large mass of air drawn from the atmosphere. The mixing reduces both the velocity and temperature of the lift jets, reducing the hazard to ground personnel and the possibility of damaging the airframe. Another "plus" is that when integrated with the wing, the ejector exhaust flow acts as a jet flap to increase wing lift and improve performance.

However, the benefit of using ejectors is seriously offset by its complexities. The ejectors must be short enough to satisfy space limitations, but still provide a high enough thrust augmentation to overcome the additional component weight requirements and drag increases. The transition from vertical to horizontal flight also presents a considerable mechanical flow switching problem. For ejector transition, baseline mission studies suggest that a thrust augmentation ratio of 1.7 or greater is needed. To advance the state-of-the-art in aerospace ejector applications, our understanding of the ejector fluid dynamics needs to be refined. This knowledge will guide ejector integration with a practical aircraft configuration.

1.2 Literature Review

Ejectors are used in a wide variety of applications due to their simplicity, lack of moving parts, and reliability. It comes as no surprise then, that there is extensive literature available, both theoretical and experimental. Since it is not within the scope of this thesis to exhaustively discuss ejector research history, only particularly

relevant literature will be presented.

A noteworthy report on ejector technology is the work of Porter and Squires (1981), which contains a comprehensive listing of over 1600 ejector references. More recently, Deckert and Franklin (1985) discuss the issues involved when incorporating the ejector concept in a supersonic STOVL fighter. Many other publications, including those by Kidwell and Lampkin (1983), Batterton and Blaha (1987), and Biesiadny (1991), discuss the possible role of ejectors in future Supersonic STOVL aircraft and supporting research programs.

A more in-depth study of the development of ejector design for STOVL aircraft is presented by Whittley and Gilbertson (1984), and Garland (1987), who comment on the development of ejector flaps and thrust augmenting lift ejectors that has occurred at the de Havilland Aircraft of Canada. Development of ejectors has naturally led to scale model tests of V/STOL (vertical/short take-off and landing) aircraft. Whittley and Koenig (1980) describe one such experimental program. This includes large scale static tests powered by a G.E. J-85 engine, small and large scale ejector development tests performed at de Havilland, and finally large scale static tests in the NASA Ames Research Center's 40'x 80' wind tunnel. As a result of the wind tunnel test, a thrust augmentation of around 1.69 was obtained for the large scale cold flow development tests, and 1.6 for the J-85 powered model at 1750 R (1290°F).

Another experimental STOVL program was the ejector-powered E-7A. Static tests of a full-scale ejector were performed at the NASA Lewis Research Center's

"Page missing from available version"

effort (Yang, Ntone, Jiang, and Pitts; 1985), the design process and experimental investigation of short thrust augmenting ejectors is discussed.

Perhaps the most important process occurring (and the least understood) in the ejector is the turbulent mixing of the viscous shear layer; it is this process that influences the secondary flow entrainment. Experimental measurement of the mixing layer using laser Doppler velocimetry (LDV) systems and Schlieren photographs have been examined by Bernal and Sarohia (1984) and Goebel and Dutton (1990).

Computer models are used extensively to provide some insight on the ejector flowfield characteristics. Bevilaqua and DeJoode (1978) use a finite difference model for an analysis in which elliptic Navier-Stokes equations are employed for the inviscid outer solution, and a reduced parabolic set of governing equations for the viscous inner solution. A solution matching procedure is then used to incorporate the two routines. Drummond (1988) introduces a method for predicting both steady-state and transient thrust augmenting ejector characteristics. This method blends the classic self-similar turbulent jet descriptions with a control volume analysis of the mixing region. A few other numerical ejector analyses are presented by Deese and Agarwal (1988), and Salter (1975).

General purpose codes have also been used to evaluate ejector flows. Garrard, Phares, and Cooper (1991), for example, use the PARC code to calibrate a variety of propulsion flows, including the ejector-like free-jet flows. Computer models are even used in the ejector design process. For example, DeFrate and Hoerl have extended a one-dimensional ejector analysis to optimize the design of jet ejectors for

the suction of gases having arbitrary molecular weight and temperature. However, since ejectors contain 3-D flow phenomena, care must be taken when applying a one-dimensional prediction. These predictions seem to work best when analyzing a good ejector design, but are not design tools themselves.

The problems involved with scale effects (both aerodynamic and thermal) are important aspects of ejector design. Most of the available research reports deal with the aerodynamic scale effects (applying sub-scale laboratory tests to full-scale applications). The general conclusion seems to be that there are no significant aerodynamic scale effects present (Garland and Gilbertson, 1990). However, there are numerous pitfalls where loss of performance can arise. For this reason, ejector work is best when conducted full-scale.

But what about thermal effects? Despite the vast amount of references available on ejectors, only a small percentage relates to scale effects, and even less on the effects of primary flow total temperature. There is, however, some very useful documentation on similarity principles. One principle in particular is described by Munk and Prim (1947), and is applicable to ideal gasses. Both Greitzer, Patterson, and Tan (1985) and Presz and Greitzer (1988) apply an approximation of this thermal scaling principle to mixer ejectors.

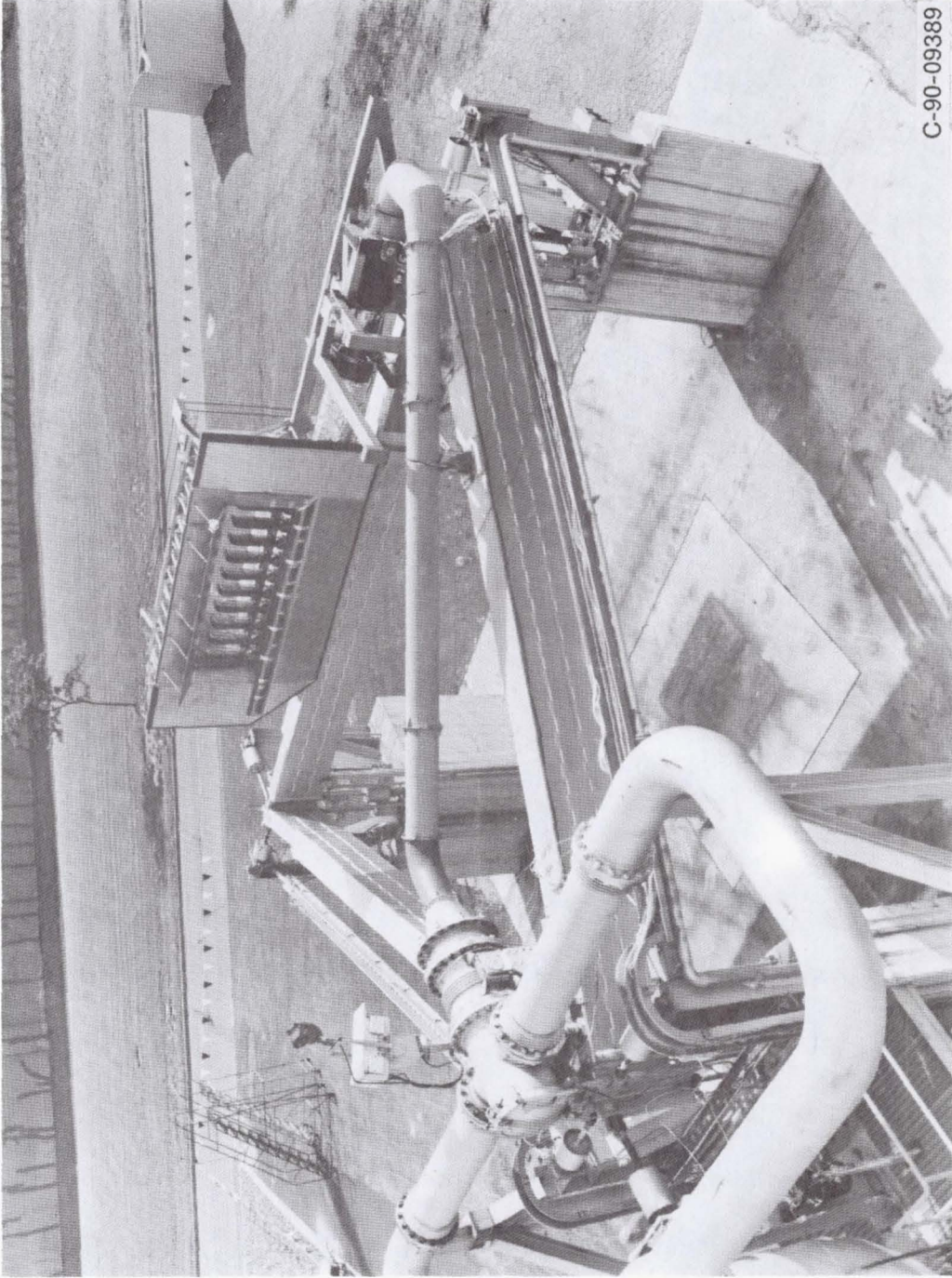
The underlying message behind much of the experimental work is that not enough is known about the internal workings of ejectors to accurately use sub-scale models. Full scale models need to be tested, and at full temperature. Practical applications have shown that ejector design is an art, not a science.

1.3 Scope of Work

Although properly designed ejectors can perform very well with cool primary air, proposed supersonic STOVL configurations require that the engine exhaust (mixed core and fan flow) is ducted to the ejectors for vertical maneuvering. As a consequence, the gas temperature available for the ejector primary nozzles is now elevated to mixed flow levels. To examine specific performance effects, the NASA Lewis Research Center--in conjunction with Boeing Military Airplanes and Boeing de Havilland--have tested a full-scale lift ejector at primary flow temperatures ranging from ambient to 1560 R (1100°F), and primary nozzle pressure ratios up to 3.0. This test is the focus of the thesis.

This unique, ejector testing was performed at the NASA Lewis Research Center's Powered Lift Facility (PLF) from June, 1990 thru January, 1991; and signifies the first design point (both pressure and temperature) testing of a full-scale thrust augmenting ejector. The design point of this ejector was at a primary-nozzle pressure ratio of 2.7 and a primary-air temperature of 1560 R. Figure 1.8 shows the top view (secondary flow inlet) of the full-scale experimental model as installed on the PLF. For experimental purposes, the model was turned on its side, measuring thrust in the horizontal direction.

The major objectives of this test were to measure thrust augmentation levels for both "cold" and "hot" primary flows in order to validate the ejector design and determine the effects of primary jet temperature on thrust augmentation. To



C-90-09389

Figure 1.8.—Ejector installed on the PLF.

accomplish these objectives, two series of tests were conducted:

1. Cold flow primary, where the supply air was not heated.
2. Hot flow primary, where the supply air was heated over a range of temperatures up to a maximum temperature of 1560 R.

In the cold flow tests, several modifications were made to improve the ejector performance. Hot flow testing was then performed with a similar configuration; only slight changes were made to allow for thermal expansion of the ejector duct.

The cost and complexity of testing ejector models could be greatly reduced if one could neglect temperature effects of the primary nozzle when determining ejector performance. Theoretically, this could be accomplished if a suitable jet similarity principle could be established. An approximate technique has been proposed and applied by Greitzer, Patterson, and Tan (1985) for viscous heat conducting flows (mixer ejector nozzles). Basically, this technique states that for fixed geometry and inlet total pressure distributions, the Mach number and total pressure along the streamlines are independent of the upstream total temperature distribution. This concept is an extension of the Munk and Prim Principle (Munk and Prim, 1947) for steady isentropic flows; the current technique includes the non-isentropic (viscous) effects.

The purpose of this thesis is to examine the cold and hot experimental ejector data and assess the validity of the Approximate Munk and Prim similarity principle for this specific ejector. Of interest were the effects of primary nozzle temperature, inlet geometry, and nozzle geometry on performance. To help determine these

relationships, test results are presented through plots of thrust augmentation vs. nozzle pressure ratio and ejector primary temperature. Other results include normalized pumping, and exit rake thrust augmentation ratio, Mach number and total pressure profiles. The degree of dependence of the normalized ejector performance on the primary nozzle total temperature is also examined.

CHAPTER II

EXPERIMENTAL FACILITY

The NASA Lewis Research Center's Powered Lift Facility (PLF) is primarily used to provide an experimental technology base for the development of supersonic short take-off and vertical landing (SSTOVL) aircraft propulsion* systems. The PLF is designed to accommodate several different categories of test programs in support of the analytical and experimental research on SSTOVL, and has the unique ability to test full-scale components or complete models, including the potential to test complete aircraft (see Figure 2.1). The research objectives supported by the PLF are to:

1. Assess analytical codes through model and full-scale tests.
2. Establish a data base for systems in which analytical codes may not be developed.
3. Determine critical parameters and their system sensitivity factors.

With renewed interest in a high speed civil transport aircraft, the PLF also lends itself to the testing of components that could have a significant impact on the

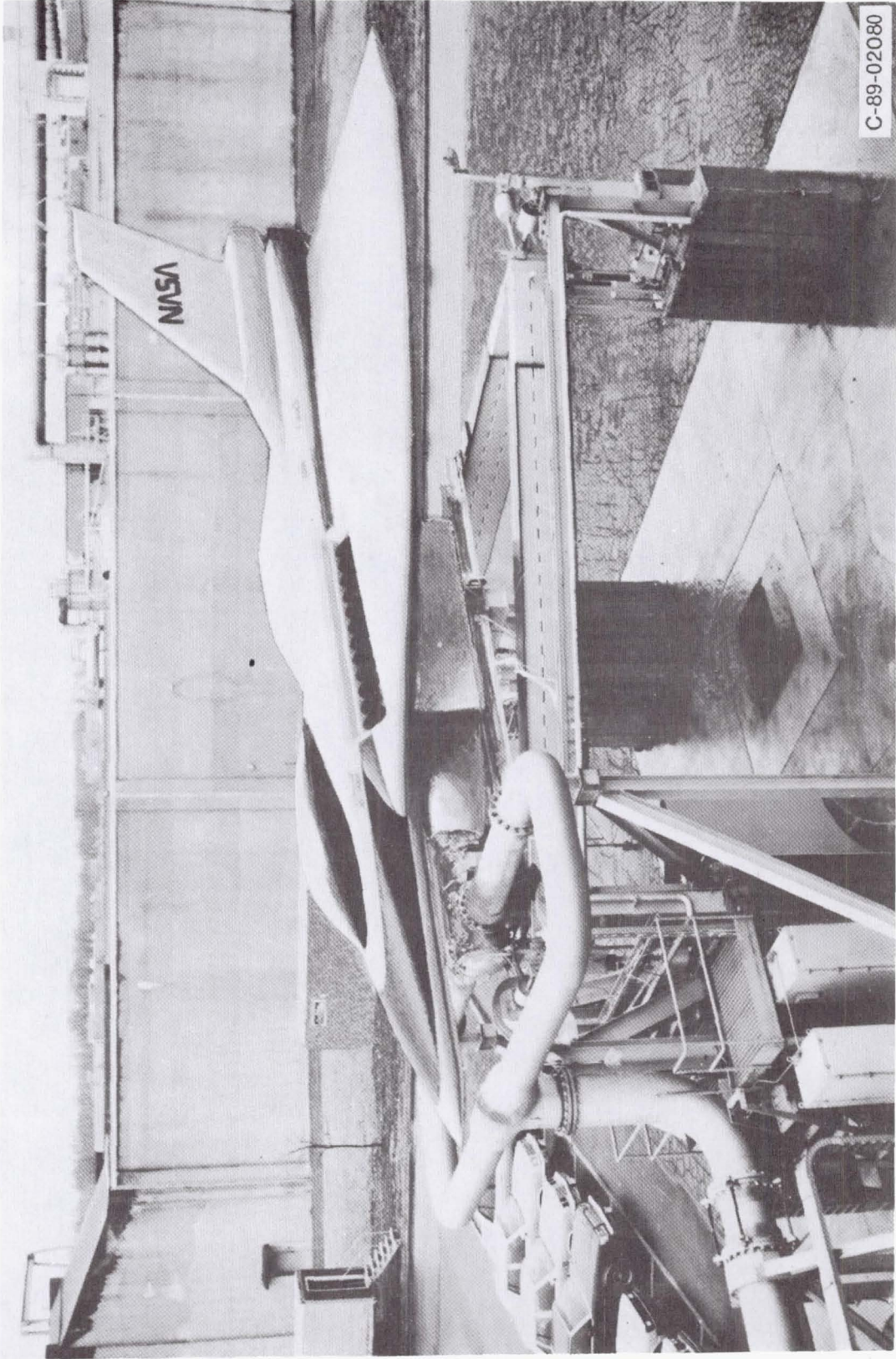


Figure 2.1.—Artist's conception of a full-scale aircraft test on the PLF.

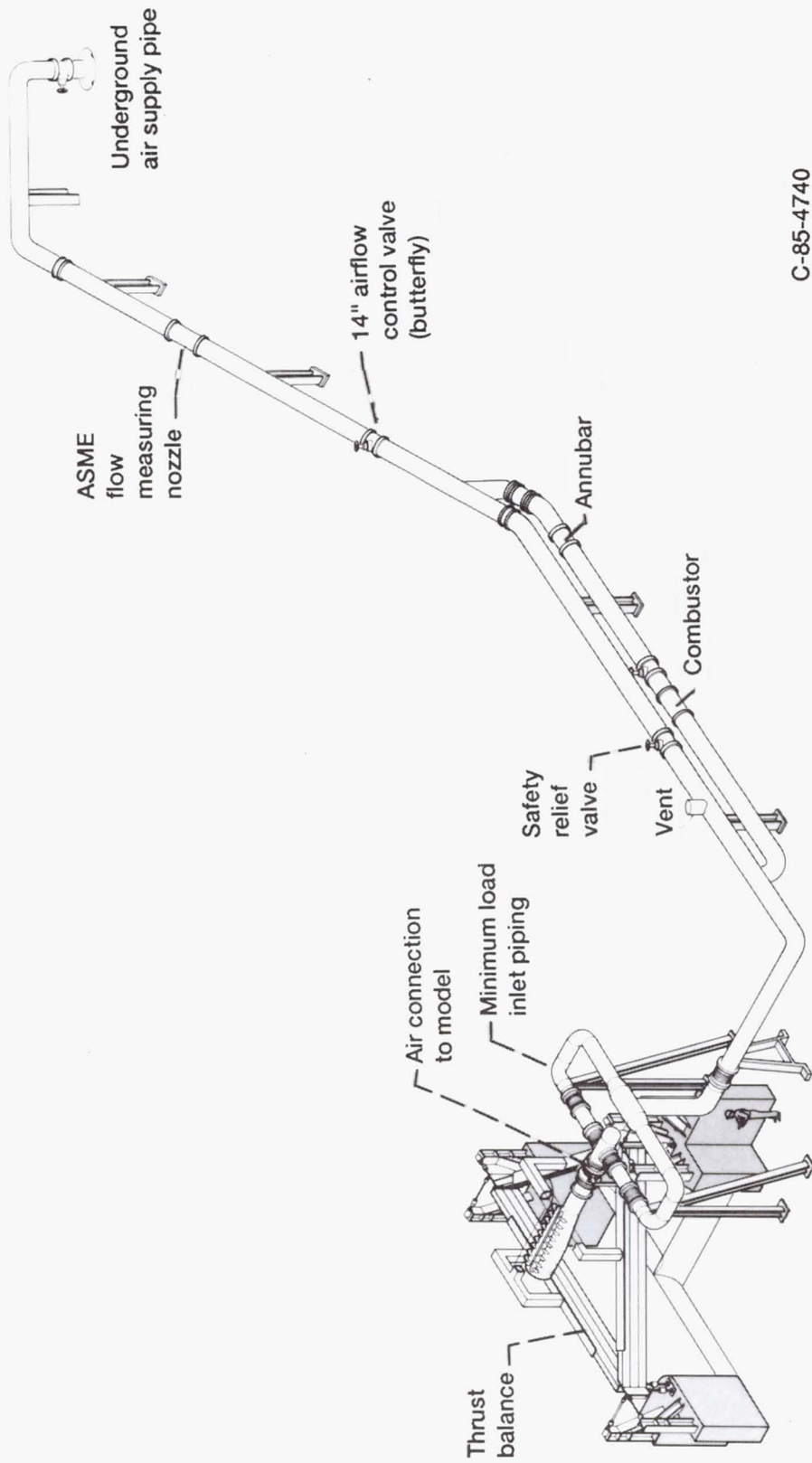
performance of such an aircraft. These components include near-scale or full-scale inlets, nozzles, and engines with flight hardware. This facility will also be useful in establishing the propulsion control requirements and techniques for integrated aircraft and propulsion flight control systems designs, including steady-state and transient subsystem component effects on those designs.

2.1 Facility Description

The PLF is an outdoor test facility comprised primarily of a thrust balance and combustion air supply (Figure 2.2). All facility operations are directed from the control room located in an adjacent building, while the test site is monitored through video cameras. Note that this is not a small laboratory test rig, but a full-scale aircraft propulsion test facility. Therefore, safety concerns dominate throughout the test program, and often restrict the nature of data that can be collected. Appendix B contains information on the PLF noise problem, which is one of the main testing concerns. More examples of these safety regulations appear in following sections.

2.1.1 Thrust Balance

The most prominent feature of the Powered Lift Facility is the triangular thrust frame, or thrust balance. This thrust balance measures 30 ft. on a side and is mounted 15 ft. off the ground on three concrete pedestals. A multi-directional force measuring system is capable of measuring thrust (force) levels in three directions as



C-85-4740

Figure 2.2—Powered lift test facility and air supply sub-system.

well as moments about all three axes, i.e. roll, pitch, and yaw moments of the test section. There are three vertical load cells (25000 lb), two lateral (5000 lb) and one axial (25000 lb). Figure 2.3 shows the load cell locations. Experimental load cells are labeled R1-R6. Calibration load cells will be referred to in a later section. Full-scale accuracy is approximately $\pm 1\%$ for the 25000 lb and $\pm 5\%$ for the 5000 lb load cells. Maximum allowable model weight is 40,000 lbs., and the aerodynamic effects (i.e. ground effects) of the exhaust are negligible.

2.1.2 Air Supply System

The combustion air arrives from an underground pipe originating at the main compressor building (see Figure 2.2), and then enters the thrust balance through a minimum load inlet arrangement (see Figure 2.2). This piping isolation system minimizes any load forces imposed on the thrust balance by the combustion air system, although there is still a small "tare load" that impinges on the balance, which must be accounted for (described later). Air temperature is slightly above ambient (due to the compression process) and may vary slightly throughout the test night. Air can be heated to 1660 R (1200°F) by the use of an air combustor sub-system installed on the stand in the feeder air supply line. An additional combustor (see Figure 2.2) can provide up to 760 R (300°F) simulated fan duct air temperatures. The combustors use JP5 jet fuel stored nearby in a 2000 gal. trailer. The maximum allowable line pressure and flow rate at the test section is 90 psig and 150 pps. Greater pressures are alleviated through a relief valve or a burst disc (see Figure

2.2). The facility mass flow measuring station is located in the inlet pipe upstream of the thrust frame (see Figure 2.2) and utilizes an ASME flow measuring nozzle as pictured in Figure 2.4. The accuracy of these systems is between 1/4 % and 1/2 %, and includes both scatter and experimental bias.

2.1.3 Instrumentation System

The basic instrumentation system has the capability to measure 372 steady-state air pressures (not including 12 reserved reference-to-ambient ports), 96 air temperatures, and other miscellaneous transducers for facility measurements.

Standard facility research measurements include:

1. Six experimental load cell forces
2. Supply pipe mass flow
3. Fuel flow and pressure
4. Ambient and barometric pressures
5. Ambient temperature
6. Inlet pipe pressure and temperature (before pipe enters thrust frame)

A variety of traversing rake probes and transient pressure transducers has also been used on the PLF. The probes are usually actuated with electric motors, and may contain various combinations of temperature and pressure instrumentation. Since no personnel are allowed on the stand during operation, the automation is mainly a safety feature. Moreover, the automated probes are also more accurate and less time consuming to operate.

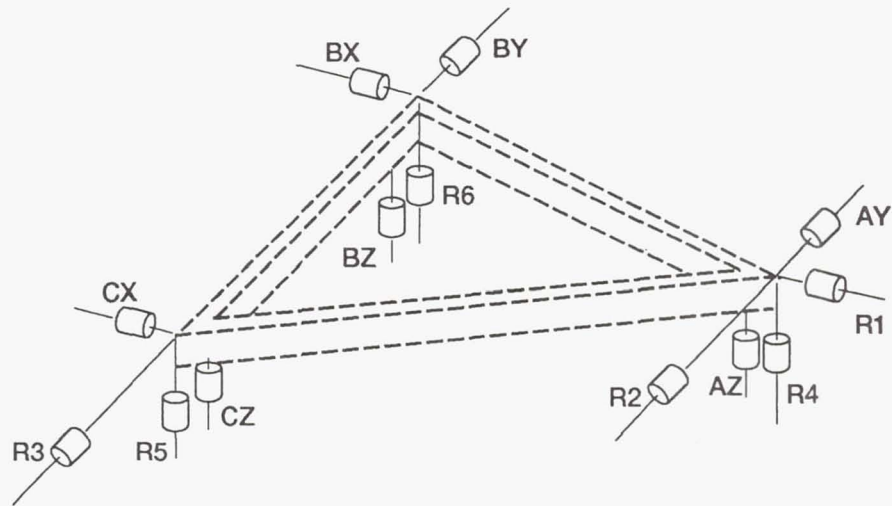


Figure 2.3.—PLF thrust frame and force measuring system.

Contour:	X	Y
0	10.646	
0.250	9.232	
0.500	8.660	
0.750	8.231	
1.000	7.877	
1.250	7.573	
1.500	7.304	
1.750	7.063	
2.000	6.845	
2.250	6.646	
2.500	6.463	
2.750	6.293	
3.000	6.137	
3.250	5.991	
3.500	5.856	
3.750	5.730	
4.000	5.613	
4.250	5.503	
4.500	5.402	
4.750	5.307	
5.000	5.219	
5.250	5.139	
5.500	5.063	
5.750	4.994	
6.000	4.930	
6.250	4.872	
6.500	4.820	
6.750	4.772	
7.000	4.730	
7.250	4.692	
7.500	4.660	
7.750	4.632	
8.000	4.609	
8.250	4.591	
8.500	4.577	
8.750	4.568	
9.000	4.563	
9.125	4.563	

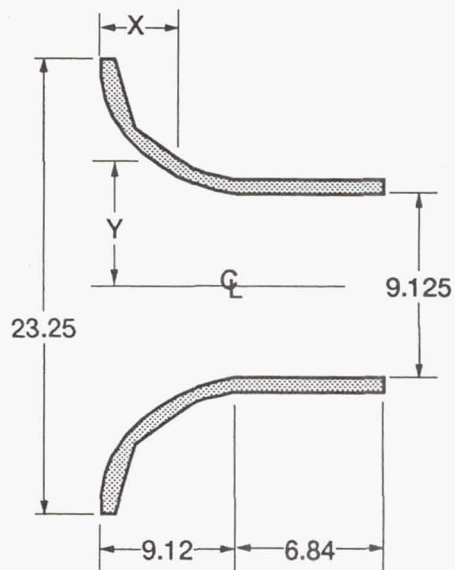


Figure 2.4.—ASME flow nozzle.

2.1.4 Data Acquisition System

The ESCORT system is a user oriented, interactive, real time data acquisition, display and recording system that provides a wide variety of computerized test support services to the steady-state experimental facilities at Lewis. The system has a DEC MicroVAX computer at the test facility, which provides the bulk of the real-time processing for the experiment. This facility computer communicates with a VAX cluster (housed in the main computer building), which provides post-run processing and data collection for archival storage. Figure 2.5 shows a diagram of the data acquisition process that will be described below.

The steady-state pressure lines run to the ESP DACU (Electronically Scanned Pressures Data Acquisition Control Unit) which contains an analog-to-digital converter microprocessor unit. From there the electrical pressure signals are sent to the control room and processed through the ESCORT ramp (remote access microprocessor--remote, because the data is retained at the location until the main ESCORT computer in the Research Analysis Center requests the data).

In addition to pressure data, thermocouple and load cell transducer data are also acquired. The load cell data enters a patchboard after signal conditioning, as shown in Figure 2.5. Thermocouple signals are sent through a thermocouple reference block before entering the patchboard. From the patchboard, data can be routed to a variety of instruments-- through digital panel meters for continuous observation, or through the Fluke interactive microprocessor. The latter is especially useful for representing load cell data graphically. The data can be "multiplexed" (or sampled

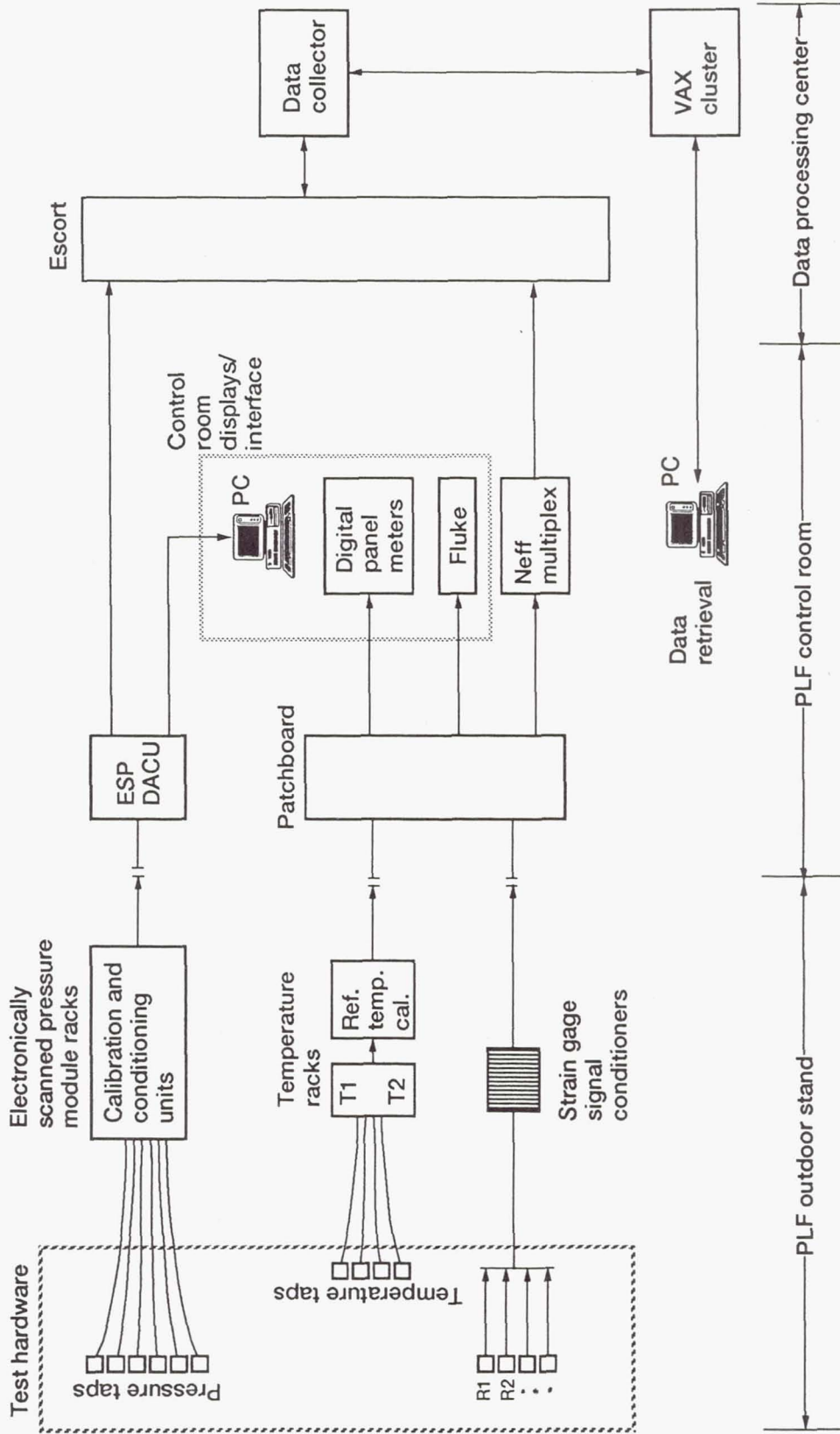


Figure 2.5.—Data acquisition/retrieval.

in sequence) and sent to the ESCORT ramp.

The data in the ESCORT ramp is continuously updated until a data point is taken. For each data point, all of the instrumentation signals are sent to the Research Analysis Center for tape storage on the VAX Cluster and further processing.

2.2 Facility Calibrations

There are three basic types of calibrations done on the PLF -- static hydraulic calibration, pressure tare calibration, and Supersonic Tunnel Association (STA) nozzle calibration. Each is a necessary and unique operation, performed separately from the others. They will be described in detail in the sections to follow. Each section will cover the reasons for each calibration, general operational hardware and instrumentation required, typical procedures, and interpretation/use of the results.

2.2.1 Static Hydraulic Calibration

The static hydraulic calibration is basically used to systematically account for any discrepancies between a known input force and the measured load cell output. There are six output load cells (reaction load cells R1-R6) which provide the thrust and moment measurements. These are located at each apex, supporting the thrust frame. In addition, there are seven calibration load cells (AY, AZ, BX, BY, BZ, CX, CZ) arranged similarly, connected to hydraulic actuators (see again Figure 2.3).

During the calibration, simulated thrust loads are applied through the hydraulic actuators. The hydraulic load (input) is measured through the calibration load cells, and the thrust stand response (output) is measured through the reaction load cells. All data is recorded and processed through the ESCORT data acquisition system. The calibration load cells are used only during calibration. During testing of a model, they are completely disconnected from the thrust frame and are not used.

A typical calibration test would involve loading and unloading each calibration cell in sequence (for example, up to 5000 lbs. in increments of 1000 lbs.) and recording the system response of each reaction load cell. The complete calibration procedure results in a total of 42 relationships between the calibration and the reaction load cells. These relationships are then linearly curve fit using the least squares method, and used to develop a six-by-six sensitivity matrix that establish a relationship between the reaction load cell output and the six components of force/moments acting at the thrust frame centroid. After the sensitivity matrix is obtained, the **inverse** is then entered into the data acquisition program to obtain the corrected thrust and moments (see Appendix C for the thrust calculation procedure). This calibration is done periodically, and documents any change in the stand. A visual inspection of the plots of the 42 relationships will show if the calibration has changed significantly. Appendix D contains a sample of these plots.

2.2.2 Pressure Tare Calibration

The pressure tare calibration is required as a result of the inlet piping

misalignment (refer again to section 2.1.2 for an explanation of the pressure tare load). These pipes should be perfectly perpendicular to the model-connection pipe, but due to the large size of the inlet piping, perfect alignment was not possible during construction of the facility. Therefore, any momentum and pressure-area terms that are imparted to the thrust balance due to misalignment are taken into account by conducting a pressure-tare calibration. To do this, the model connection pipe is blocked with a blank flange and the piping system is pressurized over a range of pressures that would normally be expected during testing (usually up to 70 psig in increments of 5 psi).

The data from each of the six system load cells is recorded by the data acquisition system and incorporated as a "tare" force to the output from the six system load cells. Each load cell is affected a little differently by the tare load, which shows different slopes on a plot of line pressure vs. load cell output. If the slope is not linear, a mechanical problem probably exists, i.e., the thrust balance may be impeded by some obstruction. The calculation procedure for the pressure tare is also included in Appendix C.

2.2.3 STA Nozzle Calibration

The purpose of the standard (STA) nozzle calibration is to validate the thrust and flow measuring systems of the PLF. The calibration provides a dynamic check of the flow coefficient ($C_{ds} = W_a/W_i$, where W_a is the actual weight flow measured at the flow measuring station and W_i is the ideal weight flow measured at the STA

nozzle) and nozzle gross thrust coefficient (C_t = measured thrust/ideal thrust). The measured loads, when used in the data reduction equations, should result in flow, force and moment values that agree with the known values.

The test nozzle is 13" in diameter, and is capable of providing 7500 lbs. of thrust at a nozzle pressure ratio of 4.0. There are four total pressure and temperature rake pads in the cylindrical section upstream of the throat. A six inch thick honeycomb flow straightener with two screen sections is built into the nozzle inlet, to ensure an evenly distributed flow pattern throughout the nozzle. A nozzle support structure is designed to support the nozzle and its thrust load in either the axial or vertical direction.

The procedure for performing a nozzle calibration is relatively straightforward. The test parameters of primary importance are the nozzle thrust, and flow coefficients. Since this is a standard nozzle, these parameters are well documented. Data is acquired over a range of nozzle pressure ratios (total pressure divided by ambient pressure). The test consists of running the nozzle at several pressure ratios, recording the data, and comparing the results with the known values. The thrust is measured at all six reaction load cells. Since the calibrated nozzle thrust is accurately predictable for any measured combustion airflow rate, the thrust stand is essentially calibrated. The results should be consistent and confirmed by the hydraulic calibration. If they are not, systematic sources of error must be identified and taken into account.

The STA standard nozzle calibration is a unique feature of the PLF. No other

thrust balance this size can be calibrated while flowing, or calibrated dynamically. Considering the size of the balance, the massive inlet piping and support structure, the accuracy is surprisingly good ($\pm 1/2\%$ including scatter plus experimental bias).

CHAPTER III

DESCRIPTION OF EXPERIMENT

3.1 Model Specifications

The ejector model is composed of an array of ten notched-cone nozzles (primary flow) placed chordwise (the x-direction in Figure 1.2(c)) along the throat of a converging/diverging nozzle shroud. Each of these primary nozzles has three spanwise (the y-direction in Figure 1.2(c)) convergent nozzle exits. For this model, the diffuser exit to throat area ratio is 1.89, and although it is similar to the E-7 ejector tested at the PLF in 1987 (Garland, 1989), the present model has a larger secondary to primary area ratio A_s/A_p of 30 compared with 23, a shorter mixing length, and a more realistic flight-type inlet. Figure 3.1 shows a close-up view of the inlet. Note the inlet door is open for vertical flight, but would close over the inlet for forward flight. This particular model was designed for a primary nozzle temperature of 1560 R and a pressure ratio of 2.7.

Also included in the research hardware is the on-balance piping and modified

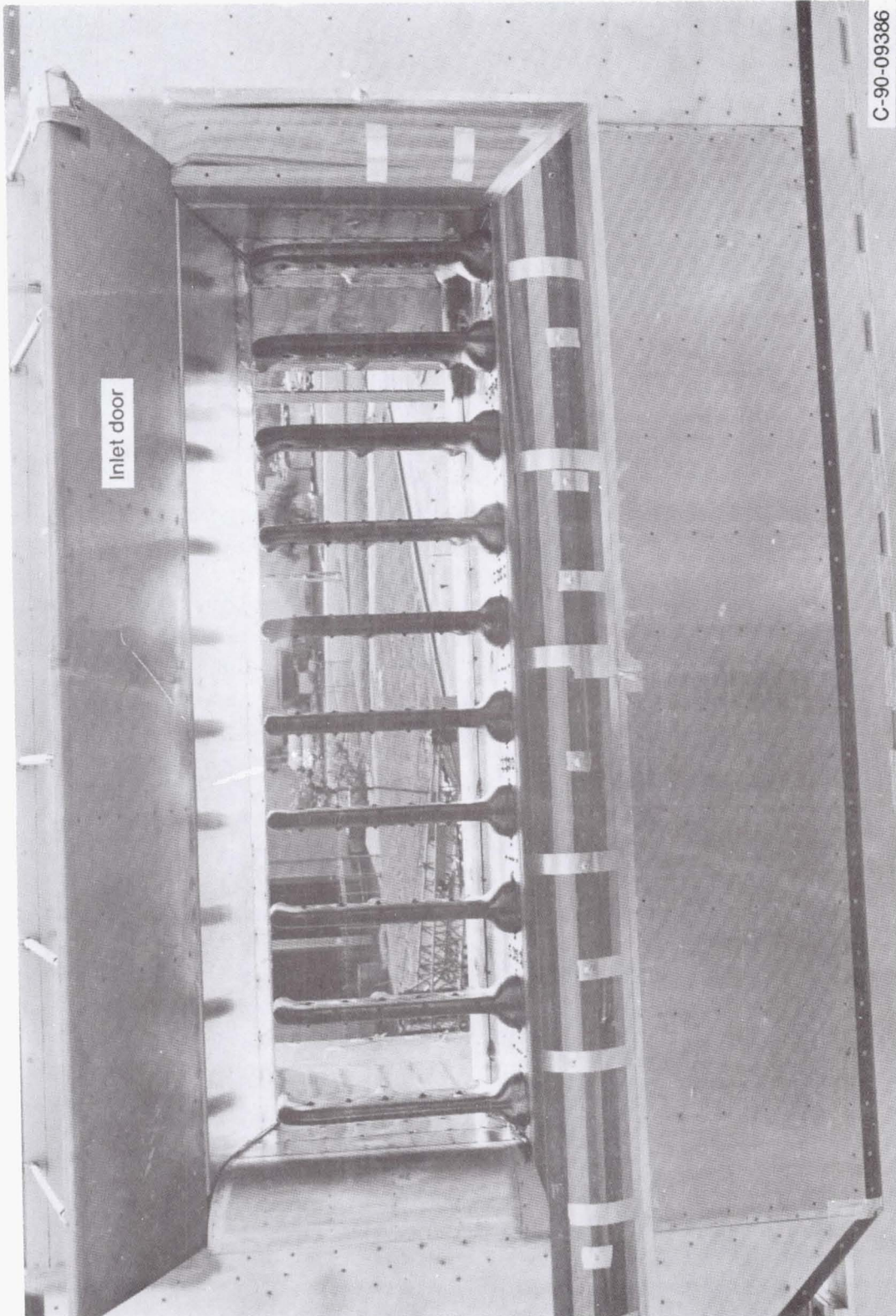


Figure 3.1.—Original ejector inlet configuration.

air combustor needed to supply and heat the air. Figure 3.2 illustrates the components of the ejector on-balance piping system. Two perforated plates acting as flow straighteners are shown at either end of the burner. The first straightens the flow from the elbow, while the second is present to help alleviate temperature distortion at the burner exit. An expandable section (bellows) is also included to allow for thermal expansion of the duct.

All hot regions of the model are fabricated in Inconel 625 except for the nozzles which are fabricated in AISI 321 stainless steel. The main structural support members are of commercial mild steel, insulated where necessary from the effects of the hot primary gas. The ejector feeder duct is wrapped in fiberglass insulation, as it would be in the aircraft. Also, any large gaps between metal pieces were sealed with high temperature putty.

3.2 Instrumentation

Several pressure and temperature measurements were taken to monitor inlet conditions and burner pressure drops (see again Figure 3.2 for locations). As shown in Figures 3.3 and 3.4, burner exit thermocouples and pressure taps are located circumferentially (the burner is expected to have inherent radial temperature distortions, the flame being naturally hotter in the center), while ejector inlet conditions are measured radially (to quantify flow uniformity).

The model itself contains approximately 130 pressure taps and 45 thermocouples

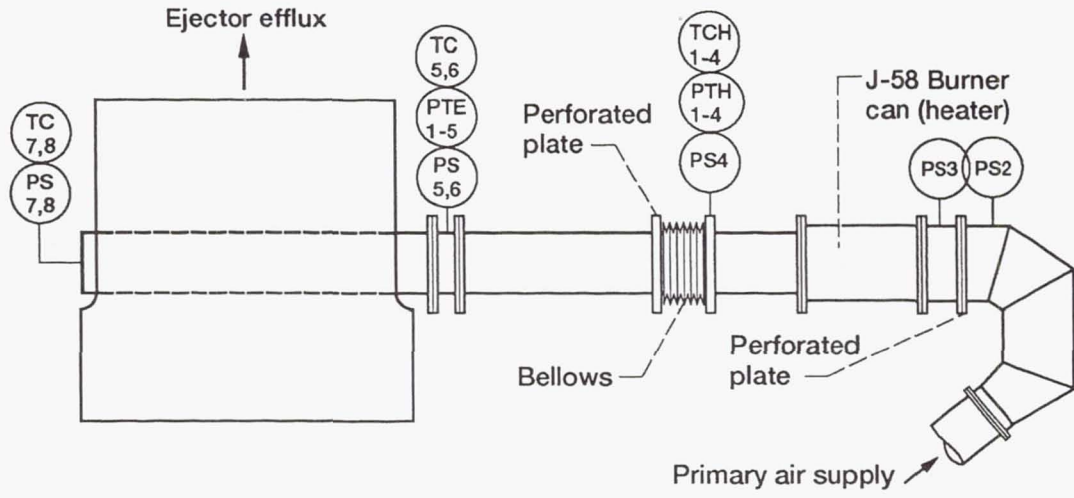


Figure 3.2.—Primary air supply duct.

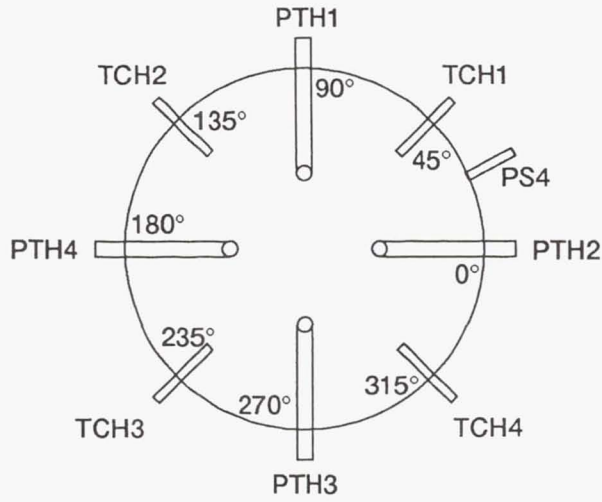


Figure 3.3.—Heater exit instrumentation ring.

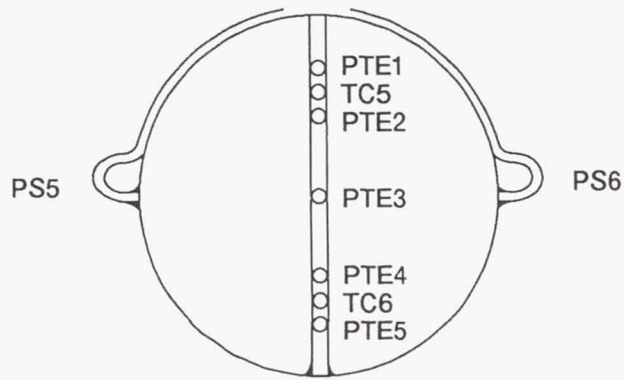
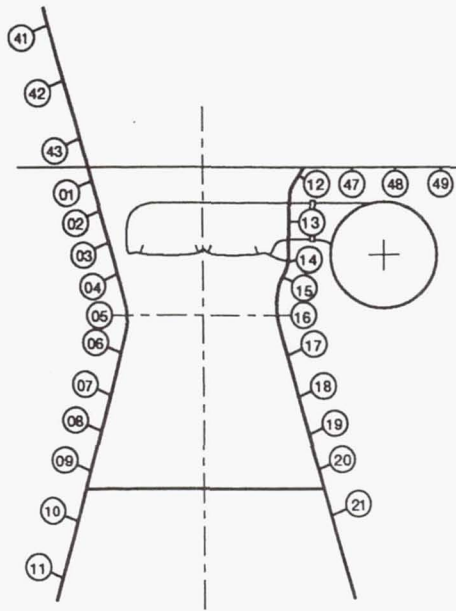


Figure 3.4.—Ejector inlet instrumentation ring.

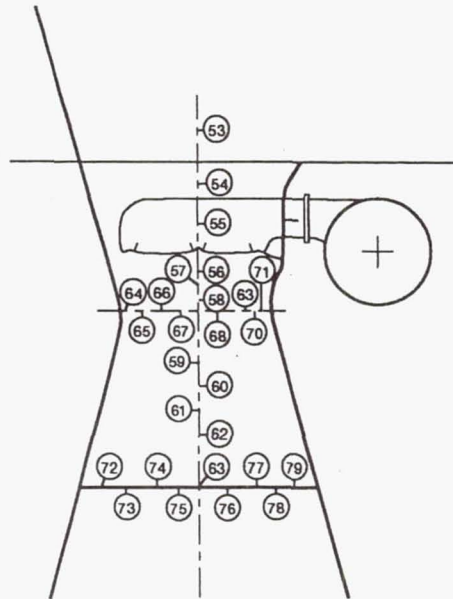
falling into four groups:

1. Ejector-surface static-pressure taps
2. Ejector-surface thermocouples
3. Ejector-exit rake instrumentation
4. Primary-nozzle static-pressure taps

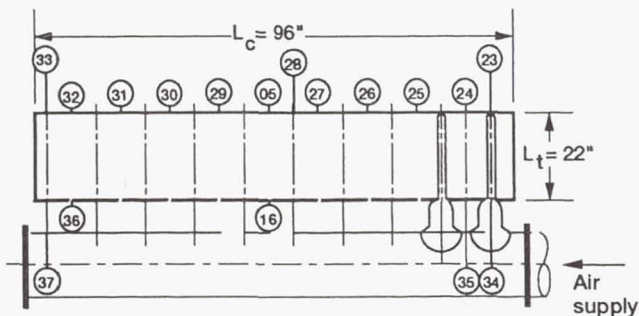
To provide information on loading and pressure distribution, static taps are located on the ejector wall between primary nozzles #5 and #6 (Figure 3.5(a)). According to design, on both sides of the ejector shroud two pressure taps are located above the nozzle exit plane, one at the nozzle exit plane, one at the plane of impingement of the plume on the wall, one at the throat and several below the throat and on to the diffuser exit doors. There are also nine static taps on the inlet door, and nine on the upper body surface. Static taps are also located on the upstream end-plate (Figure 3.5(b)). Four more taps similar to taps 53-56 are located on the downstream end-plate. Ejector-throat static taps (Figure 3.5(c)) are present to confirm chordwise uniformity of the throat Mach number. For thermal/structural design purposes, thermocouples (Figure 3.5(d)) are located along both the ejector wall (one row containing 18 thermocouples between nozzles #3 and #4 and a similar row in line with nozzle #4) and along the center line of the upstream end-plate. All thermocouples are heavily insulated on the outside model surface to prevent heat loss to the ambient. This procedure helps insure accurate temperature measurements. As shown in Figure 3.6, a rake containing twenty total pressure tubes, nine static pressure tubes, and ten thermocouples (alternating P_T , T_T , P_T , P_S)



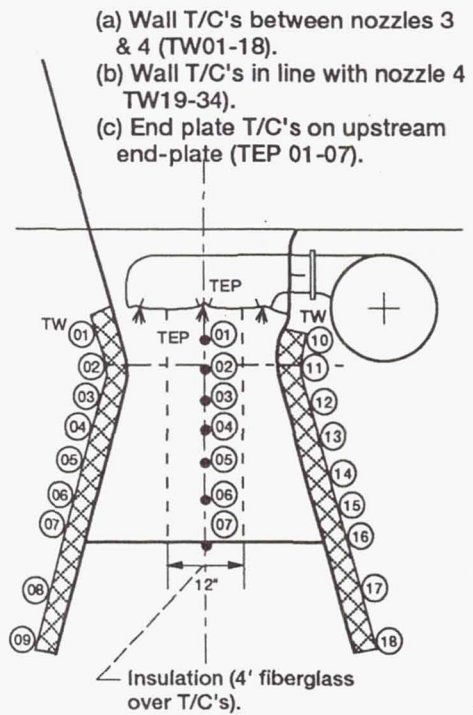
(a) Wall static pressure taps.



(b) Upstream end-plate static pressure taps.



(c) Throat static pressure taps.



(d) Wall and upstream end-plate thermocouples.

Figure 3.5.—Ejector instrumentation.

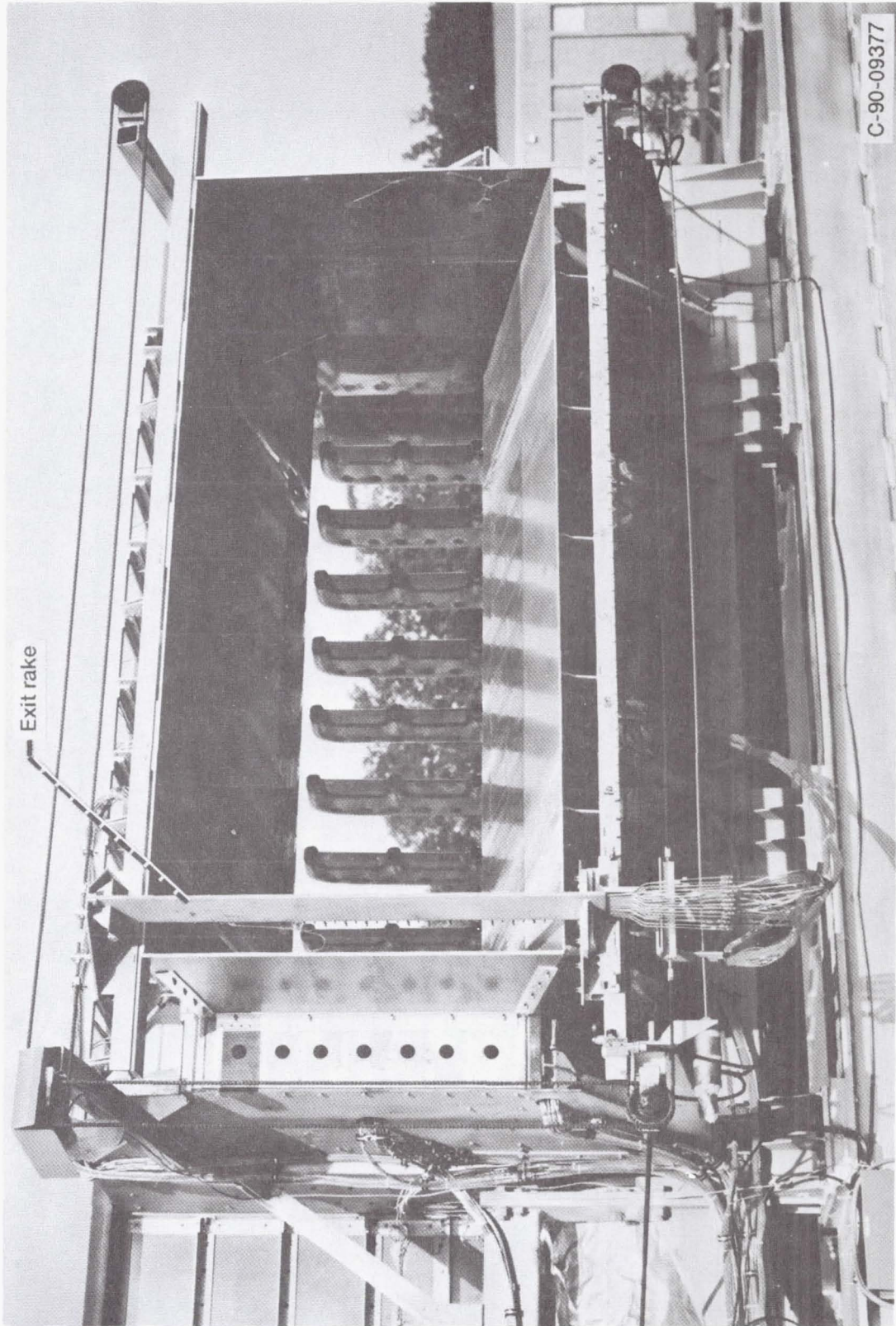


Figure 3.6.—Ejector exit plane.

is placed spanwise across the ejector exit. To obtain measurements in the diffuser exit plane, the rake is incrementally moved through the 96 inch chord length (left to right in Figure 3.6), while a (previously calibrated) transducer reports the probe position. Also, each nozzle has an internal reference static pressure tap previously calibrated against average nozzle exit total pressure and effective nozzle area for calculation of the isentropic primary thrust.

3.3 Testing Procedure

Steady-state performance testing consisted of static and total pressures, temperature, and thrust measurements over a nozzle pressure ratio (NPR) range of 1.6 to 3.0. These pressure runs were conducted with primary flow temperatures of 1560 R, 1360 R, 1160 R, and a cold flow of approximately 530 R (temperature of facility air supply without the burner ignited). For the hot temperatures, the steady state max-to-min temperature variation was approximately ± 20 R based on the burner system capability. The cold flow primary temperature did not vary as much during each test run; however, since the PLF is an outside facility (refer to section 2.2), primary and secondary air temperatures are lower for the tests conducted in the winter months than in the summer.

To help analyze the diffuser flow, rake surveys were conducted at NPR = 2.7 for the different temperatures. This procedure required incremental movement of the exit rake (as previously described) to obtain diffuser exit plane pressure and

temperature measurements approximately every four inches. To investigate the flow near the diffuser wall, data was obtained every one or two inches in the vicinity of the wall.

Potential influences on the data collection were the fluctuations in both wind speed and direction. These fluctuations often caused unsteady and non-uniform inlet flow. For this reason, no single test point is exactly repeatable. However, data for each point was collected over approximately 10 seconds to obtain a reasonable average. All calculations use the averages as the actual data point value.

3.4 Cold Flow Tests

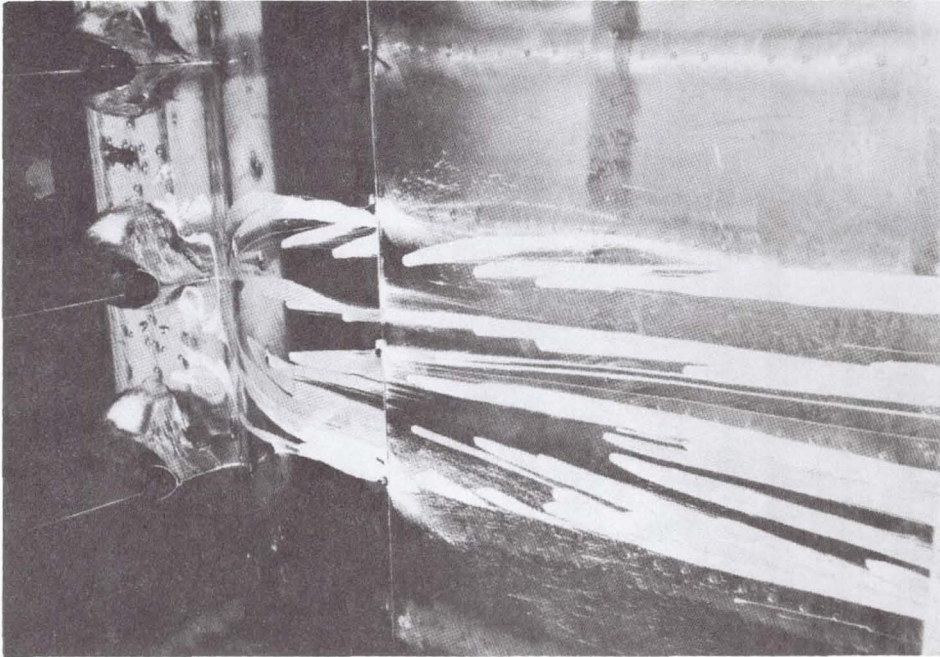
3.4.1 Flow Visualization

Several flow visualization techniques were used to assess the inlet flow field condition and pinpoint problem flow areas. For instance, yarn tufts and paint dots placed on the inlet surface and nozzles indicated inlet door separation and recirculation at the nozzle roots. The yarn tufts were easy to use, inexpensive, and provided a preliminary identification of the flow problems at the inlet. One particular advantage with the tufts was that performance data could be gathered while concurrently observing the tuft motion on the video camera. It is assumed that the tufts themselves did not interfere with the flow. Indications of recirculation and otherwise "bad" flow effects were denoted by tufts that "stood on end", or were wildly flipping around.

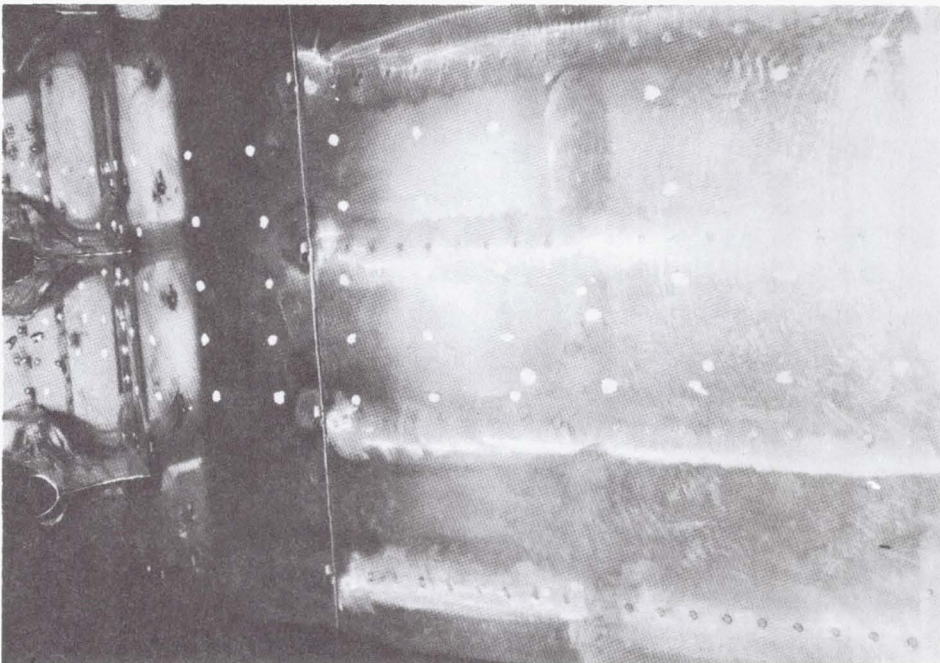
The paint dots are actually a mixture of white artist's paint and "Marvel Mystery Oil" applied in a grid-like fashion to the ejector surface several hours before testing (Figure 3.7(a)). The paint is not allowed to dry, but rather the facility is brought to the appropriate test condition for a few seconds, and then shut down for examination. The paint will smear as in Figure 3.7(b), providing some indication of the surface airflow patterns. The trick is obtaining the proper paint consistency and grid density so that the paint will run, but doesn't smear together incomprehensibly. Too much airflow will also ruin the patterns. This is also an inexpensive and easy to use method of flow visualization. Although this is still only a qualitative test, a greater understanding of the flow can be obtained than with just the yarn tufts.

The last flow visualization method employed was smoke generation around the model. The use of smoke generators confirmed separation off the upstream inlet radius, as the smoke entrainment into the secondary stream bypassed the first nozzle (not enough flow near the wall). This was also shown by the lack of dead bugs brought in by the secondary air on the leading edge of primary nozzle closest to the combustor.

More sophisticated methods of flow visualization such as Laser Doppler Velocimetry (LDV) and sheet lasers were not used. Again, safety issues did not allow the use of these devices because the PLF is not grounded. In addition, there would be the possibility of a stray laser beam accidentally hitting someone or something. These are also much more expensive devices to operate.



(b) After test condition.



(a) Before testing.

Figure 3.7.—Flow visualization paint dots.

3.4.2 Configuration Changes For Performance Optimization

Throughout the test program, model modifications were made to optimize ejector performance. These configuration changes are summarized below, and can be compared with the original configuration previously shown in Figure 3.1.

- a. Inlet door radius (Figure 3.8): The first configuration change involved replacing the inlet door (sharp edge) with a curved leading edge to decrease the inlet separation shown by the yarn tufts. This structure had a radius of 6.375", and was constructed from a PVC pipe.
- b. Nozzle root fairings (Figure 3.9): Aluminum fairings were installed at the primary nozzle roots downstream of the nozzles to reduce the "bluff body" separation indicated with the paint dots. The fairings were tack-welded into place and then sealed with high temperature putty.
- c. End plate spacer (Figure 3.10): Since the ejector is designed for a hot primary temperature of 1560 R, thermal expansion of the ejector plenum was expected to cause some degradation of performance for the cold flow tests. As shown in Figure 3.10, the ejector primary nozzle plenum is attached to the ejector shroud between the second and third nozzle (plenum anchor plane). Upon heating, plenum expansion to the right of the anchor point is adjusted for in the upstream bellows, while free expansion occurs to the left. At a primary flow temperature of 1560 R the nozzles are in their design locations. Any decrease in ejector primary temperature results in a slightly shorter plenum, causing the primary jet flow to shift away from

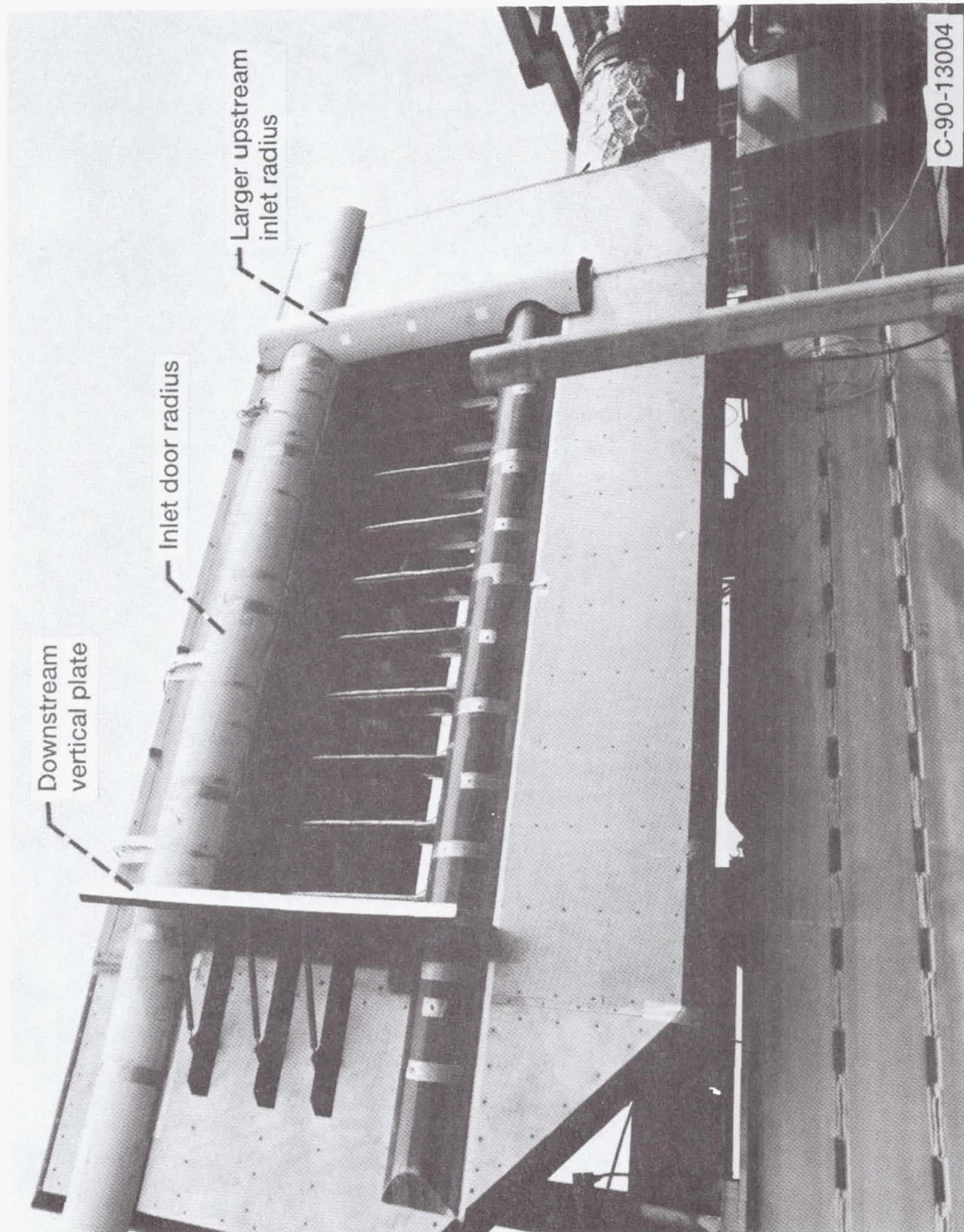


Figure 3.8.—Photo of ejector plan view. Inlet door replaced with radius shown.

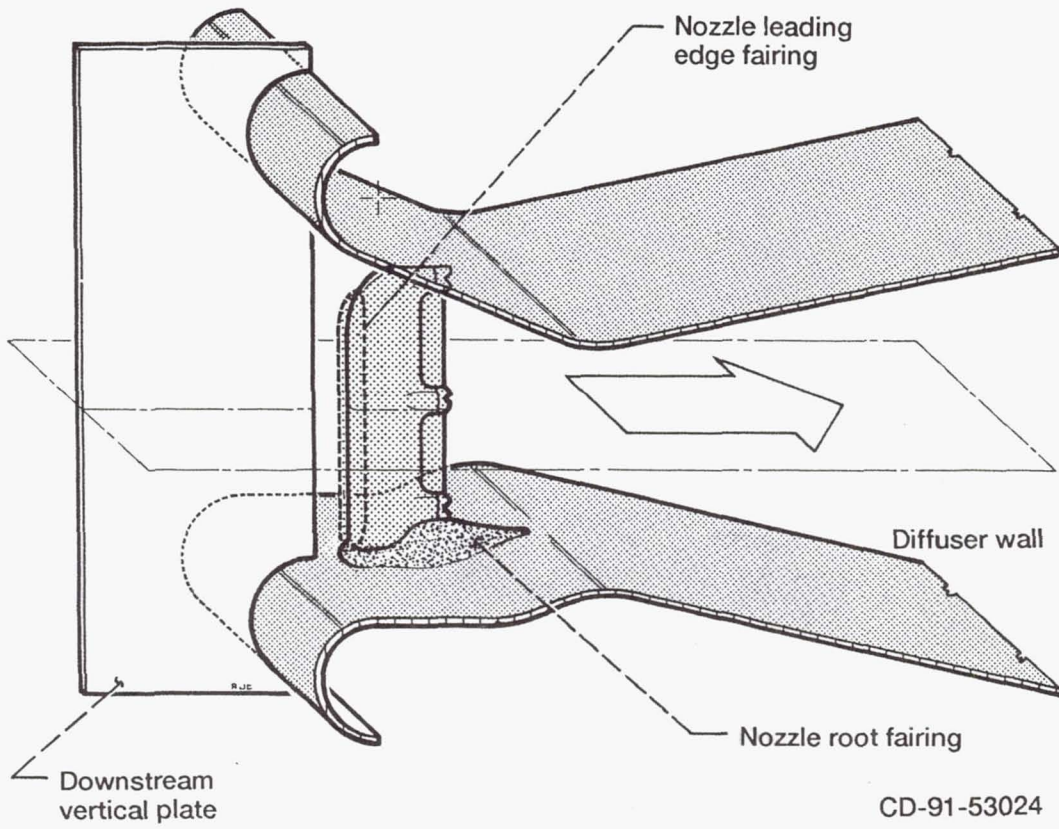


Figure 3.9.—Cross-sectional view of ejector.

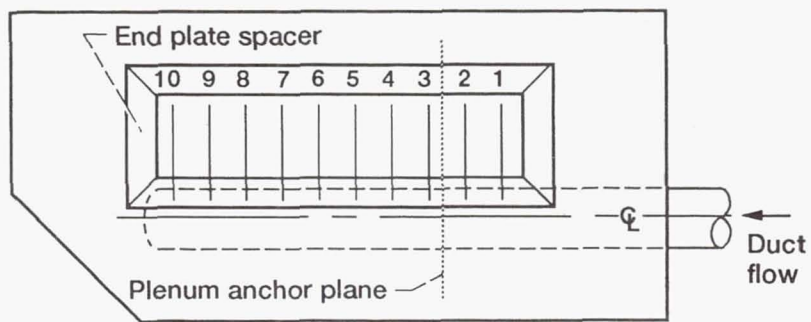


Figure 3.10.—Sketch of ejector plan view.

the wall and decrease local thrust augmentation. To alleviate the expansion gap in the cold flow configuration, a 1/4" thick plywood spacer was installed flush with downstream end plate.

- d. Notched primary nozzles: The inside nozzle corners were cut on the upper and lower nozzles (0.125" on all nozzles, but 0.2" on #4, #5 & #6) in order to redirect the primary flow of the outside plumes away from the diffuser wall and increase flow mixing in the spanwise direction.
- e. Downstream vertical plate (Figures 3.8 and 3.9): A plywood vertical plate was installed at the downstream end plate in order to examine the crossflow effects caused by the wind.
- f. Larger upstream end radius (Figure 3.8): The 5.0" upstream wooden radius was replaced by a section of PVC pipe having a 6.375" radius, to correct for flow separation.
- g. Nozzle leading edge fairings (Figure 3.9): Aluminum fairings were constructed for the first three nozzles, and held in place with aluminum tape. Since the flow was separating off of the smaller upstream radius, these fairings were intended to direct the flow back toward the upstream end-plate to more evenly distribute the inlet flow.

3.5 Hot Flow Tests

Once the ejector performance was examined with cold primary flow, primary nozzle temperature effects were then explored. Unlike the cold flow tests, only one configuration was tested with the hot primary flows. Although this configuration does not incorporate any of the end effect "fixes", it does correspond with the cold flow configuration that had the best overall performance. Major features of this configuration include replacing the inlet door with a leading edge radius, installation of the nozzle root fairings, and notching of the primary nozzles. The downstream end plate spacer was removed, since expansion of the nozzles and plenum occurs with the high primary temperatures.

CHAPTER IV

RESULTS AND DISCUSSION

4.1 Thrust Augmentation Ratio

In this discussion, ejector performance is measured by the thrust augmentation ratio:

$$\phi = \frac{\text{total thrust}}{\text{primary-nozzle ideal thrust}} = \frac{\text{load cell measurement}}{\text{isentropic thrust}} \quad (2)$$

where isentropic thrust is computed from the internal nozzle static pressure taps and the supply pipe mass flow rate. During the rake surveys a second thrust parameter is defined as:

$$\phi_R = \frac{\text{rake thrust per inch}}{\text{isentropic thrust per inch}} \quad (3)$$

This represents the total rake augmentation at each chordwise rake location. In this case, rake thrust is computed from the rake total-to-static pressure ratio.

4.1.1 Cold Flow Tests

As shown in Figure 4.1, control volume analysis (based on previous E-7 test data) predicts a cold flow augmentation ratio of 1.7 at a nozzle pressure ratio (NPR) of 2.7. The present series of tests showed lower augmentation ratios than expected (from the control volume predictions). To investigate possible causes, an analysis of the flow field was conducted using both flow visualization and rake surveys.

As previously discussed, flow visualization techniques indicated separation off the inlet door and upstream inlet radius, as well as recirculation at the nozzle roots. Configuration changes were then made to reduce (or eliminate) these effects. Performance curves (Figure 4.2) for the configuration changes show a gradual, but significant (4.5%) increase in the augmentation ratio. Note: both primary and secondary temperature measurements vary approximately 1.5% (6 R) throughout the configuration changes. This variation is caused by the changing day to day weather conditions. Variation during the test runs will be explained at the end of the section.

The first configuration change involved replacing the inlet door with a leading edge radius, decreasing the inlet separation such that the change in thrust augmentation ($\Delta\phi$) was nominally +0.022. Next, fairings were installed at the primary nozzle roots to streamline the flow and reduce the nozzle "bluff body" separation. Figure 4.2 shows that this modification has a greater effect at lower NPRs. An explanation is given below.

In theory, separation occurs in a region of adverse pressure gradients. At a higher NPR the secondary flow accelerates faster around the primary nozzle, creating

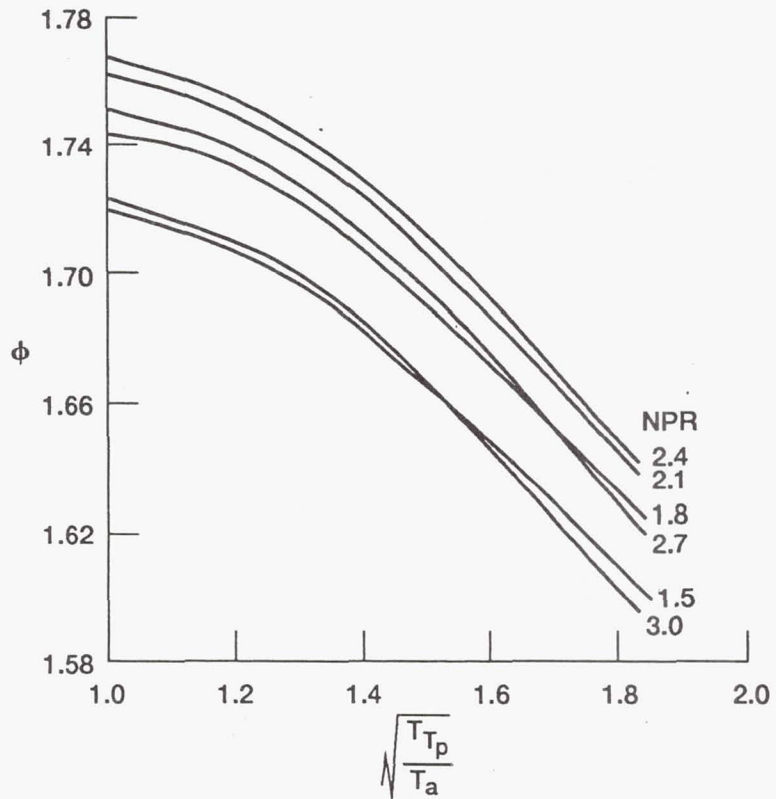


Figure 4.1.—Test adjusted ejector performance prediction.

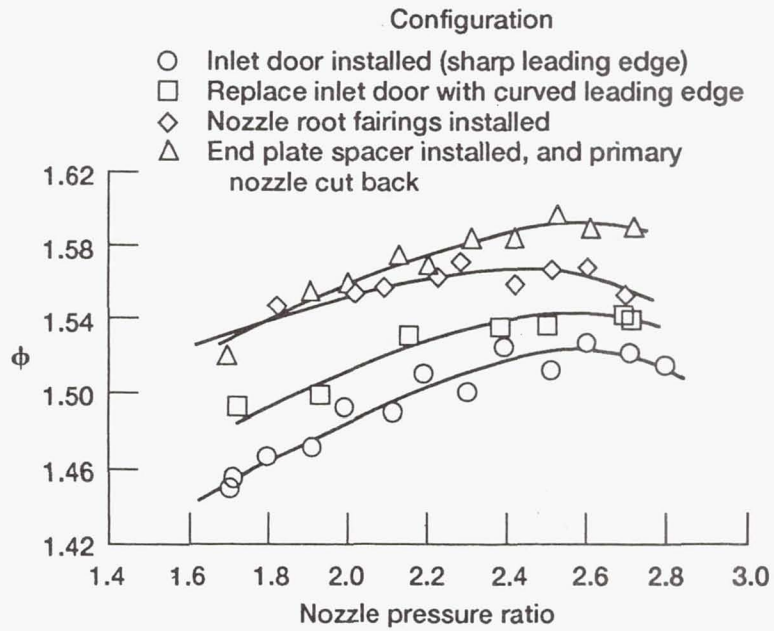


Figure 4.2.—Cold flow ejector performance.

a more favorable pressure gradient (lower pressure) and a delay in separation. Therefore, the addition of the fairings have less of an effect at high NPR because the flow initially separates farther downstream. These fairings also physically reduce the lower pressure region where recirculation occurs. The fourth curve shown will be discussed momentarily.

The rake surveys were used to map pressure and temperature data for the ejector exit plane. Chordwise rake analysis of the exit flow, using the average spanwise augmentation (Figure 4.3), indicated separation off the upstream inlet radius and downstream end-plate. Poor chordwise mixing is evident through the nozzle peaks and valleys in the rake augmentation profiles. The spanwise pressure distribution at each chordwise location (Figure 4.4, showing one chord location), indicated poor spanwise mixing (large pressure peaks), and a strong attachment of the primary nozzle flow to the diffuser walls.

The addition of a plywood spacer not only increased augmentation levels on the downstream end-plate (compare Figure 4.3 to Figure 4.5(a)), but also the overall augmentation ($\Delta\phi = +0.03$ from the root fairings curve in Figure 4.2). It should be noted that this curve does not appear in Figure 4.2.

Since the primary nozzle flow was attaching to the diffuser walls, the primary-nozzle exit area was increased slightly. Nozzle corners were cut to redirect the primary flow of the outside plumes away from the diffuser walls and increase flow mixing in the spanwise direction. Augmentation ratio ϕ_R , as measured by the ejector-exit rake before the nozzles were cut, is shown in Figure 4.5(a); after they were cut

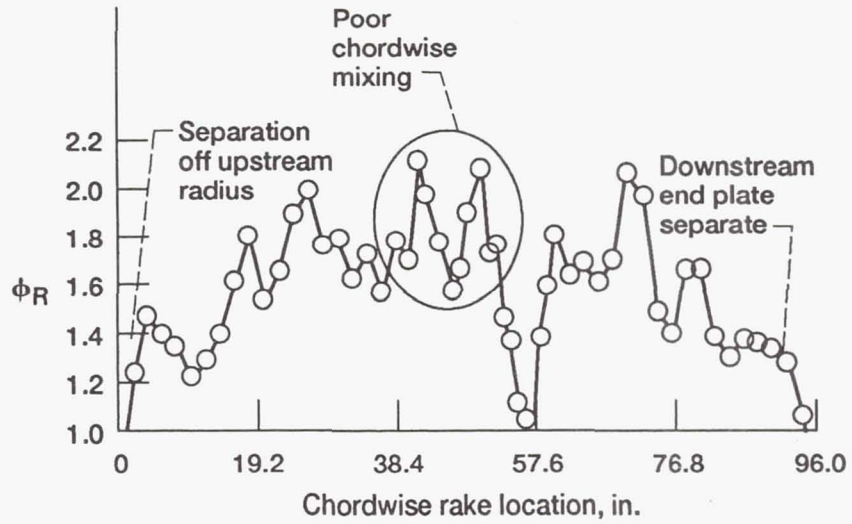


Figure 4.3.—Cold flow ejector performance at NPR = 2.7—inlet door radius and nozzle root fairings installed.

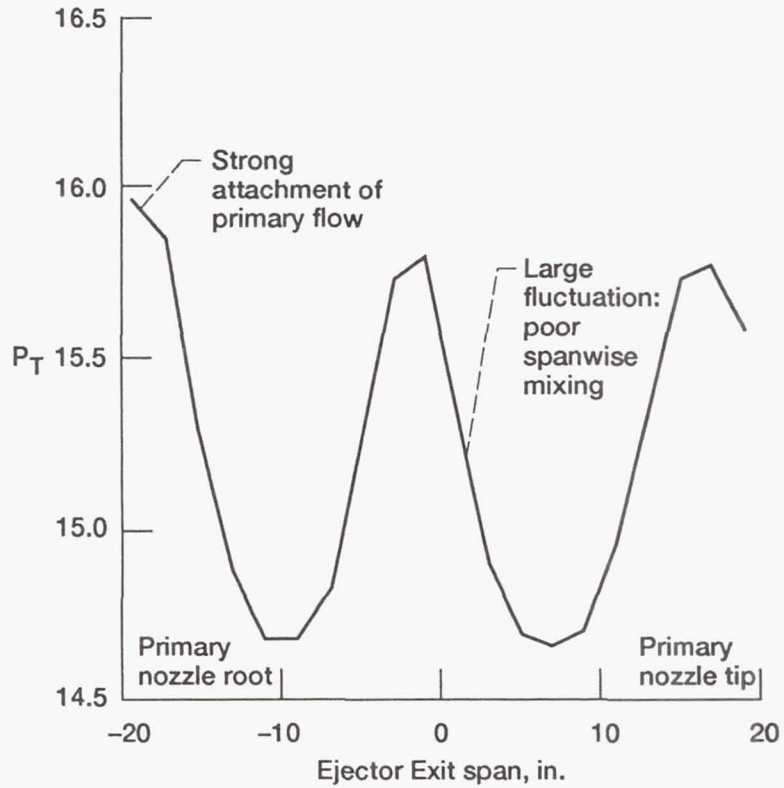
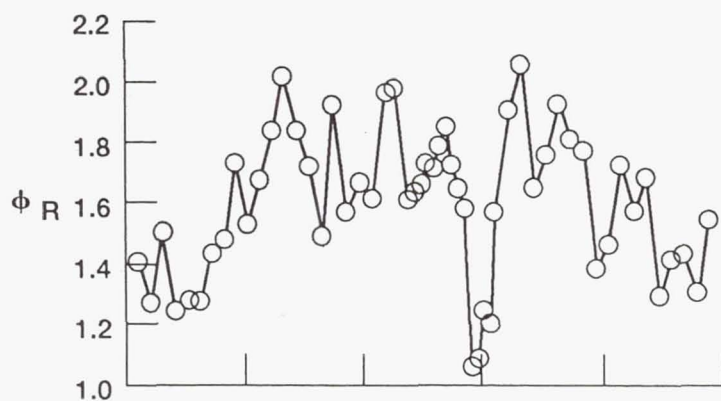
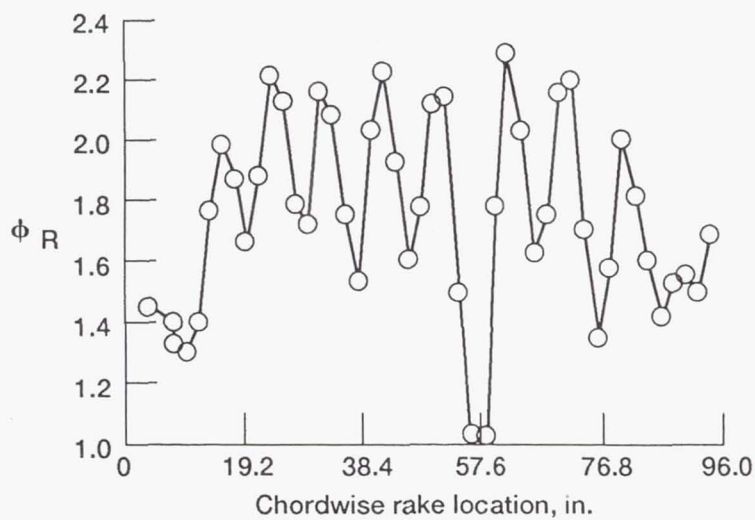


Figure 4.4.—Cold flow spanwise pressure distribution: NPR = 2.7, $T_p = 517$ R, chord location = 40 in.



(a) Before primary nozzles cut back. Inlet door curved leading edge, nozzle root fairings and wood end plate installed.



(b) After primary nozzles cut back. Chordwise rake location, in.

Figure 4.5.—Cold flow primary nozzle adjustment: NPR = 2.7.

in Figure 4.5(b). By comparing the two one can see an increase in chordwise performance, however the large fluctuations in ejector-rake augmentation indicate low chordwise mixing. Again, a small increase in the overall thrust augmentation was noted at the design point (Figure 4.2). Note that the sudden decrease in rake augmentation between nozzles 6 and 7 is always present. The exact cause of this decrease is not known, but it is consistent throughout the entire test. One possible cause could be a slight misalignment of one of these nozzles; however, no testing was performed to investigate this phenomena.

Some configurations were not designed to increase the overall ejector performance, rather, only the end-wall augmentation. Effects of these end plate adjustments were examined through the exit rake augmentation distributions of Figure 4.5. Comparing the "before and after" plots (Figures 4.5(b) and 4.6), all end adjustments do exhibit increased rake augmentation. At the upstream end-plate the larger end radius performed much better than the leading edge fairings (rake augmentation increases 18.8% vs 7.6% at nozzle #1), although no attempt was made to optimize the angle of the fairings. Although the nozzle leading edge fairings may have improved the local augmentation at the upstream end plate, the overall augmentation was not improved. Rather, it decreased and was somewhat random. Perhaps the fairings were creating significant amounts of drag. Again, optimization of the fairing placement angle may have helped. At the downstream end-plate, even though the vertical plate provides a 6.1% increase in rake augmentation, by decreasing the mixing from nozzles #6-#9 it introduces more problems than the

separation.

The highest cold flow augmentation ratio was obtained when incorporating configuration changes (a) through (d), as denoted in section 3.4.2. This data is shown in Figure 4.7. The two curves reflect the effect of seasonal temperature variation on cold flow performance (approximately 2%) where:

	January	August
T_a	480 R	535 R
T_p	510 R	540 R

Table I Seasonal variations in temperatures

Again note that these are the *average* temperatures for each run. The actual primary nozzle temperature increased gradually throughout each run, due to the heat transfer of the supply air. The following is a brief explanation. Compressed air was supplied to the primary nozzles at a temperature higher than ambient, traveling and heating the long length of supply pipe. As the pipe heats up, the air loses less heat and therefore the air temperature at the model inlet increases. In these tests, the air temperature simply did not have enough time to reach equilibrium. In Figure 4.7, the difference in thrust augmentation levels between the two curves is caused by the

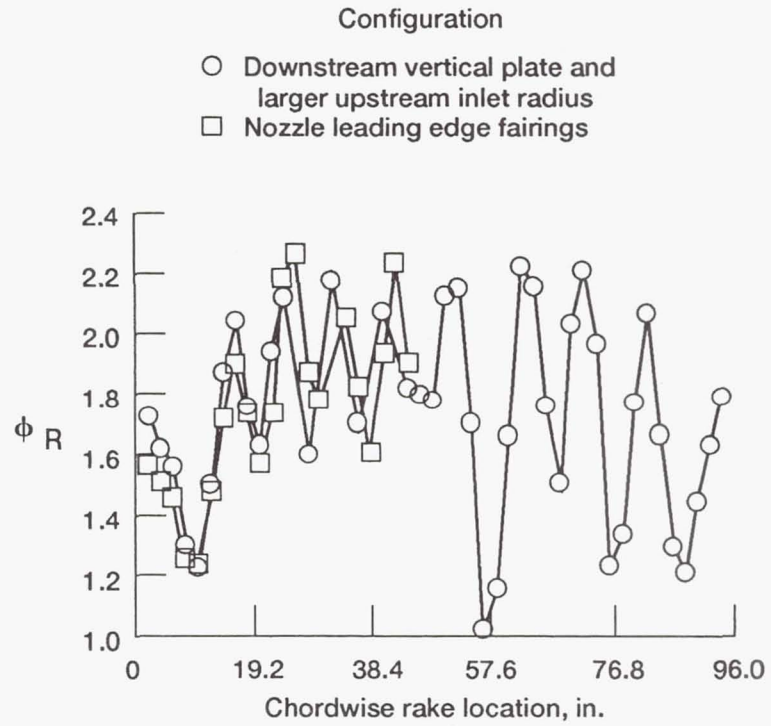


Figure 4.6.—Cold flow end plate inlet adjustments: NPR = 2.7.

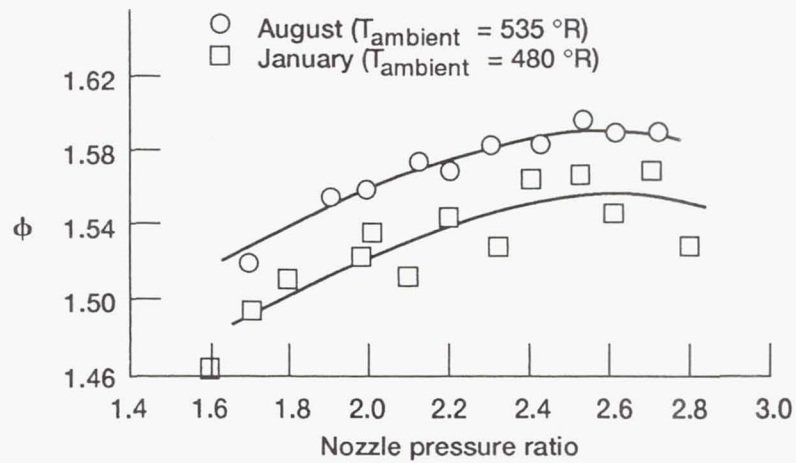


Figure 4.7.—Effect of seasonal temperature variation on cold flow performance.

different ambient temperatures, but the greater scatter in the January data probably results from the larger variation in primary nozzle temperature ($\Delta T_p = 15$ R in January, 5 R in August).

4.1.2 Hot Flow Tests

Performance vs. nozzle pressure ratio curves for several different primary nozzle temperatures at "constant" ambient temperature (Figure 4.8) show a thrust augmentation loss as the primary nozzle temperature increases. Significant scatter is present in the hot flow augmentation curves, due to the ± 20 R inlet temperature deviations (burner adjustment error) as described in section 3.3.

One way to avoid this experimental error is to plot the thrust augmentation ratio vs. the primary nozzle temperature (Figure 4.9). A similar decrease in thrust augmentation can be seen when keeping the nozzle pressure ratio constant at 2.7 and varying the primary nozzle temperature. Experimental scatter between the data points is greatly reduced. The reason for this is that nozzle pressure ratio, which is indicative of air-supply pressure, can be controlled with more accuracy than primary-flow temperature, which is dependent on maintaining a constant burner fuel flow.

Although it is the preference to present thrust augmentation ratio (as opposed to absolute thrust results), some explanation is necessary to assure that the use of ϕ trends (as a function of NPR) are meaningful. As NPR changes so does the isentropic nozzle thrust (which is the denominator of the augmentation ratio); changes in absolute thrust level (relating to vertical lift capability) can not be

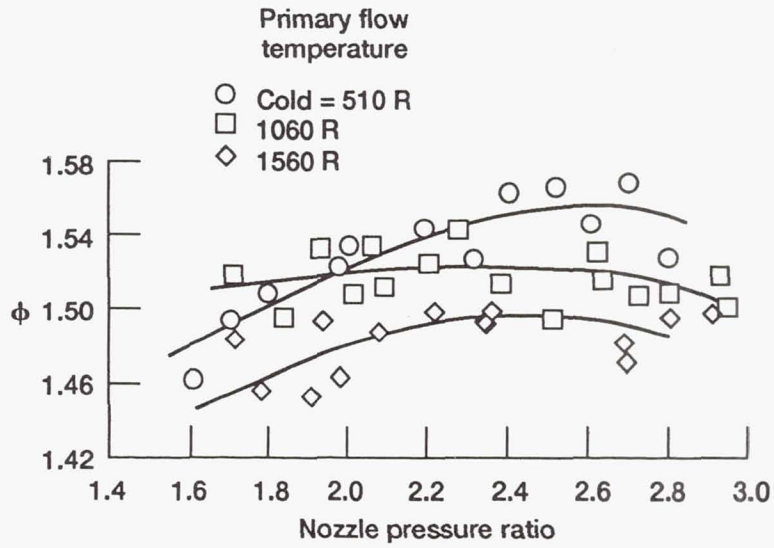


Figure 4.8.—Hot flow ejector performance.

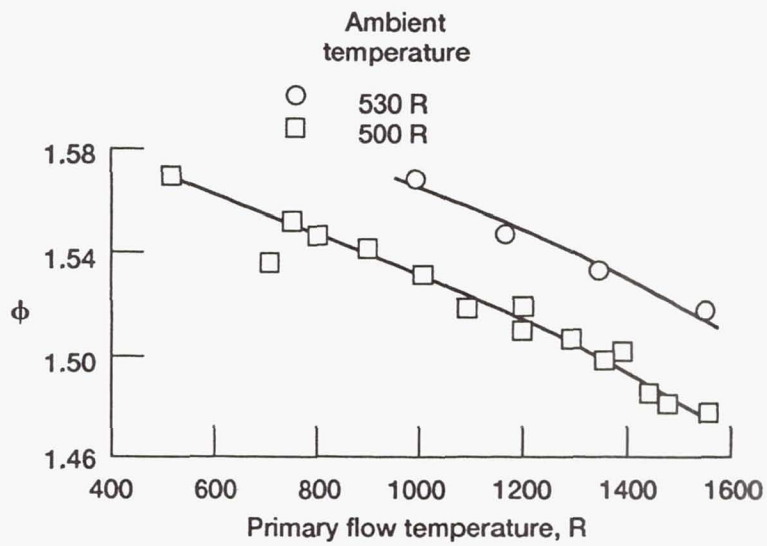


Figure 4.9.—Ejector performance at NPR = 2.7.

deduced from ϕ alone. However, at constant NPR isentropic thrust is constant, and changes in total thrust can be assumed from changes in the augmentation ratio. Since a discussion on the change in thrust augmentation ratio only makes reasonable sense for constant NPR, Figure 4.9 can also be viewed as showing the changes in actual thrust (temperature changes and mass flow changes negate each other -- isentropic thrust is constant). The data in Figure 4.9 reflects the imperfections of theoretical analysis; nozzle pressure ratio contains a 1% variation (unsteady air supply), which in turn results in a 2% variation in isentropic thrust. Accuracy of the presented data should be interpreted accordingly.

In Figure 4.9 data is presented for both ambient temperature levels as described in the cold flow section, and indicates that the hot flow performance is similarly affected by ambient temperature differences. The augmentation levels of the two ambient temperatures differ by approximately 2.5%. It is interesting to note that similar amounts of reduction in the augmentation ratio can take place by (1) decreasing the secondary flow temperature by about 30 R, or (2) increasing the primary nozzle temperature by about 500 R.

The design point chordwise rake performance (Figure 4.10) shows better mixing than the cold flow rake performance (Figure 4.5(b)). Although the rake augmentation profiles still show incomplete mixing, the flow is fairly uniform across the chord. The downstream end-wall peak augmentation is now more consistent with center flow; an increase occurring with plenum expansion to a level consistent with the corrected cold flow. However, since this configuration does not reflect the

upstream end changes, some lower augmentation in the vicinity of nozzle #1 can be seen. Still present is the low spot between nozzles #6 & #7, indicating that the effect is not one of temperature but of nozzle manufacture or installation. The ultimate goal in thrust augmenting ejector design is to obtain the highest augmentation ratio possible. Keeping with this philosophy, removal of the boundary layer/end effects raises the integrated augmentation from 1.47 (as shown in Figure 4.9) to an augmentation ratio of 1.70.

4.2 Surface Static Pressures

Surface static pressures (Figure 3.5) provide information on component loads while showing the degree of secondary flow uniformity along the chordwise length of the ejector. Location of the surface static pressures was described previously in section 3.2. Typical surface static pressure data are shown in Figure 4.11 for the ejector design point conditions of $T_p = 1560$ R, and $NPR = 2.7$. For this condition the ambient pressure is 14.45 psia and the static pressure taps located as shown previously in Figure 3.5(a). Notice that the entire ejector duct operates in sub-ambient conditions, with pressure expanding to ambient at the diffuser exit (left side of Figure 4.11). The lower pressure on the fuselage side of the intake is probably due to flow separation and/or recirculation around the primary nozzles, as well as the different inlet geometric contours. The low inlet point on the wing side is most likely just a bad static pressure tube (since it is reading low, it is either leaky or

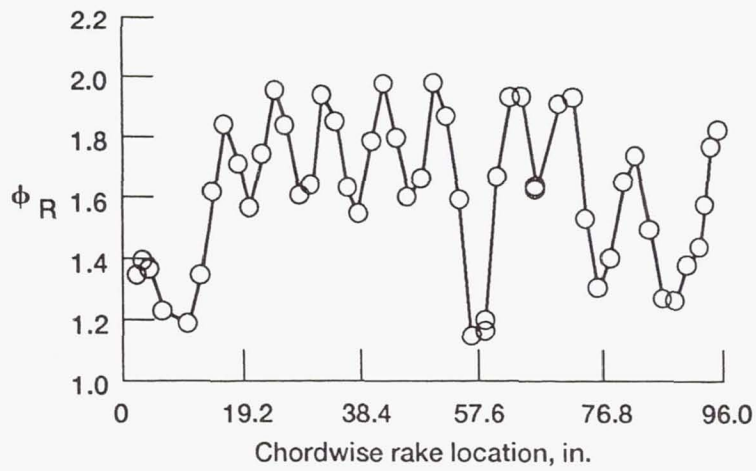


Figure 4.10.—Design point ejector performance: NPR = 2.7,
 $T_p = 1560$ R.

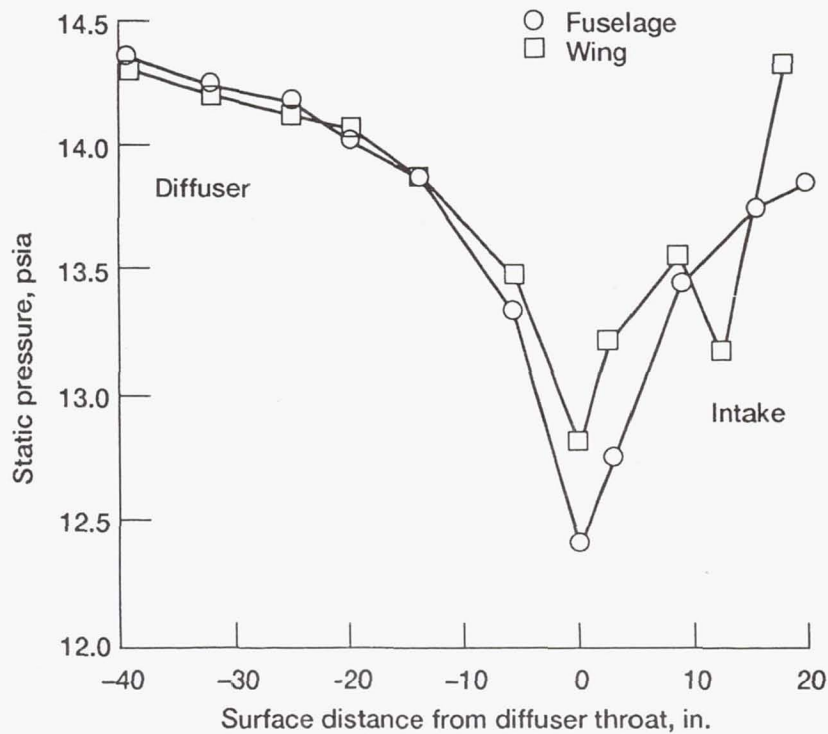


Figure 4.11.—Surface static pressure distributions: NPR = 2.7,
 $T_p = 1560$ R.

defective).

Integrating these pressures in both the horizontal and vertical directions yields the ejector surface pressure forces. A sample set of points integrated from Figure 4.11 is shown in Table II.

Plots of both the horizontal and vertical pressure loads vs. nozzle pressure ratio in Figures 4.12 and 4.13 show that these forces are proportional to NPR. The abbreviations used in these plots correspond to Table II. For example: the horizontal inlet load on the fuselage side is abbreviated as LFIH.

The variation of throat surface Mach number with NPR is shown in Figure 4.14 for both the fuselage and wing sides at a primary nozzle temperature of 1560 R. The fuselage side value is a little higher due to the inlet geometric differences (higher inlet curvature) and lack of nozzle interference. The throat surface Mach numbers

		VERTICAL	HORIZONTAL
FUSELAGE	INLET	11.855	-21.135
	DIFFUSER	-4.180	-26.080
WING	INLET	8.168	18.386
	DIFFUSER	-3.957	23.783

Table II Pressure forces (lb_f/in. at NPR=2.7, T_p=1560 R)

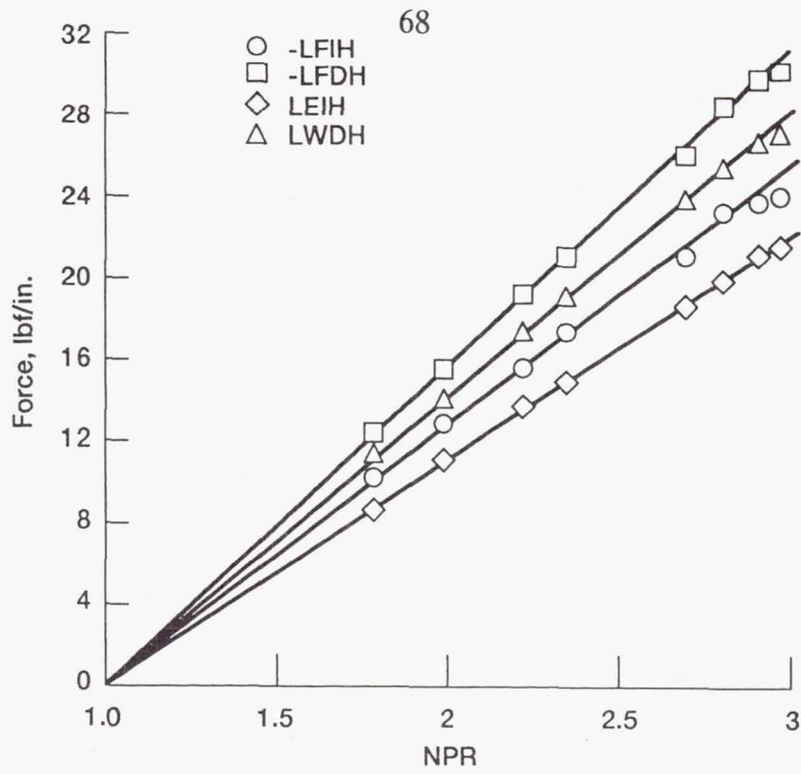


Figure 4.12.—Horizontal pressure loads: $T_p = 1560$ R.

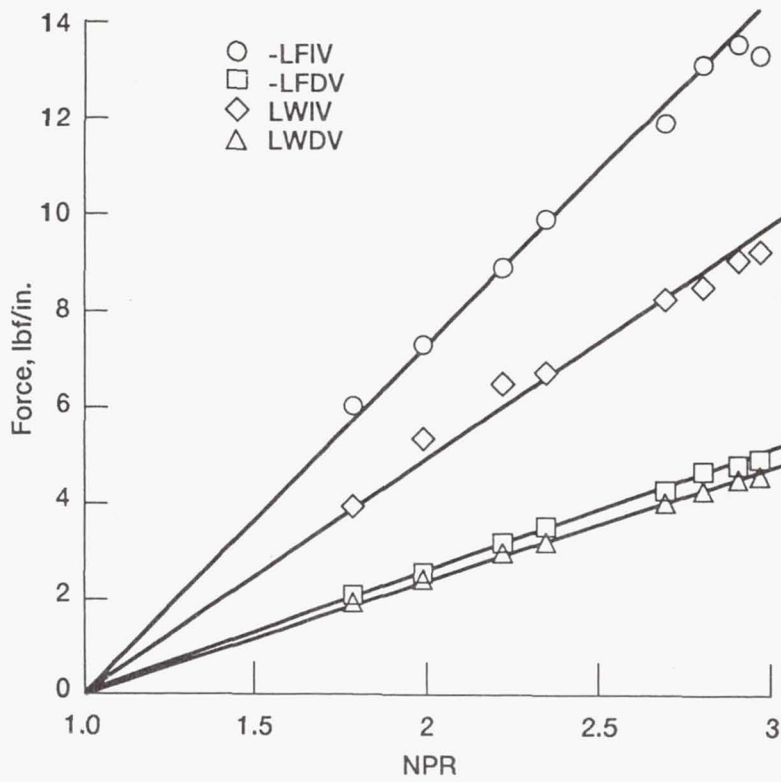


Figure 4.13.—Vertical pressure loads: $T_p = 1560$ R.

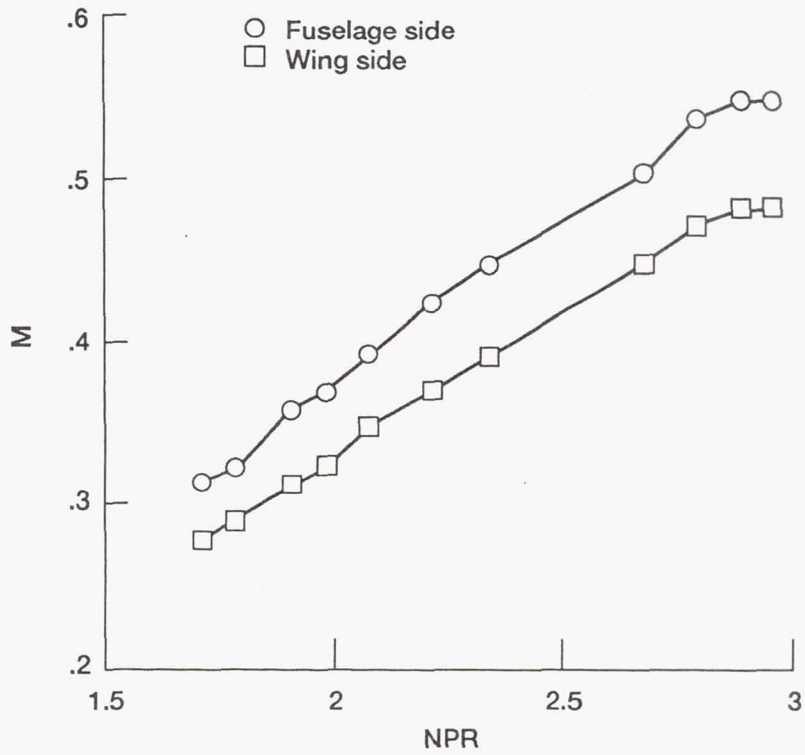


Figure 4.14.—Effect of nozzle pressure ratio on throat Mach number: $T_p = 1560$ R.

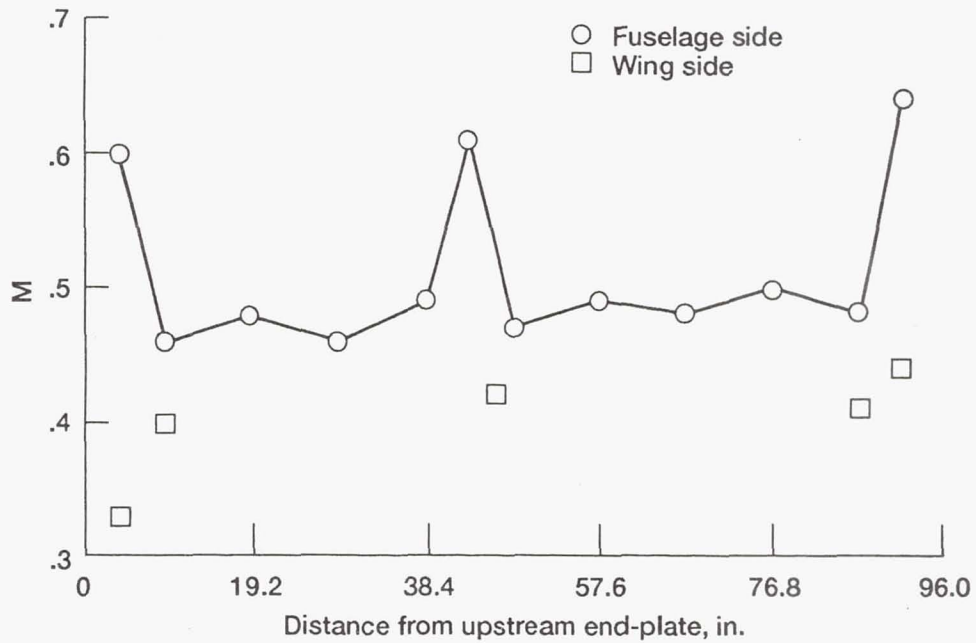


Figure 4.15.—Chordwise variation of throat Mach number: $T_p = 1560$ R.

are calculated from the static pressure taps in Figure 3.5(c) using the isentropic pressure relation for a compressible fluid:

$$M_{throat} = \sqrt{\left(\frac{2}{\gamma-1}\right) \left[\left(\frac{P_a}{P_s}\right)^{\frac{\gamma-1}{\gamma}} - 1 \right]} \quad (4)$$

Figure 4.15 shows the chordwise variation of the throat Mach number for the design conditions. The high peaks may be due to impingement of the primary nozzle jets on the ejector wall. Again note that the fuselage side has a slightly higher Mach number level due to the variation of inlet geometry between the two sides.

4.3 Approximate Munk and Prim Similarity Principle

In the prediction of hot ejector flow, a similarity principle that could eliminate the primary nozzle temperature effect on performance, would reduce testing costs and complexity by eliminating the need to conduct experiments at elevated temperatures. If the energy exchange due to viscous stresses could be neglected and the flow thus considered isentropic, the Munk and Prim Similarity Principle would apply (Munk, 1947). This principle is valid for steady, adiabatic, inviscid flow of a perfect gas with constant specific heats.

Simply stated, the Munk and Prim Principle is a guiding philosophy which says that for a fixed geometry and upstream total pressure profile, any change in the upstream total temperature profile does not alter the streamline shapes, Mach

number or total pressure distributions (and therefore momentum) in the device. This can be seen by inspection of the governing equations for isentropic, compressible flow written in terms of the Mach number and pressure (Greitzer, 1985).

Continuity:

$$\nabla \cdot \vec{M} \left[1 + \frac{(\gamma-1)}{2} M^2 \right]^{\frac{-(\gamma+1)}{2(\gamma-1)}} = 0 \quad (5)$$

Momentum:

$$(\vec{M} \cdot \nabla) \vec{M} - \frac{\gamma-1}{\gamma+1} \vec{M} (\nabla \cdot \vec{M}) + \frac{1}{\gamma} \nabla \ln(P) = 0 \quad (6)$$

Momentum expressed in terms of total pressure:

$$\begin{aligned} & (\vec{M} \cdot \nabla) \vec{M} - \left(\frac{\gamma-1}{\gamma+1} \right) \vec{M} (\nabla \cdot \vec{M}) + \\ & - \left(\frac{1}{\gamma-1} \right) \nabla \left[\ln \left(1 + \frac{\gamma-1}{2} M^2 \right) \right] + \frac{1}{\gamma} \nabla \ln(P_T) = 0 \end{aligned} \quad (7)$$

Because continuity and momentum are decoupled from the energy equation (total enthalpy or total temperature does not appear), the Mach number and static and total pressure fields are unchanged with respect to changes in upstream total temperature. The streamline pattern is also unchanged. In other words, a change in total temperature affects only the local velocity, such that the relative distributions remain constant. A derivation of the above equations appears in Appendix E.

The limitation in applying the Munk and Prim Principle to an ejector is that

mixing in an ejector is not isentropic. As shown in Figure 4.16, there are two competing effects: (1) heat transfer from the hot to the cold stream tends to increase the total pressure of the hot stream; and (2) the hot stream has a higher velocity, therefore work (through the turbulent viscous shear layer) is transferred from the hot to the cold stream and decreases the hot stream total pressure. The exchange of work in the viscous shear layer violates the inviscid flow assumption, so in a strict sense the original Munk and Prim analysis is not applicable. However, studies have found that the heat exchange and viscous interaction approximately counteract each other over a wide range of flow conditions, so expanding the similarity principle to include ejector problems would be an appropriate first approximation (see for example Greitzer, Patterson, and Tan; 1985). The purpose of this section is to see how well this assumption holds for our ejector.

As discussed previously, constant pressure performance curves of the data (Figure 4.9) show a thrust augmentation loss as the primary nozzle temperature increases. Supporting this result is Figure 4.17 (Bevilaqua, 1984), which includes the experimental results of eight different ejectors. All the data from the literature shows a slight temperature dependence of the ejector, and although all the data--except that of Lockheed--included a scale or configuration change, the trend is consistent.

The consistency in the data trends indicates that no major problems occurred in the experimental data acquisition. Therefore, the first step in the Munk and Prim analysis involved comparing exit plane Mach number and total pressure profiles of

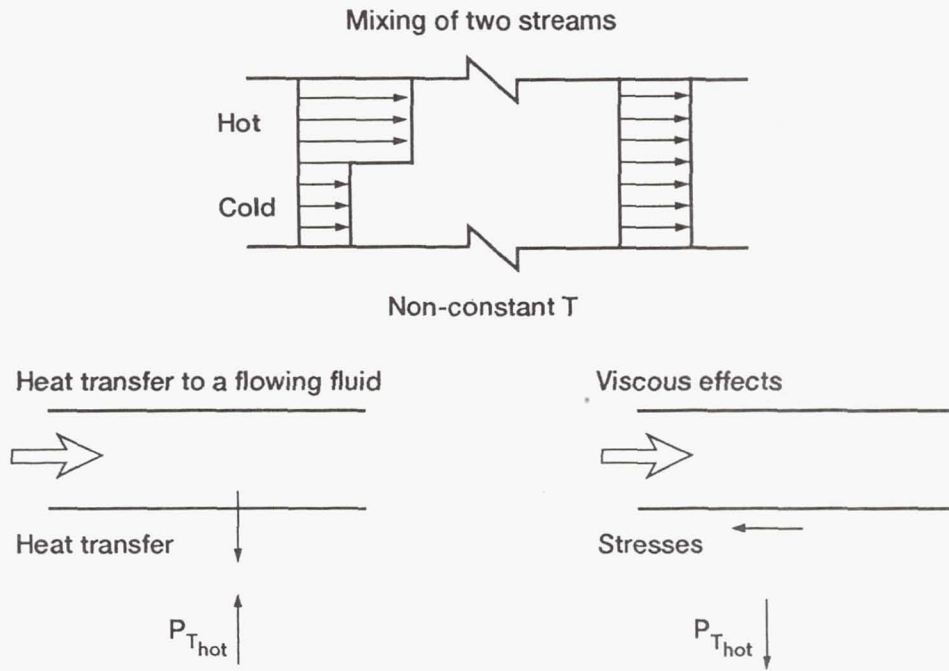


Figure 4.16.—Effect of heat transfer and shear stresses on P_T and M.

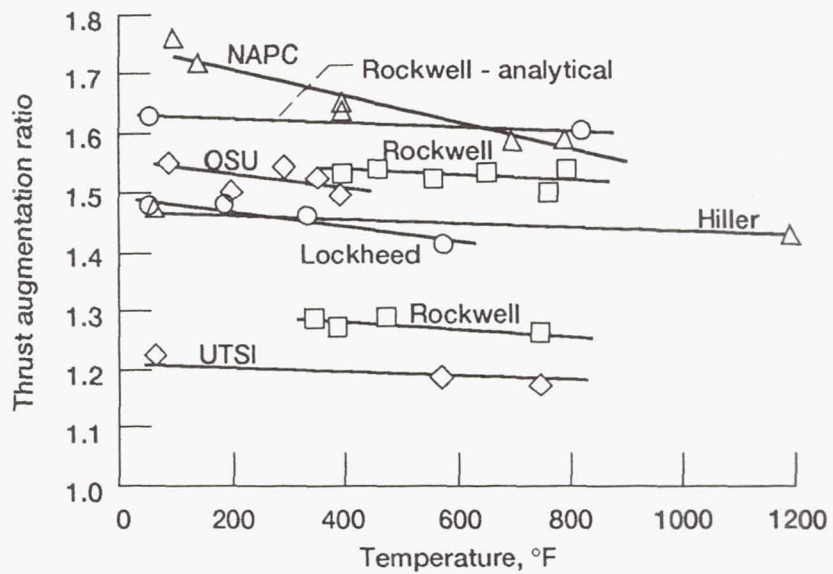


Figure 4.17.—Effect of temperature on ejector thrust augmentation.
 From: Bevilaqua, P.M., "Advances in Ejector Thrust Augmentation", AIAA 84-2425, 1984.

the cold and hot primary flow experiments. For inviscid flow these profiles should stay constant when changing the primary nozzle total temperature. Since Mach number and total pressure exit plane distributions are quite similar, redundant plots are not always presented.

The chordwise Mach number distribution (Figure 4.18) was calculated at each location as the average of the spanwise exit rake values. Although end effects are present, similarity between the two different primary nozzle total temperature data sets can be seen. Other than lowering the local peak values, the change in primary nozzle total temperature did not significantly change the Mach number distribution.

Typical contour plots obtained from the exit rake data are shown in Figure 4.19. Here the cold flow total pressure and Mach number distributions are plotted across the entire exit plane ($NPR = 2.7$). The contours show the overall trends and locations of each nozzle exit, however, the plotting routine's interpolation scheme could not accurately capture the flow details at this scale. To smooth the contours and eliminate any end effects/boundary layer effects, we then looked at the center third of the duct.

Figure 4.20 shows the hot and cold primary nozzle pressure comparison for the center portion of the duct ($NPR = 2.7$), where approximately three and a half nozzle plumes are visible across the chord length. Parts (a) and (b) show the pressure contours, while part (c) shows the 3-D surface plots for a different perspective. Figure 4.21 depicts the Mach number profiles in the same fashion as the total pressure plots. As expected, the contours are definitely similar, however there are

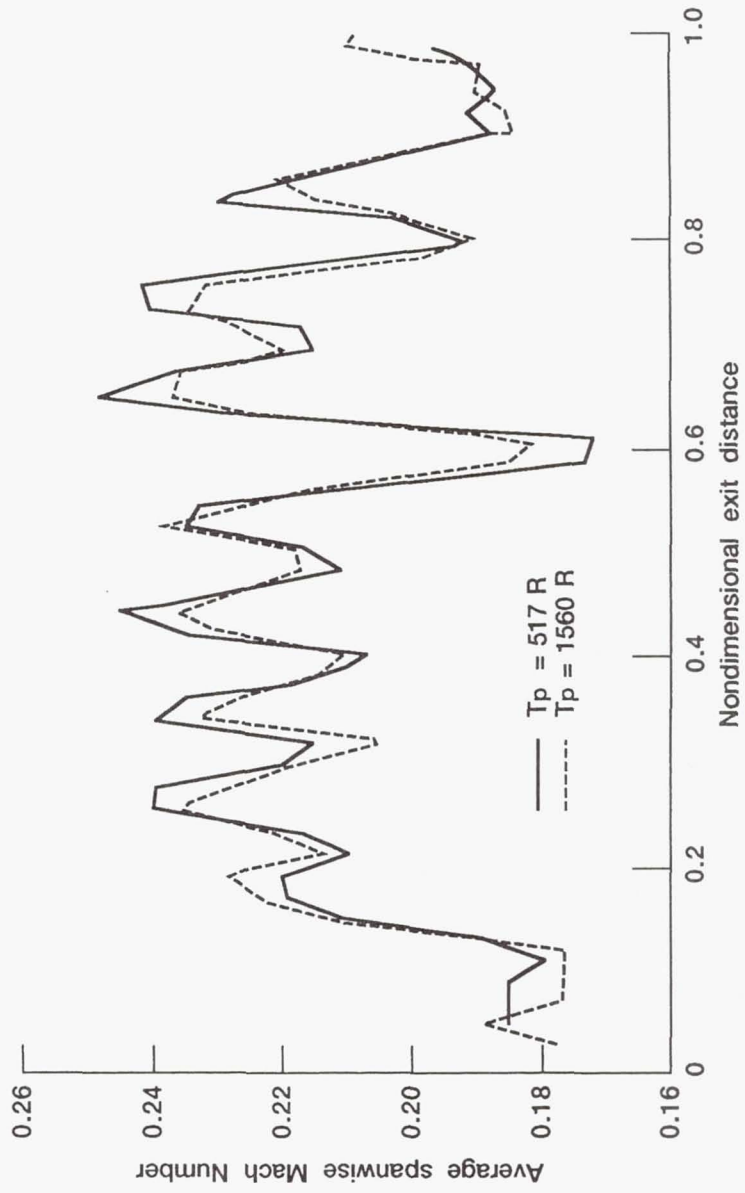


Figure 4.18.—Chordwise ejector exit Mach number distributions.

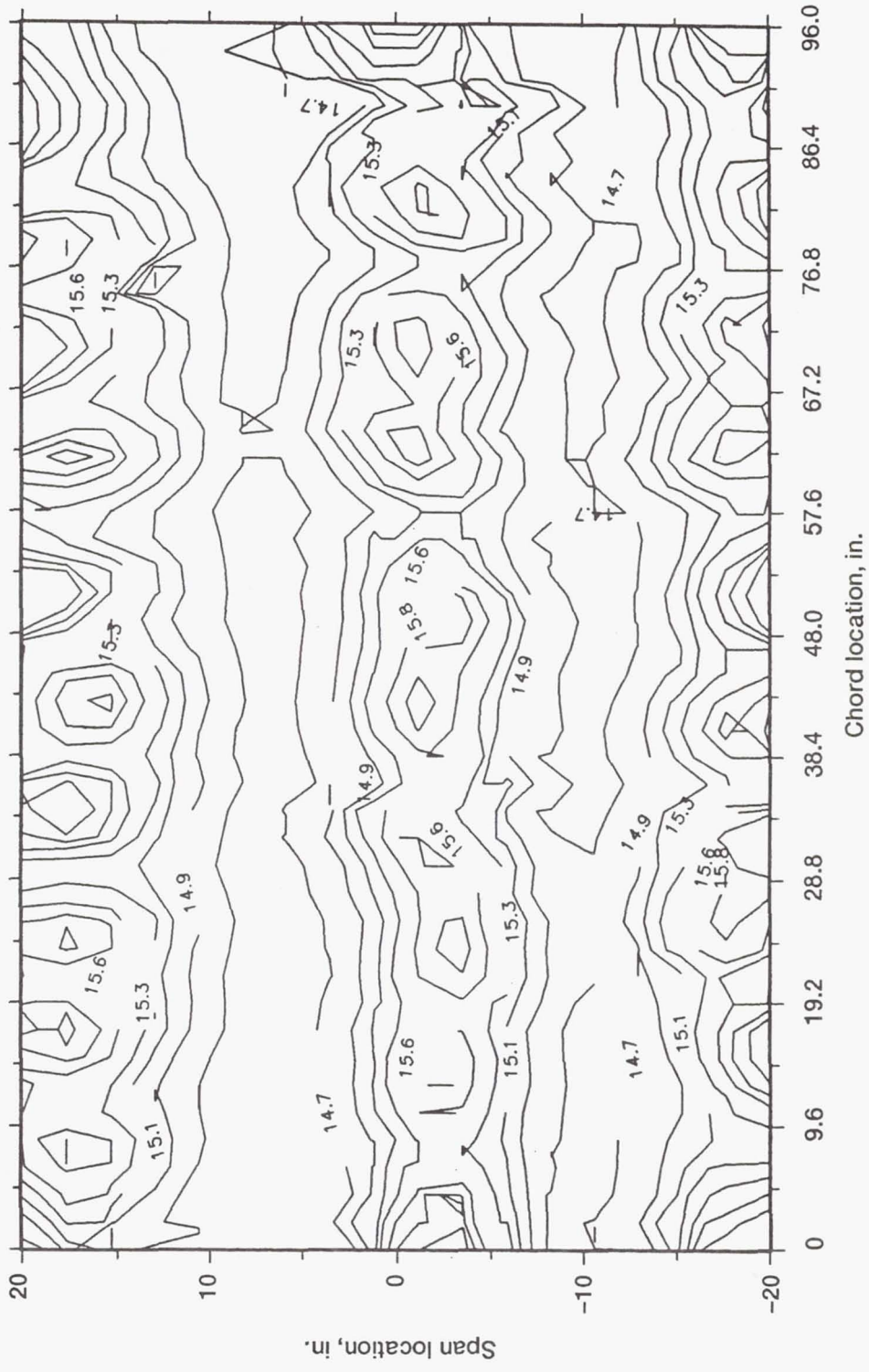


Figure 4.19(a).—Ejector exit total pressure distribution. $T_p = 517$ R.

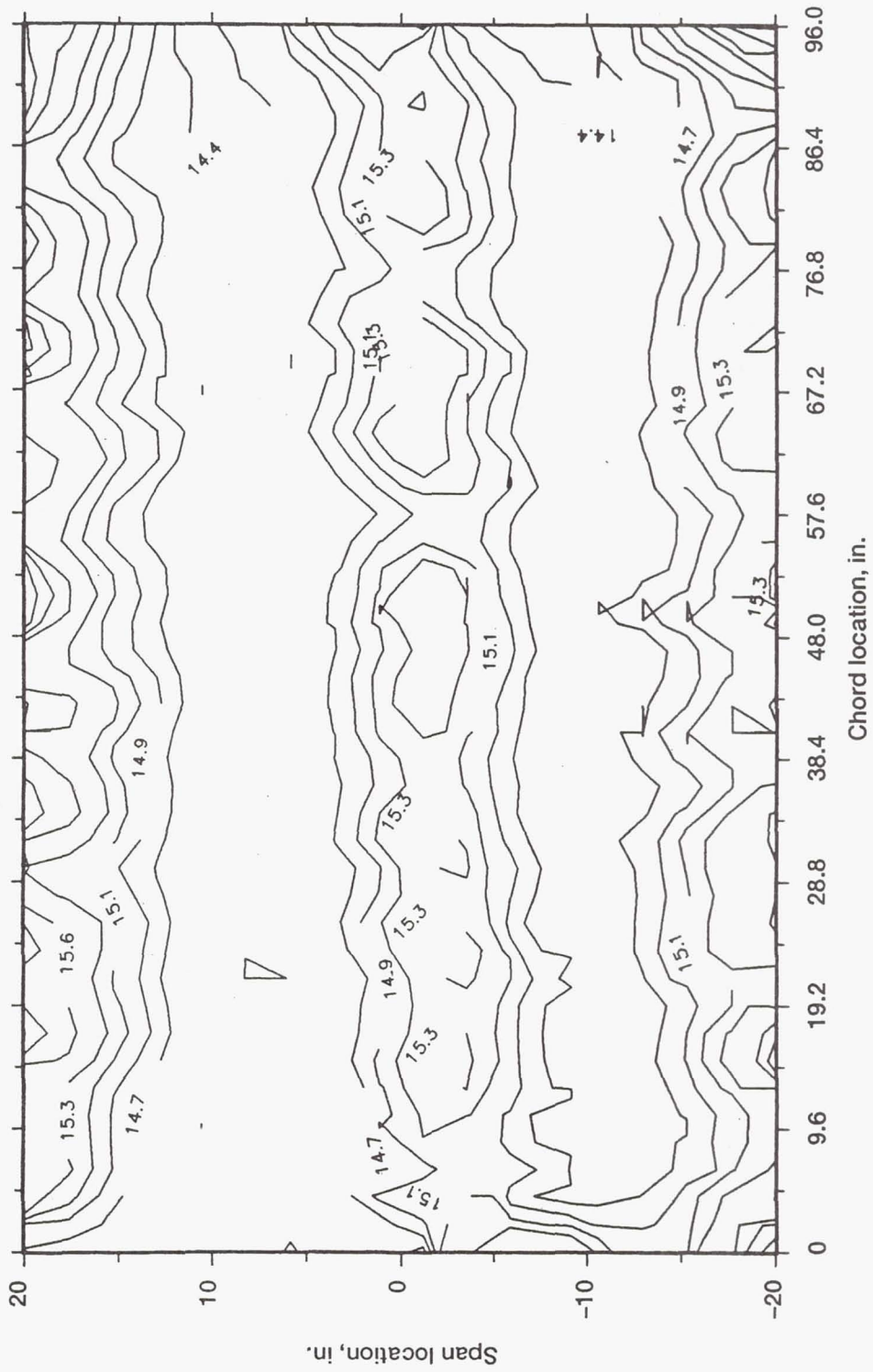


Figure 4.19(b).—Ejector exit total pressure distribution. $T_p = 1560$ R.

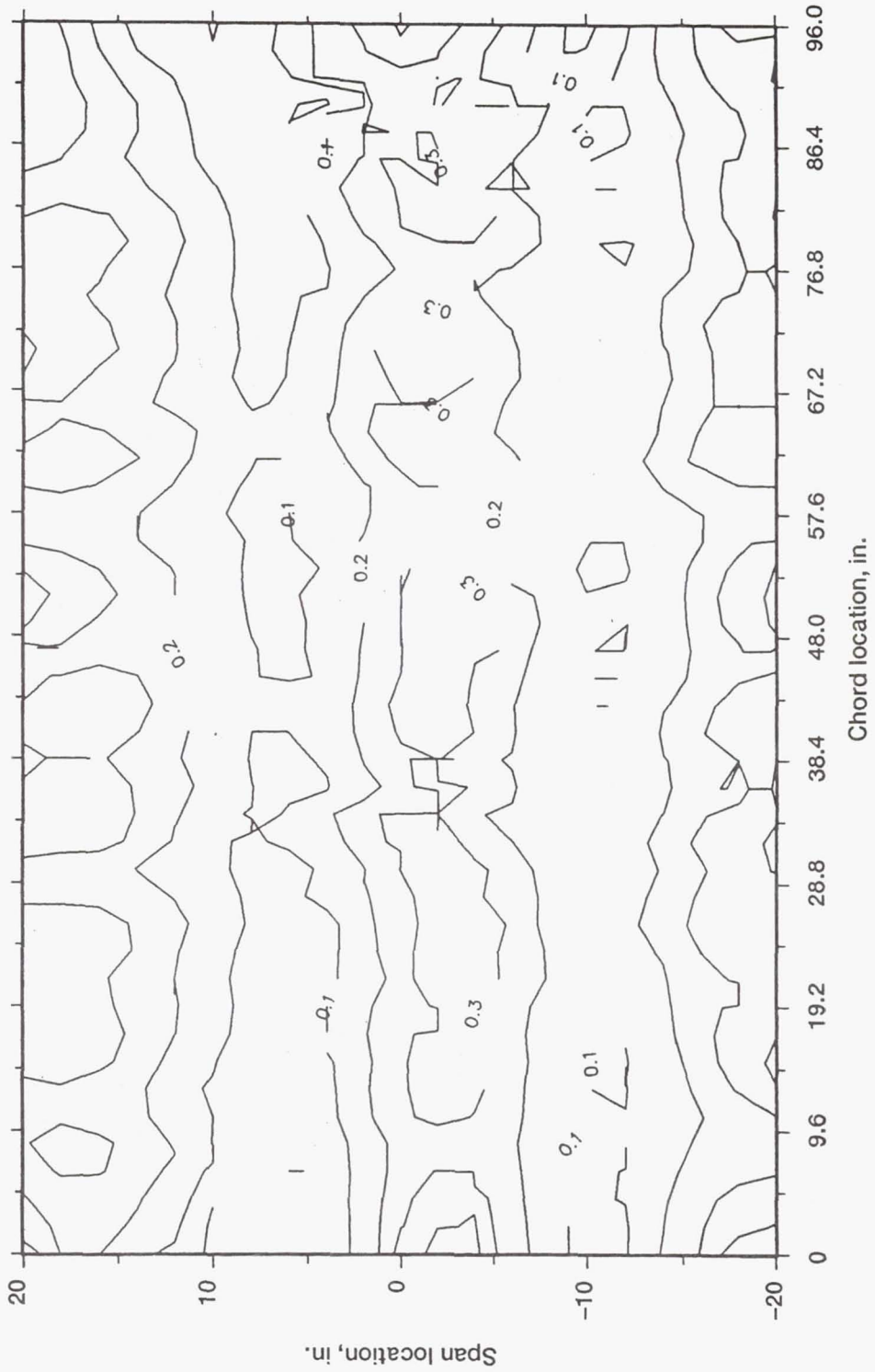


Figure 4.19(c).—Ejector exit Mach number distribution. $T_p = 517$ R.

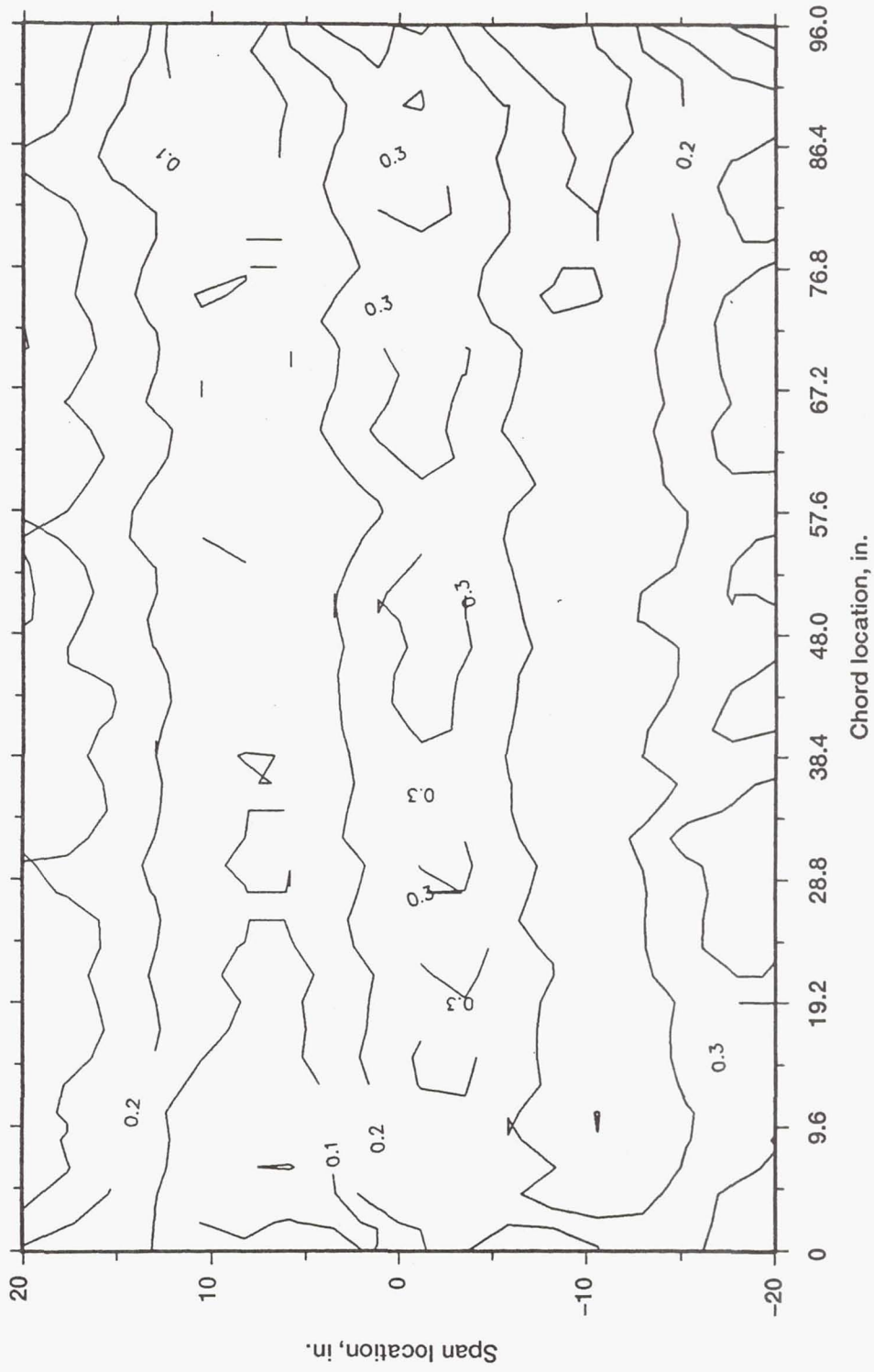


Figure 4.19(d).—Ejector exit Mach number distribution. $T_p = 1560$ R.

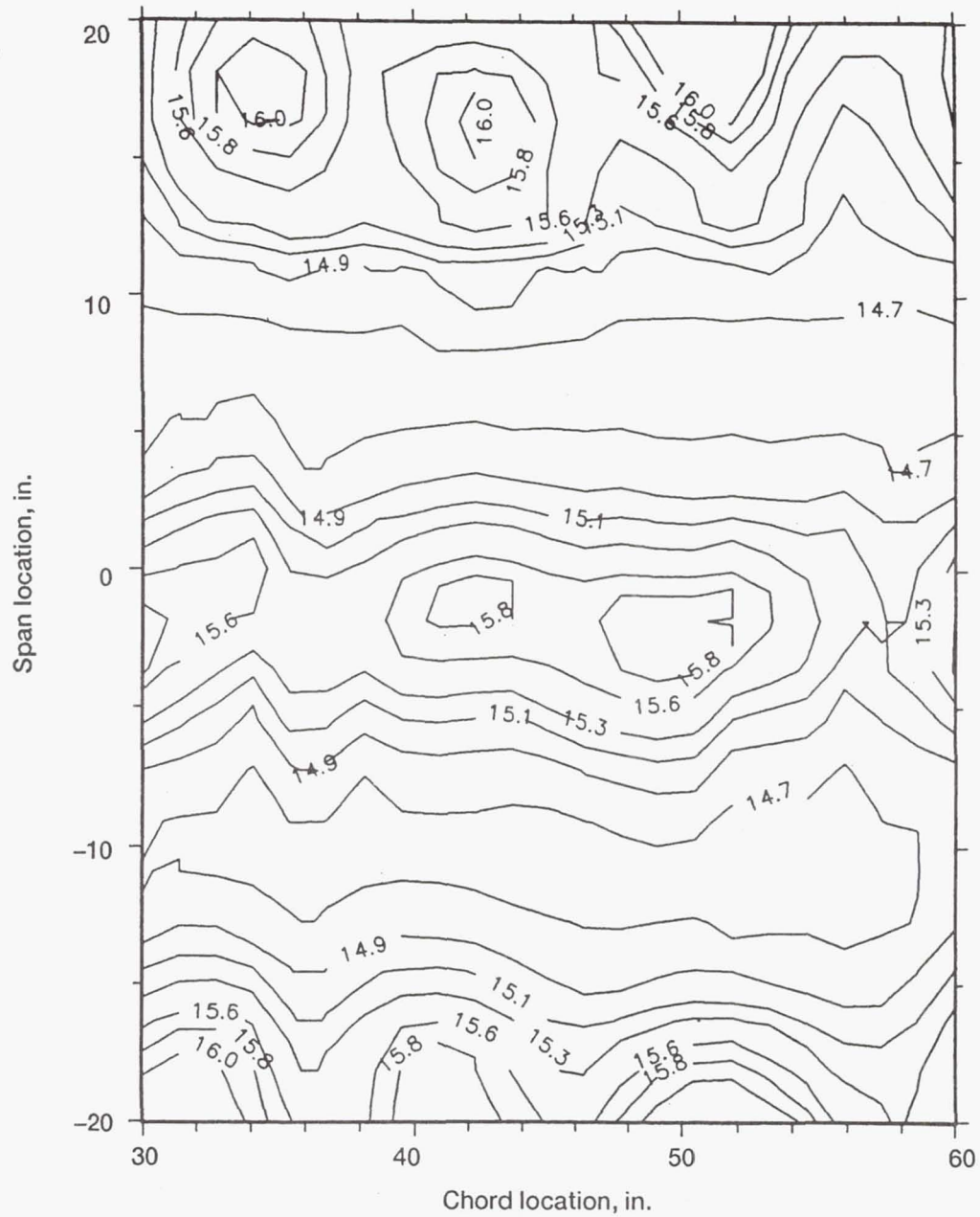


Figure 4.20(a).—Ejector exit total pressure contours of the center nozzles.
 $T_p = 517$ R.

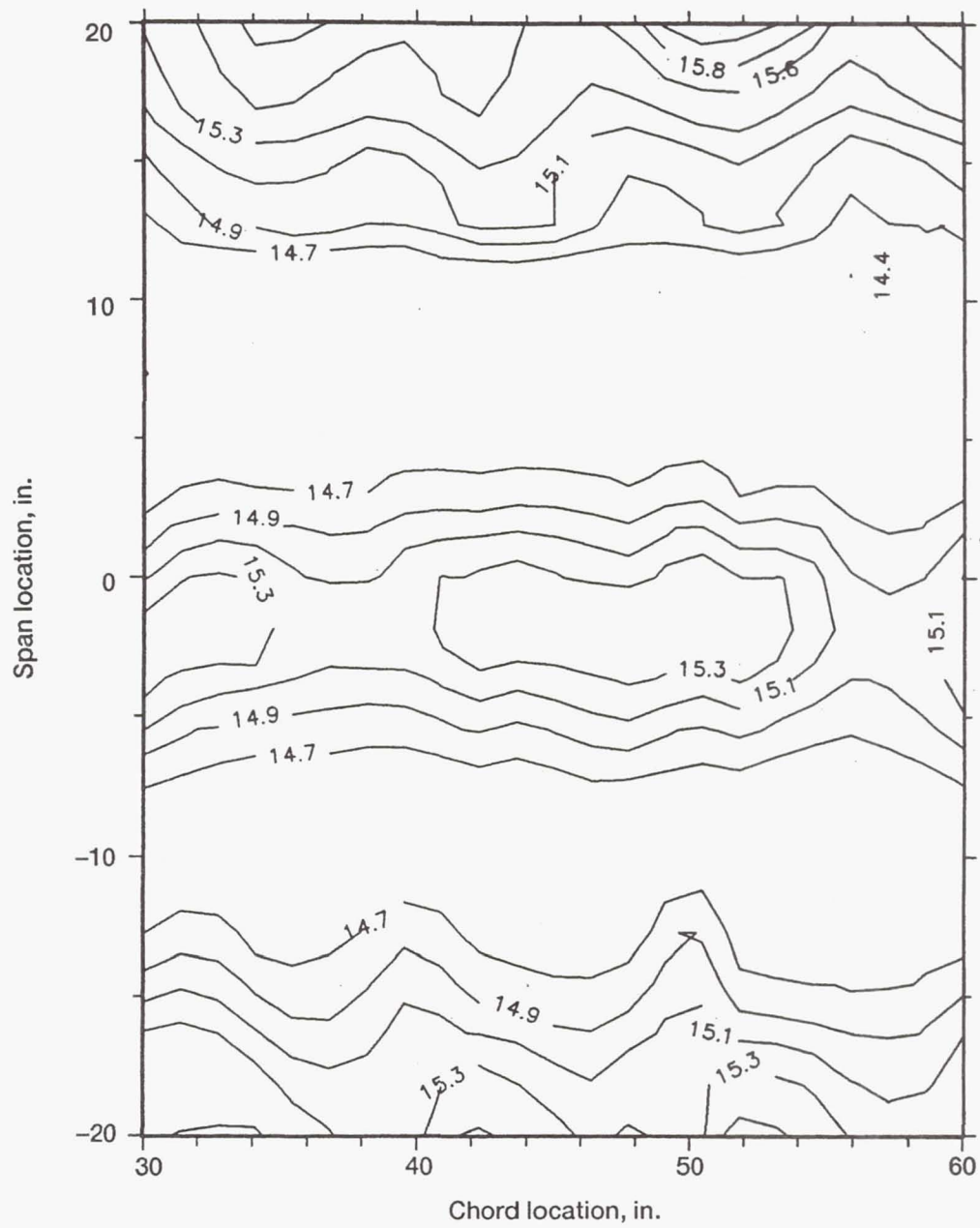
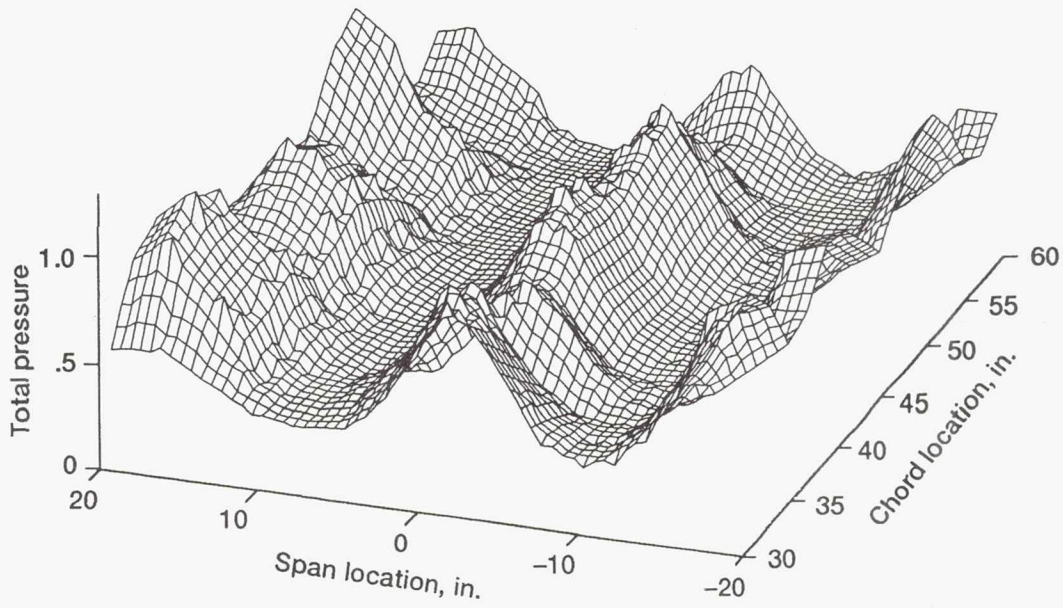


Figure 4.20(b).—Ejector exit total pressure contours of the center nozzles.
 $T_p = 1560$ R.

$T_p = 517 R$



$T_p = 1560 R$

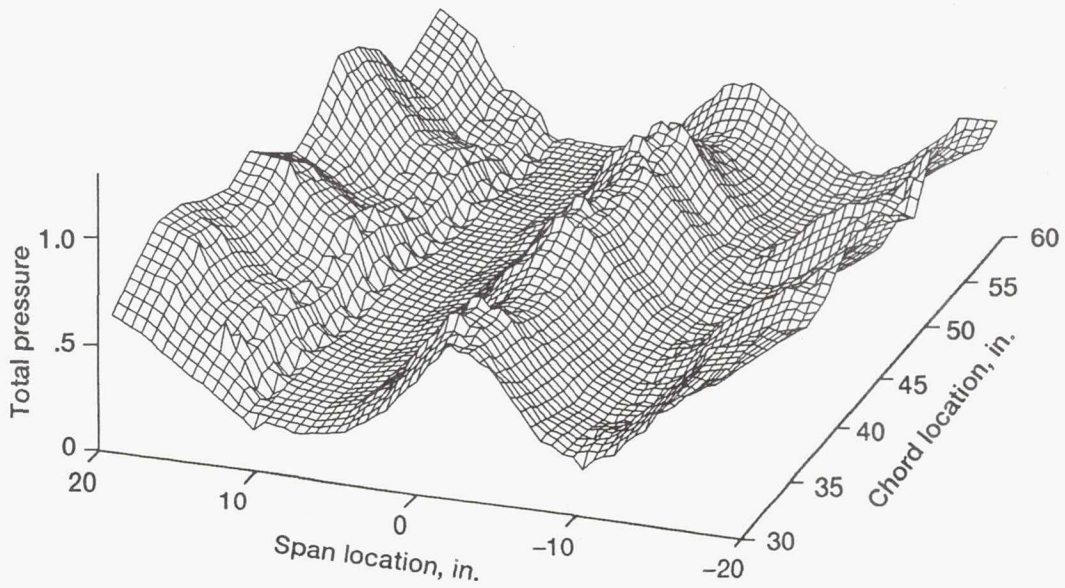


Figure 4.20(c).—Ejector exit total pressure surface plots of the center nozzles.

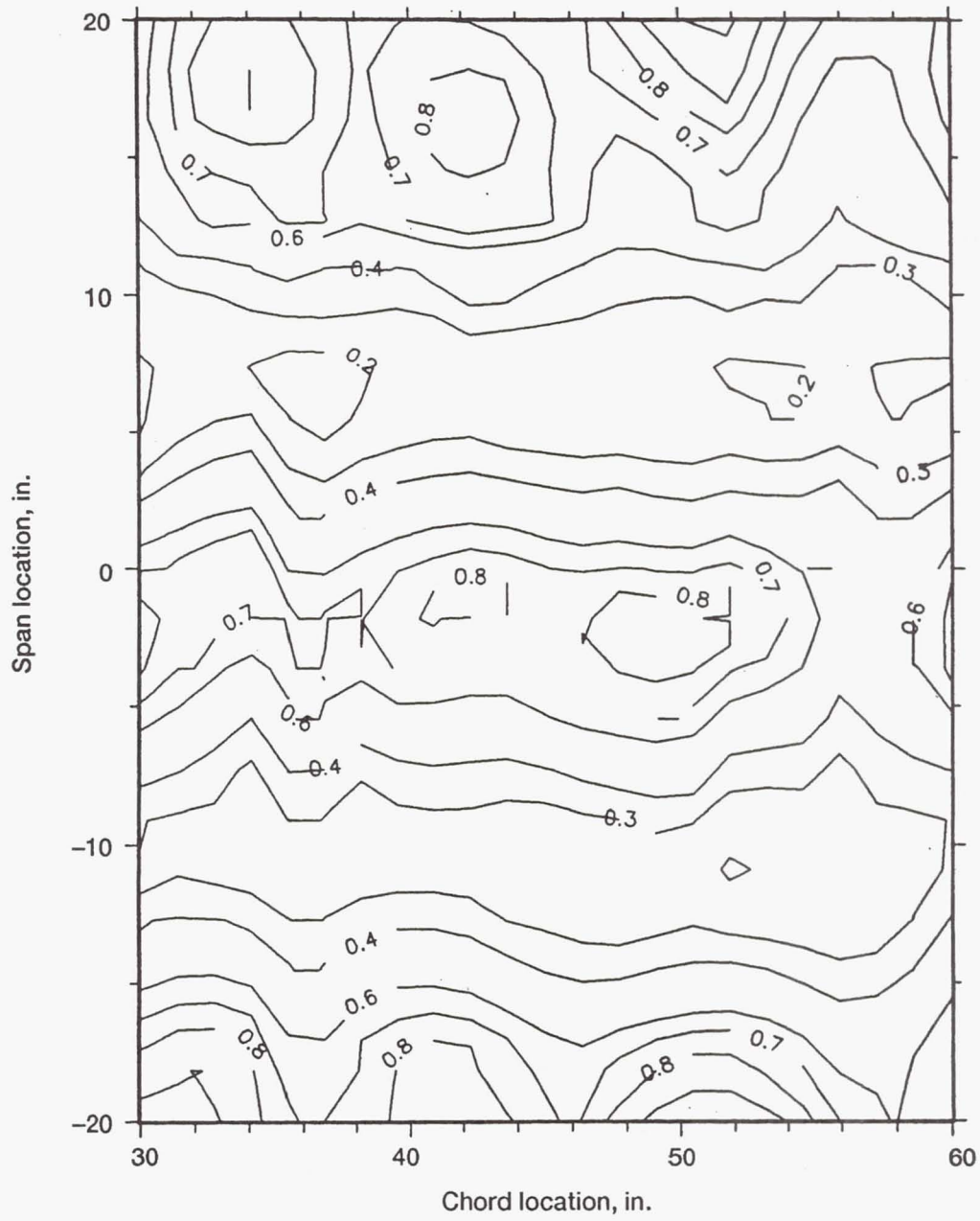
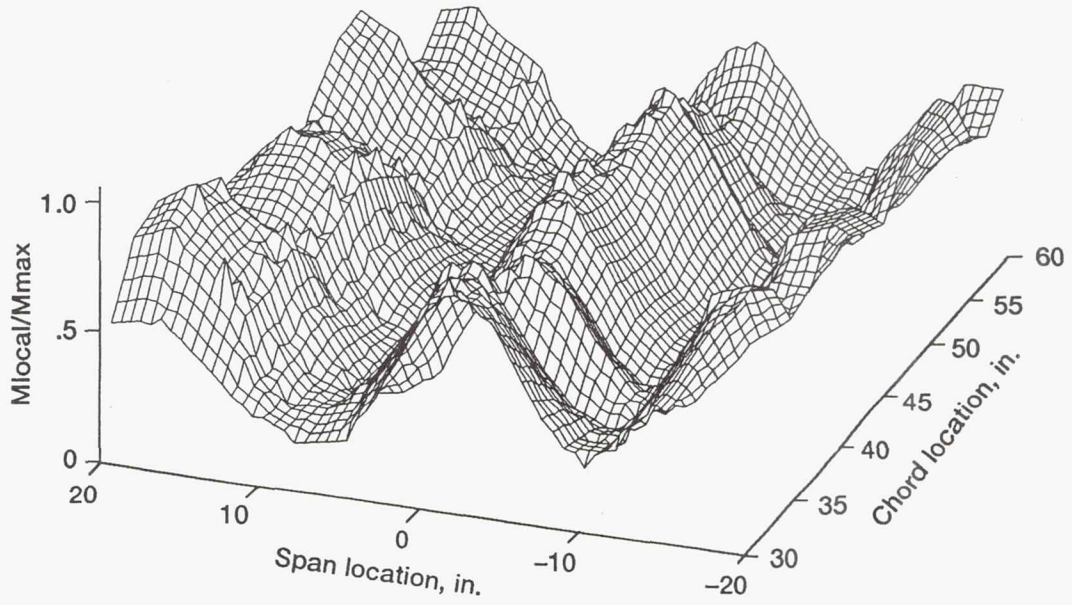


Figure 4.21(a).—Ejector exit Mach number contours of the center nozzles.
 $T_p = 517$ R.

"Page missing from available version"

85

$T_p = 517 R$



$T_p = 1560 R$

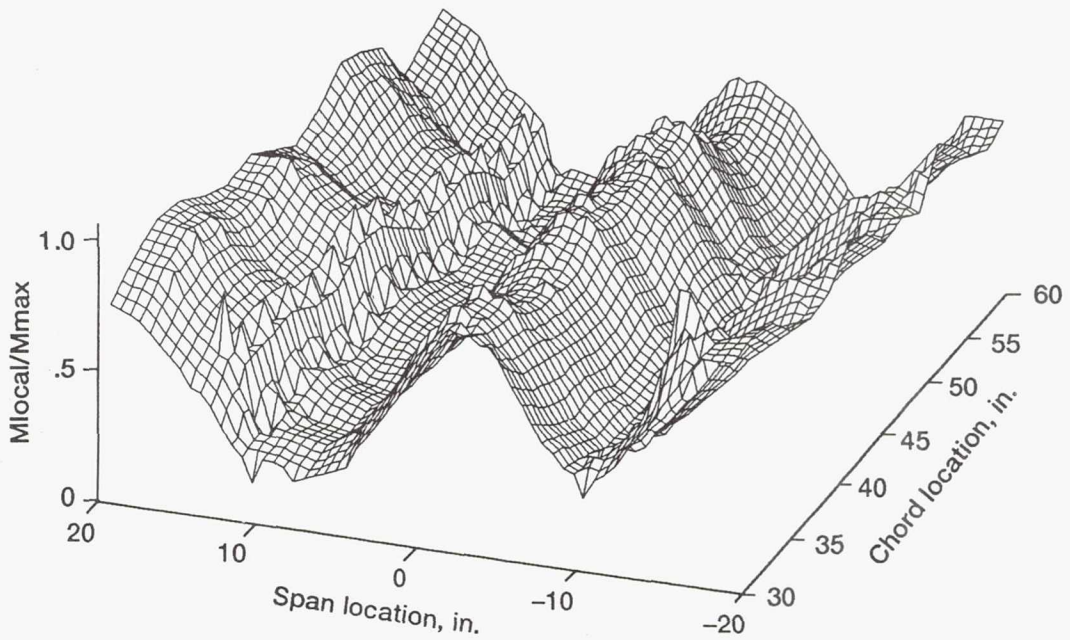


Figure 4.21 (c).—Ejector exit Mach number surface plots of the center nozzles.

a few discrepancies due to experimental error and duct thermal expansion. The qualitative similarity of the distributions suggests that the approximate Munk and Prim principle may be applicable for the thermal scaling of this ejector's performance characteristics.

To investigate the Munk and Prim concept further, it is necessary to obtain a nondimensional parameter that would collapse both the hot and cold flow performance curves into one. Since the Munk and Prim principle is only an interpretation of the governing equations, a specific parameter to use for ejector applications must be obtained by other means. As derived by Presz (1988), a control volume analysis for ejector performance under ideal conditions (incompressible, isentropic) yields:

$$\begin{aligned} & \frac{T_{T_s}}{T_{T_p}} \left(\frac{\dot{m}_s}{\dot{m}_p} \right)^2 \left[\left(\frac{A_p}{A_s} \right)^2 + \left(\frac{A_2}{A_3} \right)^2 \right] + \\ & + 2 \sqrt{\frac{T_{T_s}}{T_{T_p}}} \left(\frac{\dot{m}_s}{\dot{m}_p} \right) \left[1 \left(\frac{A_2}{A_3} \right)^2 \right] + \left[\left(\frac{A_2}{A_3} \right)^2 - 1 - 2 \left(\frac{A_s}{A_p} \right) \right] = 0 \end{aligned} \quad (8)$$

which is nothing more than a quadratic equation. The variable is the nondimensional ejector pumping ratio:

$$\frac{\dot{m}_s}{\dot{m}_p} \sqrt{\frac{T_{T_s}}{T_{T_p}}} \quad (9)$$

which is a function only of ejector geometry. Since we seek a parameter that is invariant with temperature, it is clear that an appropriate nondimensional parameter is the ejector pumping ratio. Although this equation has been derived for low speed flow, compressible flow would follow the same trend.

Figure 4.22 demonstrates the usefulness of the nondimensional pumping parameter. Here, part (a) of the figure shows the mass flow ratio as a function of the primary to secondary pressure ratio for different primary total temperatures at a constant flow area ratio (A_s/A_p). Note, as expected from the control volume analysis, the pumping parameter is fairly constant with respect to changes in the total pressure ratio. The slight variation with the pressure ratio is due to compressibility effects that were assumed negligible in the control volume formulation. Part (b) of the figure shows that the normalized pumping parameter collapses the results such that the temperature effects drop out. Again there is a slight compressibility effect present. Also note that if the flow was actually isentropic, the temperature curves should completely collapse with the pumping ratio. The slight difference in the temperature curves is due to the inviscid assumption imposed on the ejector. Since the normalized pumping parameter "washes out" the jet temperature effects, it seems an appropriate factor to use in characterizing ejector performance.

For ideal flow the thrust augmentation ratio can be expressed as:

$$\phi = 1 + \left(\frac{M_s}{M_p} \right) \left[\frac{\dot{m}_s}{\dot{m}_p} \sqrt{\frac{T_{T_s}}{T_{T_p}}} \right] \quad (10)$$

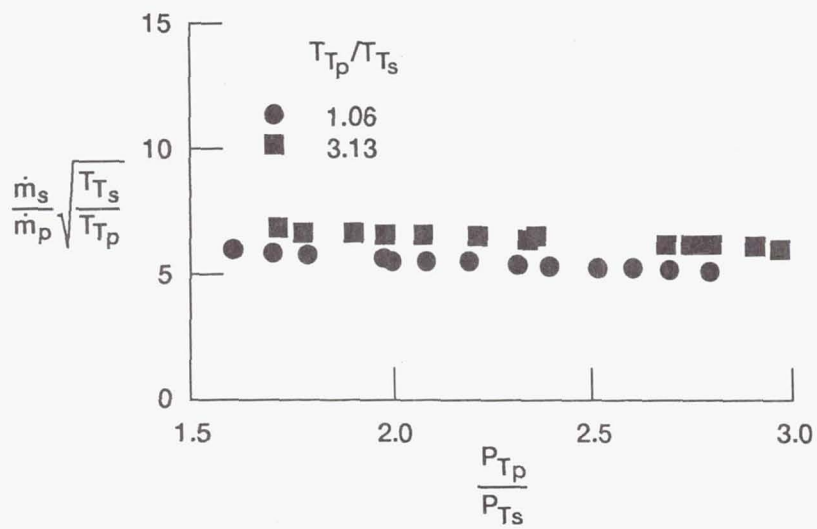
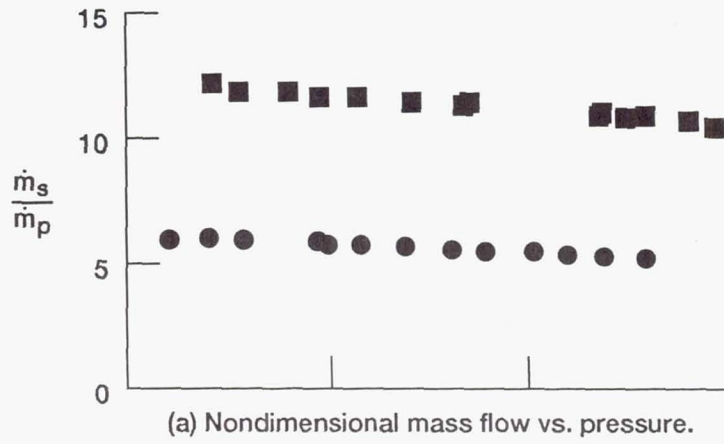


Figure 4.22.— Normalized pumping parameter at constant ejector area ratio.

derived from a control volume analysis in which the pressure-area terms were neglected (first order approximation). At first glance it may appear that the ideal flow thrust augmentation ratio varies with the normalized pumping parameter. However, the Mach number ratio is constant through the Munk and Prim principle and the normalized pumping parameter is only a function of ejector geometry (equation 8). This implies that for the same geometry and inflow total pressure distribution, the normalized ejector performance (thrust augmentation ratio) should be invariant with the normalized pumping parameter. Momentum and energy effects are contained in the normalization.

In Figure 4.23 the thrust augmentation ratio was plotted against the normalized pumping parameter. The data reflects a very weak dependency between these two parameters and thus this data supports the fundamental premise of the approximate Munk and Prim similarity principle. It should be noted that we are able to plot Figure 4.23 because of the viscous and thermal non-idealistic mixing of the ejector. In other words, violation of the basic assumptions used to invoke the Munk and Prim principle. The excursion of the data from the proposed ideal slope (Figure 4.23) has a consistent trend for both cold and hot temperatures. A linear Least Squares regression was invoked on both the hot and cold data. The correlation is as follows:

$$\phi = 1.813 - (0.052) \frac{\dot{m}_s}{\dot{m}_p} \sqrt{\frac{T_{T_s}}{T_{T_p}}} \quad (11)$$

Therefore, for this ejector, hot flow performance can be approximated by cold flow

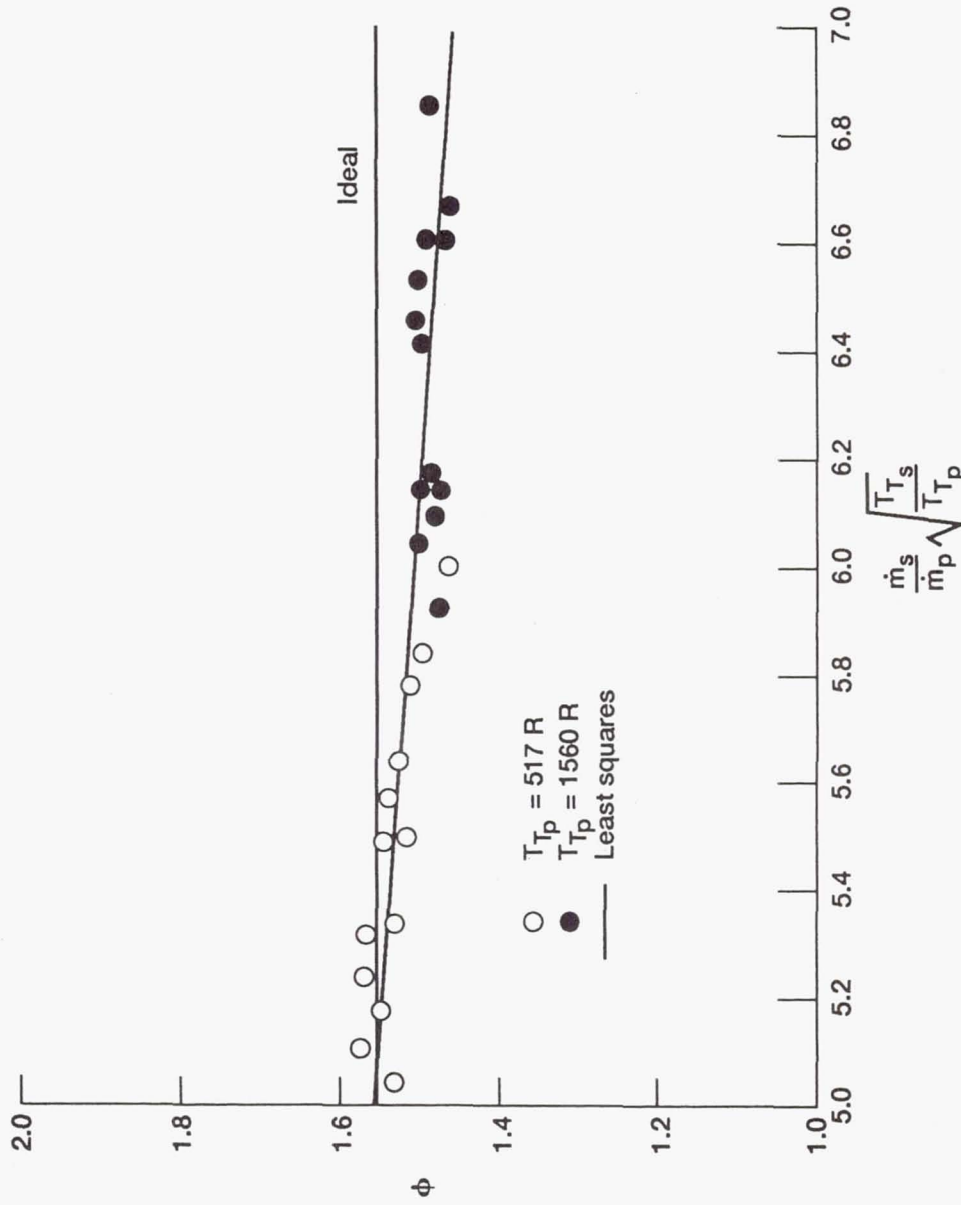


Figure 4.23.—Performance vs. nondimensional flow.

data according to the approximate Munk and Prim principle with only a slight over-prediction.

Although equation 11 is valid for this ejector only, this type of correlation could be useful in experimental research on other ejectors. Remember that the original purpose of using a similarity principle was to eliminate the primary nozzle temperature effect on ejector performance, and subsequently reduce both model and testing costs. If one was not satisfied with a first cut approximation of the Munk and Prim principle (no performance difference between hot and cold) then cold flow data could be taken, the curve fit drawn, and hot flow data extrapolated at considerably less experimental expense.

CHAPTER V

CONCLUDING REMARKS

The "STOVL penalty" can be described as the increase in aircraft weight (or engine size) that occurs with the addition of vertical lift devices. Dealing with this penalty could significantly impact the design process, since adding extra components increases the aircraft weight, which requires a larger engine. Therefore, one must optimize the benefit of vertical lift vs. engine size. For ejectors this means two things:

1. Keep the diffuser length short (and thin) so as not to drastically increase the frontal area forward drag. However, this shorter mixing length may not be sufficient to allow adequate mixing to occur, thus reducing augmentation. To obtain enough vertical lift, a larger ejector is needed and the design cycle repeats itself.
2. Increase A_s/A_p (use less engine air). This requires a smaller engine since less air is diverted to the ejectors. It also leaves a cooler footprint since there is proportionally more secondary air. However, you do need to

optimize the design or the performance will drop.

Previous E-7A ejector testing on the PLF (Garland, 1989) produced augmentation ratios ≈ 1.7 for an $A_s/A_p = 23$. Therefore in this ejector design, the goal was to reduce the amount of primary air flow as much as possible ($A_s/A_p = 30$), while still attaining adequate thrust augmentation. The diffuser length of this ejector was also shortened in design.

Static tests of this full-scale lift ejector showed that at a primary-nozzle pressure ratio of 2.7, thrust augmentation ratios of 1.47 (primary-jet temperature at 1560 R) to 1.59 (primary jet temperature at ambient) were obtained. It should be noted that this is a unique experiment, incorporating a full-scale flight-type model operating at design pressures and engine exhaust temperatures.

Cold flow augmentation ratios were increased from 1.52 to 1.59 by several modifications which decreased inlet losses and increased mixing. These modifications were of three types and included:

1. Inlet

- Replace inlet door with a curved leading edge.
- Install a downstream vertical plate.
- Install a larger upstream curved leading edge.

2. Nozzle

- Install fairings at the nozzle roots.
- Enlarge the inside nozzle exit notches.
- Install leading edge fairings on the first three nozzles.

3. Shroud wall

- Install a plywood spacer flush with the downstream end-plate.

Both hot and cold data showed approximately a 2% reduction in the augmentation ratio as the secondary (ambient) temperature decreased roughly 40 R (i.e. $T_p - T_s$ increased). Augmentation reduction occurred faster when the secondary temperature decreased than when the primary temperature increased.

Although the cold flow tests resulted in a higher overall augmentation, the hot flow exit-rake augmentation distributions showed a more uniform profile having a smaller peak-to-valley distance; indicative of better mixing. In general, the exit rake distributions showed less mixing than expected, but exit temperatures and pressures remained low. This incomplete mixing is due to unknown design sensitivities. Slight geometric variations have a great effect on thrust augmentation, implying that ejector design is still somewhat of an art. In trying to overcome the STOVL penalty and obtain the greatest augmentation, the result is an optimistically short mixing length (diffuser length)

Rake augmentation ratio was much lower near the fore and aft ends of the ejector than in the middle. If one were to ignore both the deficit between nozzles #6 and #7 and the end effect degradation, a closer examination of the rake distribution would yield an integrated rake augmentation in the vicinity of 1.70. Thus, improvements to ejector efficiency near the end plates is seen as the key to obtaining higher augmentation ratios.

The similarity between hot and cold flow experiments was confirmed for the full-

scale ejector data. The present experimental data showed a 4% decrease in augmentation ratio for a primary nozzle temperature increase of 1000 R, while supporting data from the literature showed that cold air jets may overpredict the thrust augmentation ratio by approximately 2-3%. Consistent with the Munk and Prim similarity principle, the total pressure and Mach number distributions for different primary nozzle total temperatures were found to be quite similar. Thus, for a first cut approximation, the Munk & Prim Similarity Principle holds for this ejector configuration and shows that temperature effects are relatively small and compensating, even when there is substantial viscous and heat transfer effects. An ejector pumping parameter was used to significantly reduce the temperature dependence in the performance curves by plotting the pumping parameter vs. primary nozzle pressure for constant geometry. The end result is that cold flow tests can be used to obtain a rough prediction of hot flow results at reduced time, cost, and complexity.

BIBLIOGRAPHY

- Anderson, J.D., "Fundamentals of Aerodynamics," McGraw-Hill, Inc., New York, 1991.
- Barankiewicz, W.S., "Static Performance Tests of a Flight-Type STOVL Ejector," NASA TM-104437, 1991.
- Barankiewicz, W.S., Perusek, G.P. and Ibrahim, M., "Use of an Approximate Similarity Principle for the Thermal Scaling of a Full-Scale Thrust Augmenting Ejector," AIAA Paper 92-3792, 1992.
- Batterton, P.G. and Blaha, B., "NASA Supersonic STOVL Propulsion Technology Program," NASA TM-100227, 1987.
- Bernal, L. and Sarohia, V., "An Experimental Investigation of Two-Dimensional Thrust Augmenting Ejectors: Final Report, Part II," N85-12895, 1984.
- Bevilaqua, P.M., "Advances in Ejector Thrust Augmentation," AIAA Paper 84-2425, 1984.
- Bevilaqua, P.M. and DeJoode, A.D., "Viscid/Inviscid Interaction Analysis of Thrust Augmenting Ejectors," ONR-CR12-249-1, 1978.
- Biesiadny, T., "V/STOL Gets a Lift," Aerospace America, pp. 52-55, September 1991.
- Bullock, C.E., and Haroutunian, V., "Analysis of Air Circulation Patterns Within the Sistine Chapel With a Proposed Air Conditioning System," Proceedings of the Third FIDAP User's Conference, Fluid Dynamics International, Inc., Evanston, Illinois, 1989.
- Corsiglia, V., Farbridge, J., Dudley, M. and Smith, B., "Large-Scale Wind Tunnel Tests of an Ejector-Lift STOVL Aircraft Model," AIAA Paper 89-2905, 1989.
- Deckert, W.H. and Franklin, J.A., "Powered-Lift Technology on the Threshold," Aerospace America, pp. 34-42, November 1985.
- Deese, J.E. and Agarwal, R.K., "A Numerical Study of Viscous Flow in Inlets and Augmentors," AIAA Paper 88-0187, 1988.
- De Frate, L.A. and Hoerl, A.E., "Optimum Design of Ejectors Using Digital Computers," Chemical Engineering Progress Symposium Series, vol. 55, No. 21, pp. 43-51.

- Drummond, C.K., "A Control-Volume Method for Analysis of Unsteady Thrust Augmenting Ejector Flows," NASA CR-182203, 1988.
- Garrard, G., Phares, W. and Cooper, G., "Calibration of PARC for Propulsion Flows," AIAA Paper 91-2152, 1991.
- Garland, D. B., "Development of Lift Ejectors for STOVL Combat Aircraft," AIAA Paper 87-2324, 1987.
- Garland, D.B., "Static Tests of a Full Scale Lift Ejector for the E7A Wind Tunnel Model at the NASA Lewis Research Center," de Havilland Aircraft Company, DHC-DRIE 88-5, 1989.
- Garland, D.B. and Gilbertson, F.L., "A Review of Scale Effects on the Static Performance of Lift Ejectors," AIAA Paper 90-1819, 1990.
- Greitzer, E.M., Paterson, R.W., and Tan, C.S., "An Approximate Substitution Principle for Viscous Heat Conducting Flows," Proc. R. Society London, A401, 163-193, 1985.
- Harris, C.M., "Handbook of Noise Control," Mc Graw - Hill Book Company, 1957.
- Kidwell, G.H. and Lampkin, B.A., "An Evaluation of Supersonic STOVL Technology," AIAA Paper 83-2493, 1983.
- Kinsler, L.E., et.al., "Fundamentals of Acoustics," third edition, John Wiley & Sons, 1982.
- Levine, J. and Inglis, M., "US/UK Advanced Short Takeoff and Vertical Landing Program (ASTOVL)," AIAA Paper 89-2039, 1989.
- McAmis, R. and Bartlett, C., "Aerodynamic Free-Jet Nozzle Performance Augmentation Using an Exhaust Diffuser," AIAA Paper 91-2270, 1991.
- Munk, M. and Prim, R.C., "On the Multiplicity of Steady Gas Flows Having the Same Streamline Pattern," Proceedings of the National Academy of Science, U.S.A., vol. 33, pp. 137-141, 1947.
- "PLF Noise Abatement Plan," Environmental Health and Chemical Analysis Branch, NASA Lewis Research Center, November, 1989.
- Porter, J.L. and Squyers, R.A., "A Summary/Overview of Ejector Augmentor Theory and Performance," ATC Report No. R-91100/9CR-47A, Vought Corporation Advanced Technology Center, Dallas Texas. Also, USAF Technical Report

No. R-91100/9CR-47, Volumes I and II, April 1981.

- Presz, W.M. Jr., "Mixer/Ejector Noise Suppressors," AIAA Paper 91-2243, 1991.
- Presz, W.M. Jr. and Greitzer, E.M., "A Useful Similarity Principle for Jet Engine Exhaust System Performance," AIAA Paper 88-3001, 1988.
- Quinn, B., "Compact Ejector Thrust Augmentation," *Journal of Aircraft*, vol. 10, No. 8, pp. 481-486, August 1973.
- Saad, M.A., "Compressible Fluid Flow," Prentice-Hall, Inc., New Jersey, 1985.
- Salter, G.R., "Method for Analysis of V/STOL Aircraft Ejectors," *Journal of Aircraft*, vol. 12, No. 12, pp. 974-978, December 1975.
- Shapiro, A.H., "The Dynamics and Thermodynamics of Compressible Fluid Flow vol. I," The Ronald Press Company, New York, 1953.
- Stitt, L.E., "Exhaust Nozzles for Propulsion Systems With Emphasis on Supersonic Cruise Aircraft," NASA RP-1235, 1990.
- White, F.M., "Viscous Fluid Flow," McGraw-Hill Publishing Co., New York, 1974.
- Whittle, D.C., "Large Scale Model Tests of a New Technology V/STOL Concept," AIAA Paper 80-0233, 1980.
- Whittle, D.C. and Gilbertson, F.L., "Recent Developments in Ejector Design for V/STOL Aircraft," SAE Paper 841498, 1984.
- Whittle, D.C. and Koenig, D.G., "Large Scale Model Tests of a New Technology V/STOL Concept," AIAA Paper 80-0233, 1980.
- Wilson, S.B. and Wurts, J.M., "Harrier III-AV8B With a Modern Engine," SAE Paper 851881, 1985.
- Yang, T., Ntone, F., Jiang, T., and Pitts, D.R., "An Investigation of High Performance, Short Thrust Augmenting Ejectors," *Journal of Fluids Engineering*, Vol. 107, pp. 23-30, March 1985.

APPENDICES

Appendix A

Ejector Thrust Improvement Over an Isolated Nozzle

An isolated convergent nozzle net static thrust can be represented as:

$$T = \dot{m} V_e + A_e(P_e - P_\infty) \quad (\text{A1})$$

or:

$$\frac{T}{P_T A^*} = \frac{\dot{m}}{P_T A^*} V_e + \frac{A_e}{A^*} \left(\frac{P_e}{P_T} - \frac{P_\infty}{P_T} \right) \quad (\text{A2})$$

for choking flow:

$$\frac{\dot{m}}{P_T A^*} = \frac{1}{\sqrt{T_T}} \sqrt{\frac{\gamma}{R} \left(\frac{2}{\gamma+1} \right)^{\frac{\gamma+1}{\gamma-1}}} \quad (\text{A3})$$

combining the energy equation and isentropic law:

$$V_e = \sqrt{2 C_p T_T} \sqrt{1 - \left(\frac{P_e}{P_T} \right)^{\frac{\gamma-1}{\gamma}}} \quad (\text{A4})$$

substituting equations A3 and A4 into A2:

$$\frac{T}{P_T A^*} = \gamma \sqrt{\frac{2}{\gamma-1} \left(\frac{2}{\gamma+1} \right)^{\frac{\gamma+1}{\gamma-1}}} \sqrt{1 - \left(\frac{P_e}{P_T} \right)^{\frac{\gamma-1}{\gamma}}} + \frac{A_e}{A^*} \left(\frac{P_e}{P_T} - \frac{P_\infty}{P_T} \right) \quad (\text{A5})$$

it can be show through much manipulation (Shapiro [1953]) that:

$$T_{\max} \text{ occurs when } P_e = P_\infty$$

The same result may also be obtained by taking a heuristic look at the problem. Assume, as in Figure A.1, there is a certain plane where $P_e = P_\infty$. Continuing the nozzle would decrease the internal pressure ($P_e < P_\infty$), and the added piece would have a negative thrust (drag). In the same fashion, removing a piece of nozzle upstream would also act to reduce the thrust.

Now when you add an ejector shroud, instead of changing P_e you lower P_∞ . To view this, imagine extending the nozzle (with positive thrust) until P_e once again equals P_∞ . The ejector thus provides more thrust capability than an isolated nozzle.

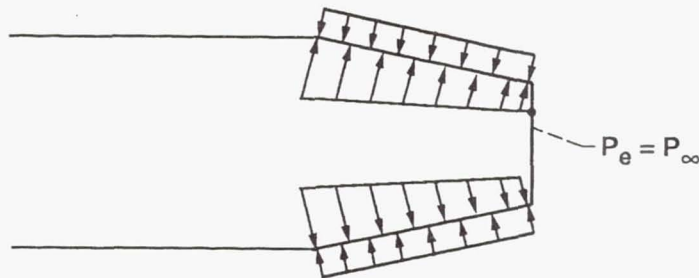


Figure A.1.—Convergent nozzle pressure distribution.

Appendix B

Ejector Community Noise Problem

Many of the propulsion devices tested at the PLF generate quite a bit of noise. The worst of these are the large conical calibration nozzles run at sonic flow pressures. The high intensity (and very annoying) screech noise developed at these pressures has sensitized the community in the vicinity of the PLF. Since NASA has always been a "good neighbor," a temporary noise limit of 77 dbA was set at the edge of this community, and testing constraints were documented in the PLF Noise Abatement Plan (1989).

Some of these constraints are:

1. Testing shall occur only between the hours of 6:00 p.m. and 10:00 p.m.
2. Testing shall not occur on nights when weather conditions exist that are known to propagate high noise levels to the surrounding communities.
3. The lowest possible nozzle pressure ratio required to fulfill research needs will be determined, and serve as an upper bound on testing. All test points must be below the community noise limit, or they will not be run.
4. Shortened research data scans will be employed where possible.
5. Implement automated nozzle exit traverse mechanism to shorten traverse time.

Estimated noise values were 65.3 dbA for cold primary nozzle flow, and 73 dbA

for hot primary nozzle flow. Actual noise data obtained were 65 dbA cold, and 75 dbA hot. Be cautioned however, that these numbers are not exclusive. There are many factors that affect the sound level. The most notable of these are the atmospheric conditions. Ordinarily, the sound pressure level decreases away from the source due to the divergence of sound waves. This is approximately a 6 db drop with each doubling of the distance away from the point source. However when certain atmospheric conditions are present (such as wind, clouds, storms, etc.), the sound waves are reflected making the same test conditions louder at the community boundary.

Although not present during the ejector testing, the facility is now enclosed by a 65 foot radius acoustically treated geodesic dome (Figure B.1). The dome limits noise exposure to the surrounding communities and allows for virtually year-round testing. Because of the proximity of the dome wall to the thrust frame, nozzles can not be vectored upward without some flow deflection device. Nozzles are usually vectored downward, or axially out the dome exhaust door.

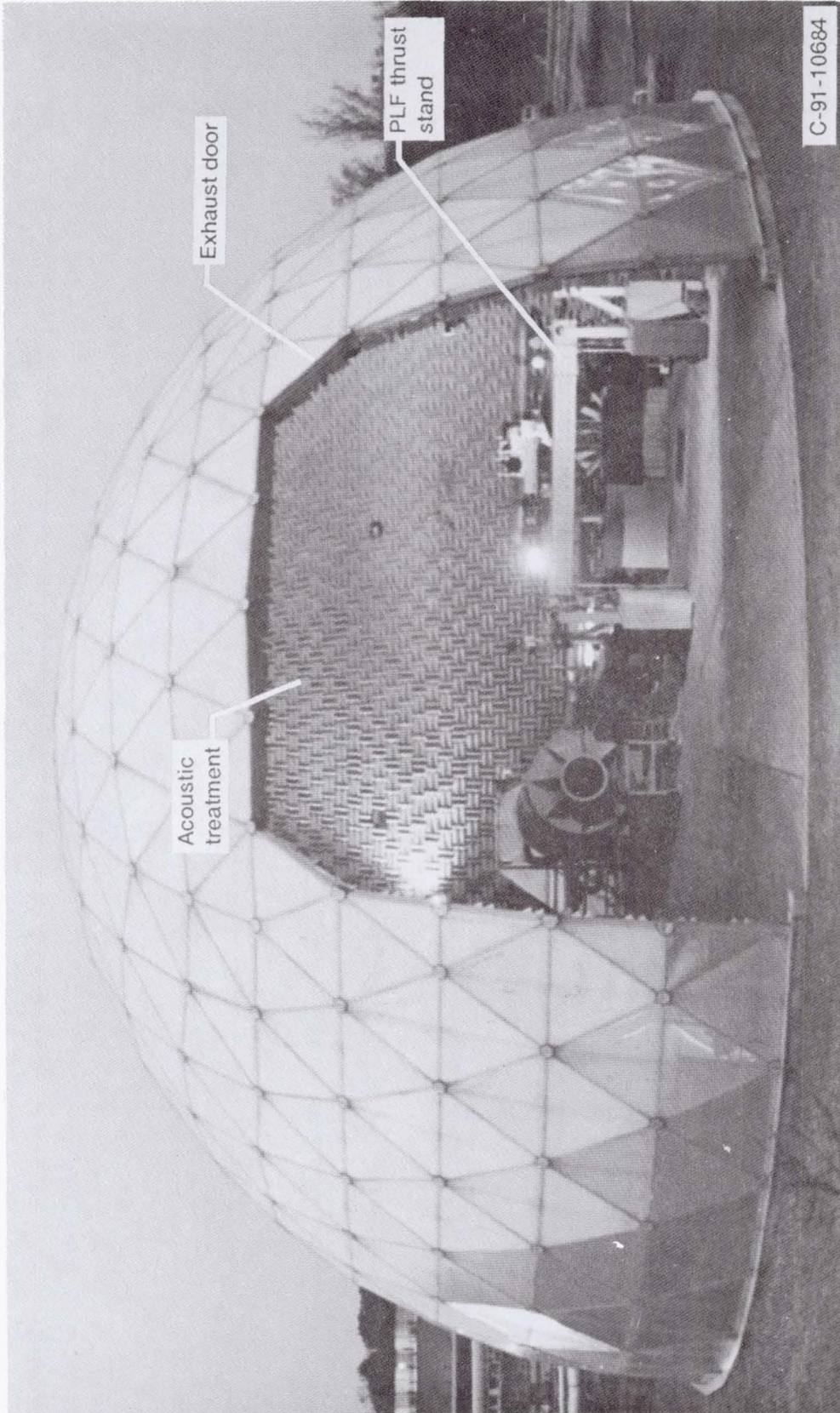


Figure B.1.—Acoustic geodesic dome.

Appendix C

Calibration and Thrust Calculation Procedures

Pressure Tare

(a) Flow momentum in the horizontally opposed ducts, MV

$$\frac{P_T}{P} = \left(\frac{1 + \sqrt{1 + \frac{2R}{g^2} \left(\frac{\gamma-1}{\gamma} \right) \left[\frac{W\sqrt{T_T}}{2(254.5)P} \right]^2}}{2} \right)^{\frac{\gamma}{\gamma-1}} \quad (C1)$$

$$MV = \left(\frac{2R\gamma}{\gamma-1} \left[1 - \left(\frac{P_T}{P} \right)^{\left(1 - \frac{1}{\gamma} \right)} \right] \right)^{\frac{1}{2}} \frac{W\sqrt{T_T}}{g} \quad (C2)$$

(b) Hydrostatic forces in the horizontally opposed ducts, $DEL R_n$ $n=1$ to 6

$$DEL R_n = CR_n [A_{duct} (P - P_a) + MV] \quad (C3)$$

CR_n are from an input dataset and are calculated from the slopes of P vs. load cell force (R_n)

Forces and Moments at the centroid of the thrust frame, [F]

The principle equation relating the output of the six system load cells to the six components of force/moments acting at the thrust-frame centroid is the following matrix equation:

$$[RC] = [S][F] \quad (C4)$$

where:

$$[RC] = \begin{bmatrix} R_1 - DELR_1 \\ R_2 - DELR_2 \\ R_3 - DELR_3 \\ R_4 - DELR_4 \\ R_5 - DELR_5 \\ R_6 - DELR_6 \end{bmatrix} \quad (C5)$$

= system load cell outputs corrected for pressure tare

$$[S] = \begin{bmatrix} S_{11} & S_{12} & S_{13} & S_{14} & S_{15} & S_{16} \\ S_{21} & S_{22} & S_{23} & S_{24} & S_{25} & S_{26} \\ S_{31} & S_{32} & S_{33} & S_{34} & S_{35} & S_{36} \\ S_{41} & S_{42} & S_{43} & S_{44} & S_{45} & S_{46} \\ S_{51} & S_{52} & S_{53} & S_{54} & S_{55} & S_{56} \\ S_{61} & S_{62} & S_{63} & S_{64} & S_{65} & S_{66} \end{bmatrix} \quad (C6)$$

= are the coefficients of the static hydraulic calibration

$$[F] = \begin{bmatrix} FX \\ FY \\ FZ \\ MX \\ MY \\ MZ \end{bmatrix} \quad (C7)$$

The force matrix [F] may then be solved by:

$$[F] = [SI][RC] \quad (C8)$$

where [SI] is the inverse of [S].

$$[SI] = [S]^{-1} \quad (C9)$$

Appendix D**Sample PLF Hydraulic Calibration Plots**

The following pages contain the hydraulic calibration plots for one input (calibration) load cell.

input: x-axis, calibration load cell, BX (Figure 2.4)

output: y-axis, each of the reaction load cells, R1-R6

Collectively, the 42 interactions (6 reaction load cells x 7 calibration load cells) result in the 6 x 6 sensitivity matrix.

Note:

Reaction cells R4-R6 show the most scatter. These measurements are in the *vertical* direction, and have a history of calibration shift. The ejector however, mainly depends on R1, which has stayed fairly constant.

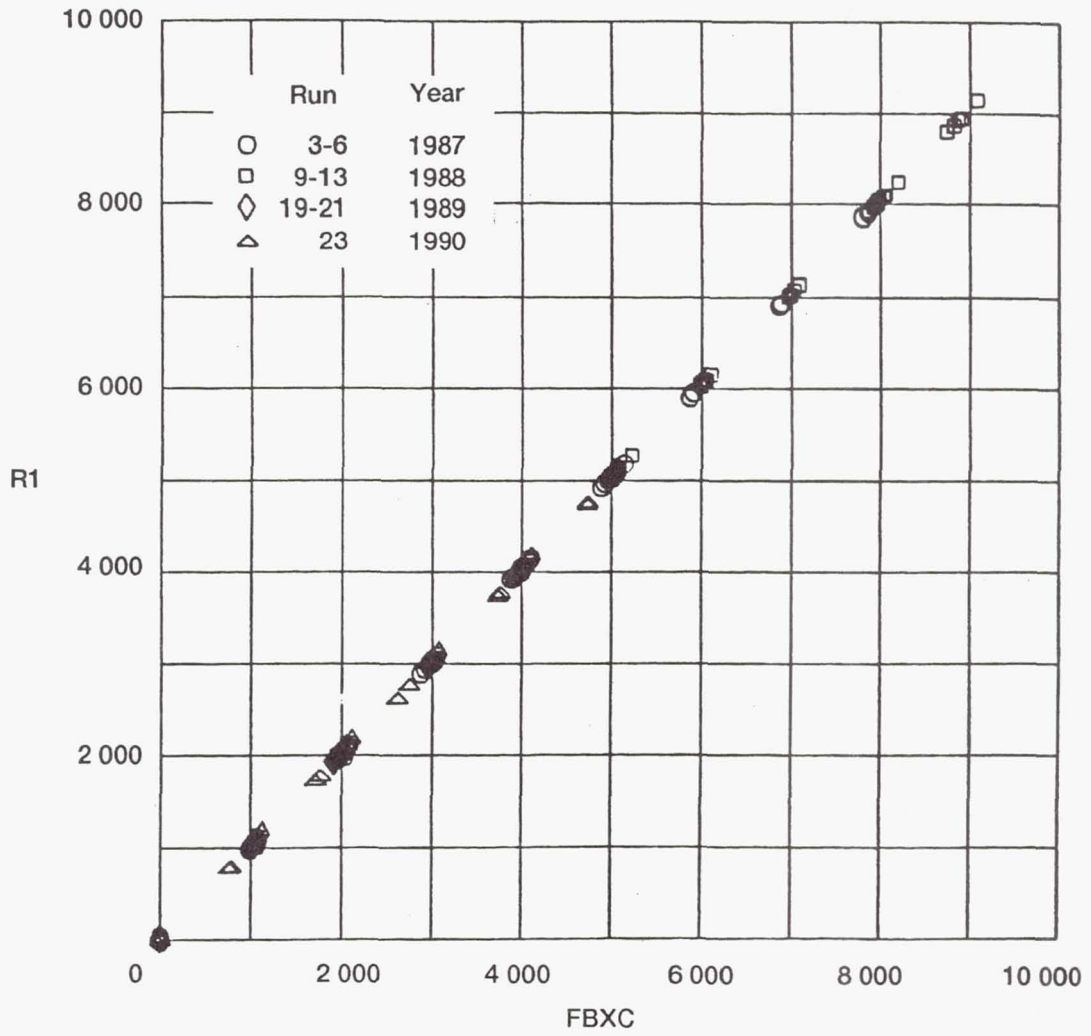


Figure D.1.—PLF hydraulic calibrations runs: R1.

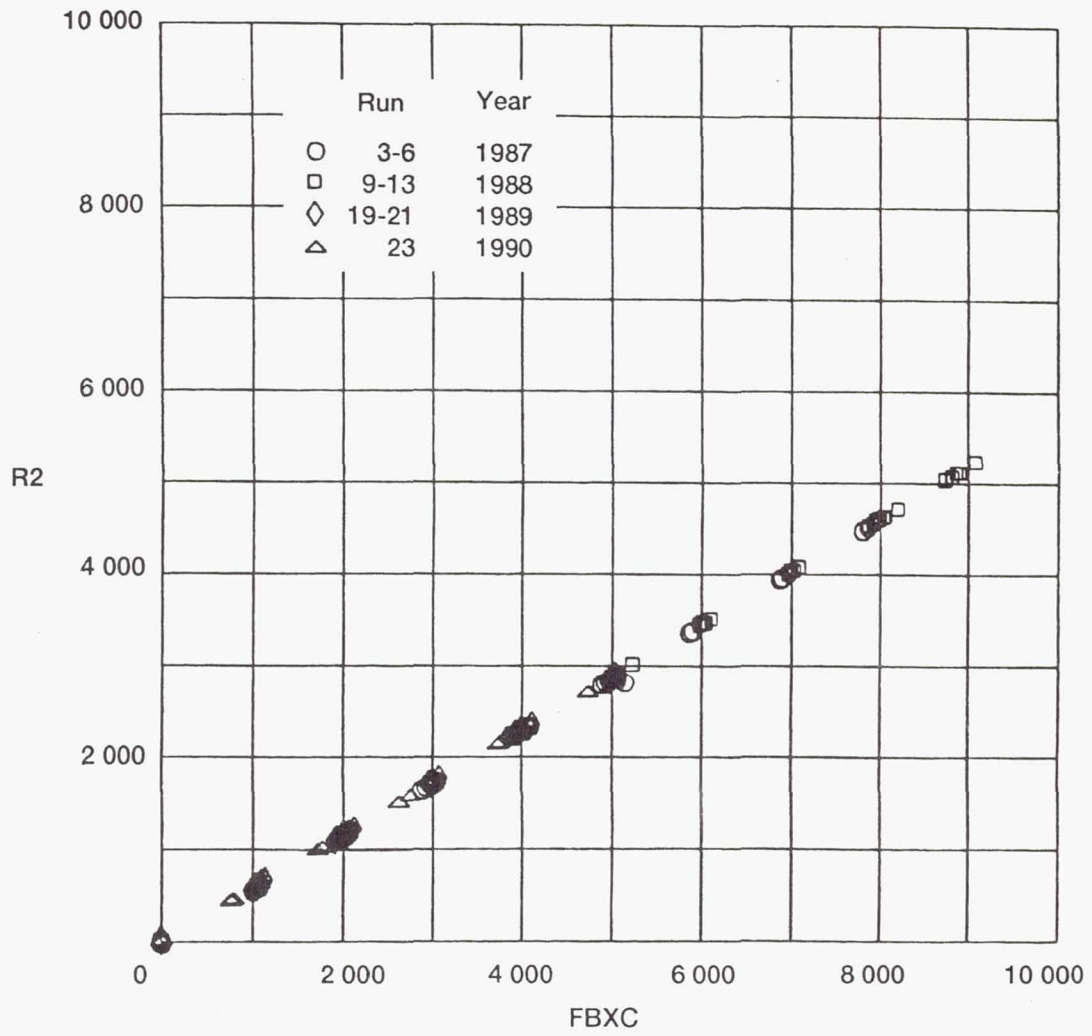


Figure D.2.—PLF hydraulic calibrations runs: R2.

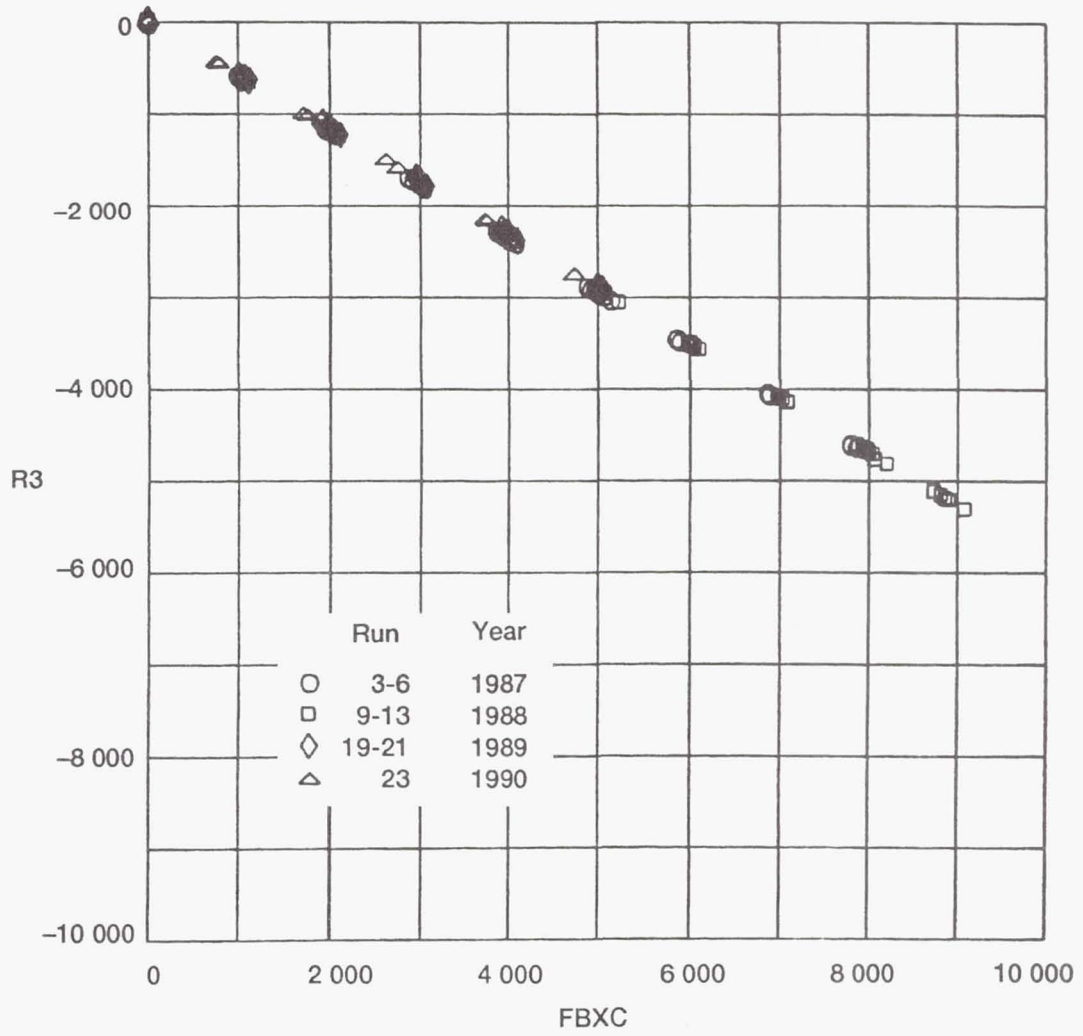


Figure D.3.—PLF hydraulic calibrations runs: R3.

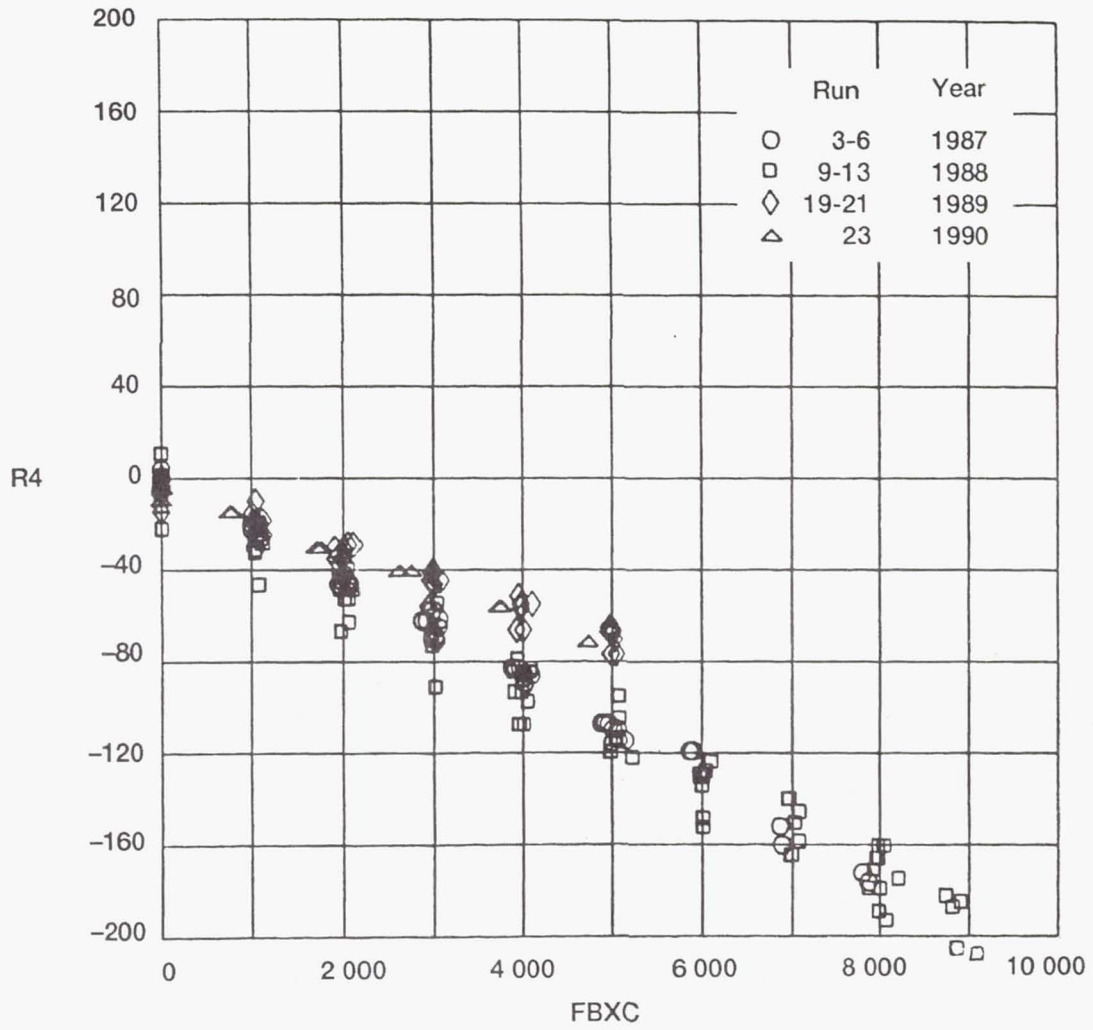


Figure D.4.—PLF hydraulic calibrations runs: R4.

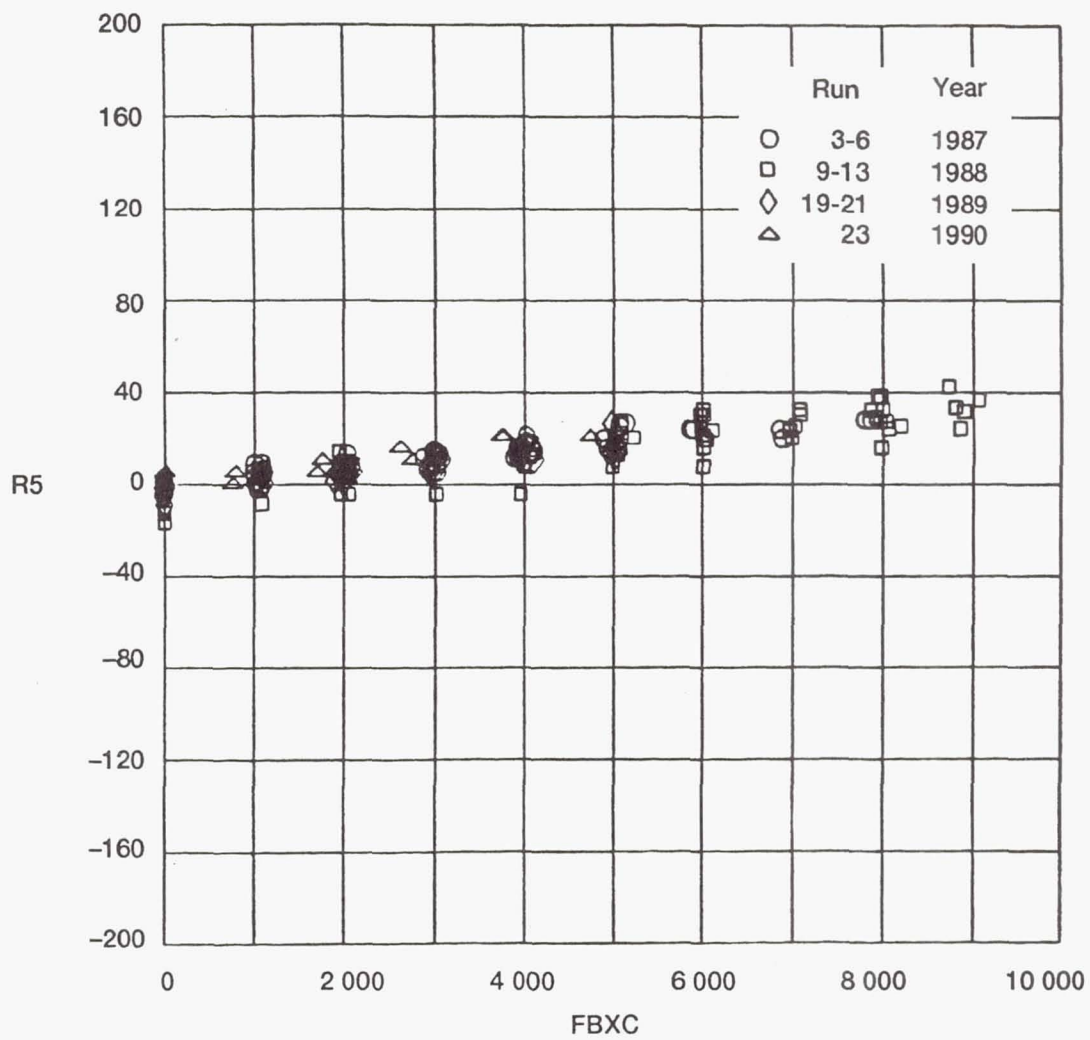


Figure D.5.—PLF hydraulic calibrations runs: R5.

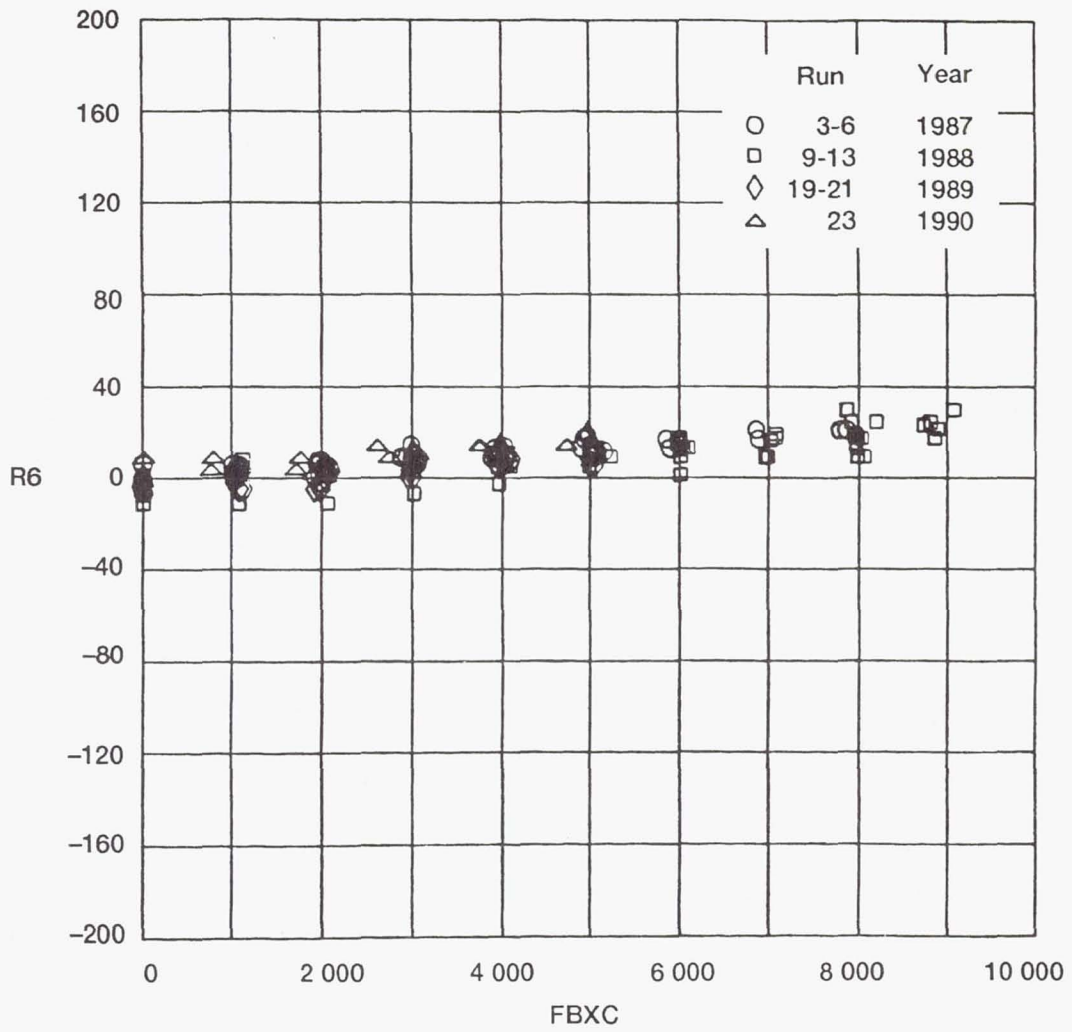


Figure D.6.—PLF hydraulic calibrations runs: R6.

Appendix E

Development of the Governing Equations for the Munk and Prim Principle

Continuity

The general differential equation of continuity is:

$$\frac{\partial \rho}{\partial t} + \nabla \cdot (\rho \vec{V}) = 0 \quad (\text{E1})$$

for steady flow:

$$\frac{\partial}{\partial t} = 0 \quad (\text{E2})$$

then:

$$\nabla \cdot (\rho \vec{V}) = 0 \quad (\text{E3})$$

for a perfect gas:

$$\rho = \frac{P}{RT} \quad (\text{E4})$$

then:

$$\begin{aligned} \rho \vec{V} &= \frac{P}{\sqrt{RT}} \frac{\vec{V}}{\sqrt{RT}} \frac{\sqrt{\gamma}}{\sqrt{\gamma}} \\ &= P \sqrt{\frac{\gamma}{RT}} \vec{M} \end{aligned} \quad (\text{E5})$$

for isentropic flow:

$$\frac{T_T}{T} = 1 + \frac{\gamma-1}{2} M^2 \quad (\text{E6})$$

$$\frac{P_T}{P} = \left(1 + \frac{\gamma-1}{2} M^2\right)^{\frac{\gamma}{\gamma-1}} \quad (\text{E7})$$

substituting into E5:

$$\rho \vec{V} = \frac{P_T}{\sqrt{T_T}} \sqrt{\frac{\gamma}{R}} \vec{M} \left(1 + \frac{\gamma-1}{2} M^2\right)^{\frac{-(\gamma+1)}{2(\gamma-1)}} \quad (\text{E8})$$

then:

$$\nabla \cdot \left[\frac{P_T}{\sqrt{T_T}} \sqrt{\frac{\gamma}{R}} \vec{M} \left(1 + \frac{\gamma-1}{2} M^2\right)^{\frac{-(\gamma+1)}{2(\gamma-1)}} \right] = 0 \quad (\text{E9})$$

but for isentropic flow:

P_T , T_T , γ , and R are all constant

therefore:

$$\nabla \cdot \left[\vec{M} \left(1 + \frac{\gamma-1}{2} M^2\right)^{\frac{-(\gamma+1)}{2(\gamma-1)}} \right] = 0 \quad (\text{E10})$$

Momentum

The differential equation of momentum for an inviscid, perfect gas is:

$$\rho \frac{D\vec{V}}{Dt} = -\nabla P \quad (\text{E11})$$

for steady flow this becomes:

$$(\vec{V} \cdot \nabla)\vec{V} = -\left(\frac{1}{\rho}\right)\nabla P \quad (\text{E12})$$

rearranging the Mach number definition:

$$\vec{V} = \sqrt{\gamma RT} \vec{M} \quad (\text{E13})$$

and noting the vector operation:

$$\nabla \cdot s \vec{v} = (\nabla s \cdot \vec{v}) + s(\nabla \cdot \vec{v}) \quad (\text{E14})$$

then E12 becomes:

$$\sqrt{\gamma RT} \vec{M} \cdot \nabla (\sqrt{\gamma RT} \vec{M}) = -\left(\frac{1}{\rho}\right)\nabla P \quad (\text{E15})$$

Expanding:

$$\sqrt{\gamma RT} \vec{M} \cdot [\sqrt{\gamma RT} \nabla \vec{M} + \vec{M} \nabla (\sqrt{\gamma RT})] = -\left(\frac{1}{\rho}\right)\nabla P$$

$$(\sqrt{\gamma RT} \vec{M}) \cdot (\sqrt{\gamma RT} \nabla \vec{M}) + \sqrt{\gamma RT} \vec{M} \cdot [\vec{M} \nabla (\sqrt{\gamma RT})] = -\left(\frac{1}{\rho}\right)\nabla P$$

$$\gamma RT \vec{M} \cdot \nabla \vec{M} + \sqrt{\gamma RT} \vec{M} \cdot \vec{M} \nabla(\sqrt{\gamma RT}) = -\left(\frac{1}{\rho}\right) \nabla P$$

divide by γRT :

$$(\vec{M} \cdot \nabla) \vec{M} + \frac{\sqrt{\gamma RT}}{\gamma RT} \vec{M} \cdot \vec{M} \nabla(\sqrt{\gamma RT}) = -\left(\frac{1}{\rho \gamma RT}\right) \nabla P \quad (\text{E16})$$

remember the ideal gas law:

$$P = \rho RT \quad (\text{E17})$$

therefore:

$$P \gamma = \rho \gamma RT \quad (\text{E18})$$

The right hand side of E16 then becomes:

$$-\frac{\nabla P}{\gamma P} = -\frac{1}{\gamma} \ln P \quad (\text{E19})$$

and E16 becomes:

$$(\vec{M} \cdot \nabla) \vec{M} + \frac{1}{\sqrt{\gamma RT}} \vec{M} \cdot \vec{M} \nabla(\sqrt{\gamma RT}) + \frac{1}{\gamma} \ln P = 0 \quad (\text{E20})$$

a bit more algebra applied to the second term of E20 and you get the Munk and

Prim form of the momentum equation:

$$(\vec{M} \cdot \nabla) \vec{M} - \frac{\gamma-1}{\gamma+1} \vec{M} (\nabla \cdot \vec{M}) + \frac{1}{\gamma} \nabla \ln(P) = 0 \quad (\text{E21})$$

To convert to total pressure, use the isentropic relation:

$$\frac{P}{P_T} = \left(1 + \frac{\gamma-1}{2} M^2\right)^{-\frac{\gamma}{\gamma-1}} \quad (\text{E22})$$

Then E21 becomes:

$$\begin{aligned} (\vec{M} \cdot \nabla) \vec{M} - \left(\frac{\gamma-1}{\gamma+1}\right) \vec{M} (\nabla \cdot \vec{M}) + \frac{1}{\gamma} \nabla \ln \left[P_T \left(1 + \frac{\gamma-1}{2} M^2\right)^{-\frac{\gamma}{\gamma-1}} \right] &= 0 \\ (\vec{M} \cdot \nabla) \vec{M} - \left(\frac{\gamma-1}{\gamma+1}\right) \vec{M} (\nabla \cdot \vec{M}) + \frac{1}{\gamma} \nabla \left[\ln \left(1 + \frac{\gamma-1}{2} M^2\right)^{-\frac{\gamma}{\gamma-1}} + \ln(P_T) \right] &= 0 \\ (\vec{M} \cdot \nabla) \vec{M} - \left(\frac{\gamma-1}{\gamma+1}\right) \vec{M} (\nabla \cdot \vec{M}) + \frac{1}{\gamma} \nabla \left[\ln \left(1 + \frac{\gamma-1}{2} M^2\right)^{-\frac{\gamma}{\gamma-1}} \right] + \frac{1}{\gamma} \nabla \ln(P_T) &= 0 \end{aligned}$$

And finally you have the Munk and Prim momentum equation expressed in terms of total pressure:

$$\begin{aligned} (\vec{M} \cdot \nabla) \vec{M} - \left(\frac{\gamma-1}{\gamma+1}\right) \vec{M} (\nabla \cdot \vec{M}) + \\ - \left(\frac{1}{\gamma-1}\right) \nabla \left[\ln \left(1 + \frac{\gamma-1}{2} M^2\right) \right] + \frac{1}{\gamma} \nabla \ln(P_T) = 0 \end{aligned} \quad (\text{E23})$$

REPORT DOCUMENTATION PAGE

Form Approved
OMB No. 0704-0188

Public reporting burden for this collection of information is estimated to average 1 hour per response, including the time for reviewing instructions, searching existing data sources, gathering and maintaining the data needed, and completing and reviewing the collection of information. Send comments regarding this burden estimate or any other aspect of this collection of information, including suggestions for reducing this burden, to Washington Headquarters Services, Directorate for Information Operations and Reports, 1215 Jefferson Davis Highway, Suite 1204, Arlington, VA 22202-4302, and to the Office of Management and Budget, Paperwork Reduction Project (0704-0188), Washington, DC 20503.

1. AGENCY USE ONLY (Leave blank)	2. REPORT DATE February 1993	3. REPORT TYPE AND DATES COVERED Technical Memorandum	
4. TITLE AND SUBTITLE Full-Scale STOVL Ejector Experiment		5. FUNDING NUMBERS WU-505-68-32	
6. AUTHOR(S) Wendy S. Barankiewicz			
7. PERFORMING ORGANIZATION NAME(S) AND ADDRESS(ES) National Aeronautics and Space Administration Lewis Research Center Cleveland, Ohio 44135-3191		8. PERFORMING ORGANIZATION REPORT NUMBER E-7433-1	
9. SPONSORING/MONITORING AGENCY NAMES(S) AND ADDRESS(ES) National Aeronautics and Space Administration Washington, D.C. 20546-0001		10. SPONSORING/MONITORING AGENCY REPORT NUMBER NASA TM-106019	
11. SUPPLEMENTARY NOTES Responsible person, Wendy S. Barankiewicz, (216) 433-8706.			
12a. DISTRIBUTION/AVAILABILITY STATEMENT Unclassified - Unlimited Subject Category		12b. DISTRIBUTION CODE	
13. ABSTRACT (Maximum 200 words) The design and development of thrust augmenting short take-off and vertical landing (STOVL) ejectors has typically been an iterative process. In this investigation, static performance tests of a full-scale vertical lift ejector were performed at primary flow temperatures up to 1560 R (1100 °F). Flow visualization (smoke generators, yarn tufts and paint dots) was used to assess inlet flowfield characteristics, especially around the primary nozzle and end plates. Performance calculations are presented for ambient temperatures close to 480 R (20 °F) and 535 R (75 °F) which simulate "seasonal" aircraft operating conditions. Resulting thrust augmentation ratios are presented as functions of nozzle pressure ratio and temperature. Full-scale experimental tests such as this are expensive, and difficult to implement at engine exhaust temperatures. For this reason the utility of using similarity principles – in particular, the Munk and Prim similarity principle for isentropic flow – was explored. At different primary temperatures, exit pressure contours are compared for similarity. A nondimensional flow parameter is then shown to eliminate primary nozzle temperature dependence and verify similarity between the hot and cold flow experiments. Under the assumption that an appropriate similarity principle can be established, then properly chosen performance parameters should be similar for both hot flow and cold flow model tests.			
14. SUBJECT TERMS Ejectors; Powered Lift Aircraft; STOVL		15. NUMBER OF PAGES 120	
		16. PRICE CODE A06	
17. SECURITY CLASSIFICATION OF REPORT Unclassified	18. SECURITY CLASSIFICATION OF THIS PAGE Unclassified	19. SECURITY CLASSIFICATION OF ABSTRACT Unclassified	20. LIMITATION OF ABSTRACT

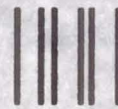
National Aeronautics and
Space Administration

Lewis Research Center
Cleveland, Ohio 44135

Official Business
Penalty for Private Use \$300

FOURTH CLASS MAIL

ADDRESS CORRECTION REQUESTED



Postage and Fees Paid
National Aeronautics and
Space Administration
NASA 451

NASA
